INVESTIGATING THE STABILITY AND MODES OF DEACTIVATION OF METAL-EXCHANGED ZEOLITES VIA COMPUTATIONAL MODELING

A Dissertation submitted to the Graduate Faculty

of the University of Virginia in Candidacy for the Degree of

Doctor of Philosophy

---

by

Keka Mandal

Department of Chemical Engineering

University of Virginia

May 2023

Christopher Paolucci, Advisor

Robert J. Davis, Chair

William S. Epling

Prasanna V. Balachandran

Rajamani Gounder

APPROVAL SHEET

This

Dissertation

is submitted in partial fulfillment of the requirements
for the degree of

Doctor of Philosophy

Author: Keka Mandal

This Dissertation has been read and approved by the examing committee:

Advisor: Christopher Paolucci

Advisor:

Committee Member: Robert J. Davis

Committee Member: William S. Epling

Committee Member: Prasanna V. Balachandran

Committee Member: Rajamani Gounder

Committee Member:

Committee Member:

Accepted for the School of Engineering and Applied Science:

Jennifer L. West, School of Engineering and Applied Science

May 2023

Investigating the Stability and Modes of Deactivation of Metal-exchanged Zeolites via Computational Modeling

Keka Mandal

(ABSTRACT)

Zeolite-supported metal catalysts are an integral part of heterogeneous catalysis, with applications in petrochemical processing, biomass conversion, conversion of aromatics, and automobile exhaust aftertreatment. In addition to displaying excellent catalytic activity, selectivity, and hydrothermal stability, zeolites enable tuning of the metal distribution and speciation, ranging from isolated cations to nanoparticles, by means of variation in synthesis, compositional parameters such as Si/Al ratio, metal loading, and gas treatments. Metals in zeolites can exist as (a) cations exchanged in the zeolitic framework, (b) clusters ($<$ 2 nm) encapsulated in the zeolite cages, and (c) extracrystalline nanoparticles located on the outer surface of zeolite crystallites. The dynamic chemical nature of the metal active sites in ion-exchanged zeolites warrants a molecular level investigation of their speciation and interaction with gas molecules under reaction conditions of interest, to understand the deactivation and regeneration mechanisms of zeolite-supported metal catalysts. Here, we studied zeolites ion-exchanged with Pd and Cu by employing computational modeling and tools such as density functional theory (DFT), wave function theory (WFT), ab initio molecular dynamics (AIMD) simulations, first principles based thermodynamic calculations, and kinetic Monte Carlo (kMC) simulations. We first investigated hydrothermal deactivation and regeneration thermodynamics and mechanisms for Pd-zeolites. We determined Pd cation speciation under different conditions and used this information

to study the redispersion of extra-crystalline Pd nanoparticles to ion-exchanged Pd^{2+} cations in zeolites. We found that H_2O pressure plays a critical role in determining the phase boundary between Pd cations and Pd-oxide, and redispersion from Pd-oxide to Pd cations follows an Ostwald ripening-like mechanism. Next, we studied chemical deactivation via sulfur for commercial Cu-zeolites to determine Cu species that are particularly susceptible to irreversible poisoning. Ab initio thermodynamic models for sulfur poisoning of Cu-CHA zeolites showed that Cu dimers that form at high temperatures strongly bind SO_2 and SO_3, forming (bi)sulfated Cu dimers with remarkable thermodynamic stabilities, that require high temperature (> 870 K) desulfation treatments for catalyst regeneration. Taken together, these studies point towards molecularly detailed design rules for improving the thermal and chemical stability of metal-containing zeolite catalysts.

Acknowledgments

I would like to thank my advisor, Christopher Paolucci, for his continued support and guidance throughout my PhD journey. His feedback and encouragement have helped me become not only a better researcher, but improve my technical writing and presentation skills as well. His passion for science, teaching and mentorship is inspiring, and I aspire to emulate that in my research career. I feel proud to have been one of his graduate students (in fact, the very first one!), and privileged to have had the opportunity to learn a lot from him.

I'm also grateful to Prof. Robert J. Davis, and Prof. Wiliam S. Epling, for their technical insights, guidance, and feedback throughout the years.

I would also like to acknowledge my experimental collaborators, past and present, Dr. Yuntao (Kevin) Gu (UVA), Dr. Trevor Lardinois (Purdue University), Dr. Yu-ren Chen (UVA), Dr. Lai Wei (UVA), and Prof. Rajamani Gounder (Purdue University) for their guidance and patience. The experience of being able to work and learn about experiments and spectroscopic methods from them has been especially enriching and rewarding. I would like to thank our collaborators at Cummins Inc., Dr. Rohil Daya and Dr. Daniyal Kiani for their questions, suggestions and advice that has continued to make our research work better.

I would like to also acknowledge the past and present group members from the Epling and Davis Lab whose work has been a source of constant learning for me, and the amazing undergraduate researchers I have worked with over the years, Karl Westendorff, Anupama Jayaraman, and Kijeong Nam.

I would like to acknowledge our funding sources, UVA Engineering Research and In-

novation Award, Double Hoo Research Grant, and Cummins Inc., and UVA Research Computing for the computational resources and support. I'm thankful to Cummins Inc. for giving me the opportunity to do a summer internship, and my supervisor, Matt Anderson, Dr. Krishna Kamasamudram, and the entire Advanced Chemical Systems and Integration team for their support.

None of the amazing things that have happened to me in the last five years would have been possible without the support of my wonderful research group and friends. Thank you to my group members Asanka Wijerathne, Anna Sviripa, Anukriti Shreshtha, Sugandha Verma, Gabriel Dickey, Ching-Heng Tai, and past group members, Changming Liu and Xutao Gao, my peers Colby Whitcomb, Silvia Marino, Natalia Diaz Montenegro, and Tracy Kuper, for making the fun moments even more joyous, and the challenging ones seem easier. I'm fortunate to have made such amazing friends for life, who have always been a pillar of support, and my family here at UVA.

Finally, I want to express my heartfelt gratitude to the people behind the scenes, my family back in India, my parents Kajal Mandal, Karnadev Mandal, and my brother Kaushik Mandal, and my wonderful life partner Akshay Agrawal, for their unwavering and unconditional encouragement, patience, and belief in me. I dedicate my PhD to them, which wouldn't have been possible without their sacrifices, love, and support.

Contents

List of Figures

List of Tables

Chapter 1

Introduction

1.1 Significance of Supported Metal Catalysts in Heterogeneous Catalysis

Transition metals on metal oxide supports such as silica, alumina, ceria, etc. are widely used heterogeneous catalysts for several industrial applications, chemical manufacturing, and environmental catalysis, to name a few. The performance of these metal supported catalysts is closed linked to the metal particle size, with metal active sites ranging from single metal atoms, sub-nanometric clusters (<1 nm) to large metal nanoparticles (1–100 nm). Reduction in particle size increases its unsaturated coordination and surface free energy, rendering the metal sites more reactive towards the support and adsorbates. This correlation between particle size and activity and selectivity often forms the basis for rational catalyst design and synthesis.[1,2] However, the optimal catalyst design and operation also needs to take into account the effect of structural changes of metal active sites on the catalyst stability and deactivation.

Catalyst deactivation, i.e. the loss of catalytic activity and (or) selectivity over a period of time (ranging from seconds to years), and catalyst instability under condition of operation and (or) storage, pose serious economic and environmental challenges to industrial processes. A rapidly deactivating or unstable catalyst, can raise replenish-

ment costs, making the process operation cost-inefficient, or deter the commercialization of new technologies which might otherwise have a high performance. Thus, understanding the dynamic interplay between structure-performance relationships in the context of catalyst stability and deactivation, under different reaction conditions is crucial.

1.2 Modes of Catalyst Deactivation

The modes of catalyst deactivation can be broadly categorized as thermal, chemical, and mechanical in nature.[3,4] For the scope of this dissertation, we are going to focus on thermal and chemical deactivation of catalysts.

1.2.1 Chemical Deactivation

Chemical deactivation occurs via strong chemisorption or reaction of the active sites with reactants, products, and (or) impurities, which can either physically block the active sites and (or) induce structural changes in the metal sites, transforming them to an inactive phase.[3–5] In particular, structure-sensitive reactions are reported to be more susceptible to chemical poisoning compared to structure-insensitive reactions. Chemical deactivation can be either reversible or irreversible, and necessitates structural information of the poison covered metal surface, and how the poison coverage changes the surface structure and coordination chemistry.[4] For instance, sulfur poisoning of industrial catalysts used in processes like hydrogenation, steam reforming, ammonia synthesis, etc. is a long-standing challenge, whereby the sulfur can deactivate the metal sites via (1) physical blockage of the adsorption or reactive sites;

(2) restructuring of the catalytic surface; (3) electronic modification of the nearest neighbor metal atoms due to the strong sulfur-metal chemical bond; and (4) limiting or inhibiting surface diffusion and (re)combination of adsorbed reactants.[4,6] Regeneration of sulfur-poisoned catalysts often requires high temperatures which can in turn lead to sintering of the catalyst.[4,7]

1.2.2 Thermal Degradation via Particle Sintering and Redispersion

Thermal deactivation of supported metal catalyst results from exposure to high temperatures and reducing species, causing single atoms and clusters to aggregate into larger particles via (1) migration and coalescence of crystals on the support, and (or) (2) Ostwald ripening due to gas-phase or surface mediated atomic migration.[3,4,8] The aggregation of active single metal atoms or smaller clusters to form larger particles decreases the active surface of the catalyst, and is called as particle sintering. The reverse process is known as particle redispersion, and depending on the nature of active sites required for a reaction process, can cause catalyst deactivation (disintegration of metal particles to inactive isolated sites) or catalyst regeneration (recovery of active single atoms from particles). Critical reaction and catalyst parameters that can affect particle sintering and redispersion are (1) temperature (sintering increases exponentially with rise in temperature); (2) reaction environment (oxidizing conditions promote sintering, while metal redispersion can be induced by high temperature oxidation, followed by reduction. Water vapor has been shown to accelerate sintering in metal oxide supports); (3) metal-support interactions (also affects the thermal stability of metal particles in O_2); (4) presence of 'trapping sites' or defects on the support (hinder mobility and surface migration, decreasing rates of sintering); and

(5) porosity of catalyst supports (sintering is lower in porous supports such as zeolites compared to non-porous ones).[4]

1.3 Role of Zeolites in Heterogeneous Catalysis

Zeolites are crystalline aluminosilicates made up of interconnected SiO_4 and AlO_4 tetrahedra, and are ubiquitous in heterogeneous catalysis, with applications for chemical separations, petroleum refining, hydrogenation, oxidation, and carbon-carbon coupling reactions, and pollution abatement technologies. Synthesis protocols and gas treatments, along with compositional parameters such as Si/Al ratio, and metal loading, can be used to tune the speciation, location and spatial distribution of the metal species in the zeolites. Metal species in zeolites can be present as **(a)** single atom cations exchanged in the zeolitic framework (represented as metal/zeolites), **(b)** metal clusters ($<$ 2 nm) encapsulated in the zeolite cages, and **(c)** extra-crystalline metal nanoparticles located on the outer surfaces of zeolites. Unlike the case of traditional metal oxide supports where the metal-support interaction is not strong enough to deter sintering of single metal atoms, the well-defined, nanoporous cage-like structures of zeolites can confine and stabilize small nanoparticles ($<$ 2 nm), slowing down rates of sintering.[9,10]

1.4 Structural Interconversion between Metals Cations and Particles in Zeolites

Structural transformation between metal speciation in zeolites have been widely researched in industry and academia. The extent of atomic dispersion and formation of nanoparticles is also dictated by the synthesis techniques used for dispersion of Pd into zeolite supports, such as incipient wetness impregnation, wet impregnation, solution ion-exchange, and solid-state ion-exchange.[11,12] Solution ion-exchange has been reported to impart the highest initial atomic dispersion of Pd to single Pd cations exchanged in the zeolites.[13] Studies have shown that solid-state ion-exchange in zeolites with high Si/Al ratios (>10) induce PdO agglomeration, with HAADF-STEM images showing PdO nanoparticles > 10 nm for Si/Al $\sim$ 30, and 1 wt% Pd loading. Small PdO clusters (< 2 nm), seen at Si/Al = 12 and 1 wt% Pd loading, can exist both as encapsulated particles in the zeolite cages, and on the exterior surface of the zeolite. However, for an identical Pd loading, Si/Al = 6 showed complete atomic dispersion to single Pd cations.

While reducing environments can lead to the agglomeration of single metal cations ion-exchanged in the zeolite framework to encapsulated metal clusters and extra-crystalline metal particles, the reverse, i.e. atomic redispersion of agglomerated metal particles to single atom cations can also occur.[10] Reversible interconversion between Pt single atoms and nanoparticles in high-silica CHA zeolite was reported by Moliner et al.[14] via cyclical reduction-oxidation treatments. Sustained regeneration of Pd active sites by reduction-oxidation cycles in Pd/MOR allowed Petrov et al.[15] to maintain high conversion (90%) of methane oxidation and stability even after more than 90 h in hydrothermal aging (HTA) conditions. High temperature and presence of reductants

have a detrimental impact on the longevity of Pd/zeolites by inducing sintering of Pd cations forming agglomerated metallic Pd, and PdOx domains, causing a loss in their NOx storage capacity at low temperatures ($<$ 473 K).[13] Studies have reported different zeolite topologies to have different outcomes when subjected to HTA. CO-aged Pd/ZSM5 and Pd/MCM22 exhibited regeneration following HTA at 1023 K in a recent study by Bello et al.,[16] who found that while Pd/ZSM5 completely recovered its NOx storage capacity, Pd/MCM22 regained only ∼50% of its previous capacity. This was attributed to the formation of a higher fraction of larger metal agglomerates (∼15-20 nm) in Pd/MCM22 during aging as compared to Pd/ZSM5, where majority of agglomerates had average sizes $<$ 4 nm.[16] High temperature air treatments (723–1023 K) have also been shown to impact the synthesis methods, resulting in a more uniform spatial distribution of Pd.[17] An increased amount of ion-exchanged Pd^{2+} cations were formed due to the redistribution of Pd species further into the interior sites of the zeolites with greater number of Brønsted acid sites as a consequence of the increased treatment temperatures.[17] Together, these studies evince the critical influence of the reaction conditions, and particle size on catalyst deactivation and the potential for regeneration, via structural transformation between metal particles and ion-exchanged cations.

Single metal cations in metal/zeolites, and their interaction with other compounds, exhibit similarities to their well-documented counterparts in the organometallic and homogeneous catalysis literature. Solvation and mobilization of metal ions by H_2O or other adsorbates such as NH_3 appear to be a general phenomenon of metal-exchanged zeolite systems under certain conditions, and has important consequences on catalytic function and adsorption of other gases such as CO, hydrocarbons, and sulfur for automobile emissions control. Reaction condition-dependent metal speciation and adsorp-

tion chemistry have important mechanistic implications on the catalytic performance of Cu/zeolites for selective catalytic reduction(SCR) of NOx in diesel engines,[18–21] the chemical deactivation induced by sulfur exposure,[22–31] and feasibility of regeneration methods.[23,28]

Thus, given the widespread practical implications of zeolite supported metal catalysts, and the dynamic nature of their physicochemical properties and catalytic activity, they represent an ideal model system for the study of the thermodynamic and kinetics of catalyst stability and deactivation.

1.5 Scope of This Dissertation

The aim of this dissertation is to develop a molecular level understanding of the thermodynamics and kinetics associated with thermal and chemical deactivation of metal-exchanged zeolites, using computational modeling and tools such as density functional theory (DFT), wave function theory (WFT), *ab initio* molecular dynamics (AIMD) simulations, first principles based thermodynamic calculations, and kinetic Monte Carlo (kMC) simulations, that can complement as well as supplement the insights gained from experiments and spectroscopic characterizations.

Chapter 2 presents a detailed examination of the speciation of Pd cations and their complexing with H_2O and NO, which are a critical parameters in the optimal design and synthesis in their implementation as passive NOx adsorbers (PNAs) in diesel engines. We report the formation of mobile and H_2O-solvated Pd^{2+} complexes under conditions of practical interest for PNAs, which upon exposure to NO evolve to H_2O-solvated Pd^{II}-NO^{-} complexes, a behavior that transcends across different zeolite

topologies.

Chapter 3 focuses on extracrystalline Pd nanoparticles and their conversion to ion-exchanged cations in the zeolites via redispersion of agglomerates of metal and metal-oxide domains. We found that nanoparticle size, and particle size distribution, gas conditions such as O_2 and H_2O pressures, and zeolite composition, dictate the thermodynamic extent and rates of conversion, and conditions under which the particle sintering (or redispersion) can occur.

Chapter 4 follows the distribution and coordination chemistry of monatomic and dimeric Cu species in SSZ-13 zeolites as a function of treatment conditions and the local Al distribution, and their interaction with SO_2/SO_3 at high temperatures (at low coverages of NH_3), and the implications of sulfur poisoning of dimeric Cu species on the catalytic SCR performance.

Chapter 2

Condition-Dependent Pd Speciation and NO Adsorption in Pd/Zeolites

This chapter has been reproduced in its entirety with permission from Mandal, K.; Gu, Y.; Westendorff, K. S.; Li, S.; Pihl, J. A.; Grabow, L. C.; Epling, W. S.; Paolucci, C. Condition-Dependent Pd Speciation and NO Adsorption in Pd/Zeolites. *ACS Catal.* **2020**, 10, 12801−12818. Copyright 2020 American Chemical Society. The supplementary materials for this paper/ chapter can be found at https://doi.org/10.1021/acscatal.0c03585. This chapter highlights the importance of a molecular level understanding of the Pd cation speciation in zeolites, and its reaction chemistry under a variety of reaction environments, which are especially relevant to the low temperature NO trapping in diesel engines for emissions control. Here, we present experimental evidence from kinetic measurements and spectroscopy data, along with DFT calculations and thermodynamic modeling to address some of the ambiguities in the field of passive NOx adsorbers (PNAs) literature, and set the stage for the subsequent chapter on the redispersion of Pd nanoparticles to cations in zeolites. My contributions to this study included performing DFT calculations and AIMD simulations for arriving at the optimized geometries of all the Pd/SSZ-13 struc-

tures considered in this work, functional sensitivity analysis, and development of the thermodynamic model for evaluating the thermodynamic stability of Pd-coordinated species under a variety of reaction conditions. As a co-first author of this paper, I was palyed a lead role in the drafting and editing of the manuscript, and writing the Introduction and computational results sections, addressing reviewer queries and implementing suggested modifications.

2.1 Introduction

Metal-exchanged zeolites are widely used in chemical separations, catalysis, and pollution remediation technologies.[32–35] In the limit of single metal cations, the active sites in these materials resemble their analogues in the organometallic and homogeneous catalysis literature.[36] Metal cations form bonds to the zeolite or acquire ligands via gas adsorption and can become solvated, interacting only electrostatically with the zeolite framework.[18] Solvation and mobilization of metal ions by H_2O or other adsorbates appear to be a general phenomenon of metal-exchanged zeolite systems under certain conditions, and has important consequences on catalytic function and adsorption of other gases.[37–41] However, this phenomenon has largely gone unrecognized in the Pd/zeolite literature. Here, we integrate computation at multiple levels of theory, and in-situ spectroscopic and kinetic experimental measurements, to determine the nature of Pd complexes exchanged in zeolites. We explore the molecular structure of Pd-zeolite motifs under a wide range of conditions of practical relevance for NO abatement technologies, and catalytic CO oxidation and methanol synthesis. We show that H_2O-solvation of Pd cations profoundly affects their chemical nature, catalytic performance, and complexing with NO.

Pd cations have been extensively explored in the inorganic chemistry and homogeneous catalysis literature. Similar to most group 8 and higher transition metals, Pd typically favors lower oxidation states of Pd^{0} and Pd^{II}.[42–44] While Pd^{I} and Pd^{III} have been observed, their presence has only been confirmed in a minute number of homogeneous compounds.[43–49] Infrared (IR) evidence of carbonyl anions of binuclear Pd^{I} were reported by Goggin and coworkers,[48] and binuclear Pd^{I} isocyanide complexes have been synthesized by Otsuka et al.[44] Similar binuclear Pd^{I} complexes with various ligands have also been observed using a variety of spectroscopic characterization techniques.[42–44] However, mononuclear homogeneous Pd^{I} complexes have not yet been identified.[44] Even though higher oxidation states like +4, +5 and +6 have been identified for Pd in homogeneous complexes,[47,50–57] structural characterization of mononuclear Pd speciation in zeolites is wanting.

Zeolites are crystalline aluminosilicates comprised of interconnected tetrahedra of SiO_4 and AlO_4 to form a nanoporous, three-dimensional cage-like structure. Replacement of Si^{IV} with Al^{III} at the corner-sharing aluminosilicate tetrahedra, called T-sites, induces a negative charge on the zeolitic framework that is compensated by cations. Synthetic protocols determine the frame-work distribution of Al and the Si/Al ratio, which influence the speciation and location of the exchanged cation.[58–62] Depending upon the Al distribution, various local Al configurations are possible, producing numerous possibilities for the charge-compensating cation, which has, hitherto not been systematically investigated for Pd ions. The commonly observed Pd^{II} oxidation state can charge-compensate one or two Al T-sites in the form of a single Pd cation or Pd with an oxidizing ligand. Despite the absence of evidence for mononuclear Pd^{I} in homogeneous complexes, some studies have assigned Pd^{I} at a 1Al T-site as a possible species.[63–68]

Pd/zeolites have been investigated for catalytic alkene hydrogenation, methane oxidation, Wacker oxidation, selective catalytic reduction of NOx with methane (CH_4-SCR) and other applications.[15,69–75] Recently, Pd/zeolites have been studied for low temperature NOx trapping from automotive engine exhaust.[11–13,76–81] Pd/zeolites, among all other candidates, meet the practical requirements for NO storage capacity and NO release temperature, although their resistance against different aging modes, such as CO and hydrocarbon-induced degradation, and sulfur poisoning, needs further investigation.[13,77,82] Khivantsev et al.[64] synthesized a series of atomically dispersed Pd/SSZ-13 catalysts (Pd/Al = 0.03, Si/Al = 6) and reported IR features at 1860 cm^{-1} and 1805 cm^{-1} during NO exposure in the absence of H_2O, similar to those reported by Chen et al.[77] They assigned the 1860 cm^{-1} feature to Pd^{II}-NO and the 1805 cm^{-1} feature to Pd^{I}-NO. The effect of multiple H_2O adsorption and H_2O-solvation of Pd-nitrosyl complexes is still not well-understood.

Though there are IR NO stretching assignments in the Pd/zeolite literature for Pd^{I} species,[63–66] odd oxidation states including Pd^{I} and Pd^{III} have only been directly characterized in Pd/Y and X zeolites using EPR under vacuum and following exposure to H_2 at 298 K.[83,84] Descorme et al. invoked Pd^{I} to explain NO_2 formation upon NO exposure on Pd/ZSM-5 in the absence of O_2 and assigned an IR feature at 1881 cm^{-1} to NO on Pd^{I}; however, no other characterization was provided to demonstrate the oxidation state of Pd^{I}.[63]

Literature results highlight a number of ambiguities in our understanding of Pd/zeolites. The initial Pd distribution, Pd speciation during ion-exchange, and dependency on zeolite composition are not clear. The precise nature of the effect of H_2O on Pd speciation is also unknown. The coordination environment of Pd-NO complexes in the presence and absence of H_2O, a ubiquitous and non-innocent spectator in emis-

sion technologies, requires investigation. Here, we present a combined computational and experimental study on Pd speciation under a variety of conditions, highlight the hydration effect on Pd cation structures and reveal the intrinsic difference in the sites formed in the presence and absence of H_2O. We report that Pd complexes in zeolites primarily manifest as mobile and H_2O-solvated Pd^{II} complexes under conditions of practical interest for PNA, and catalytic CO and Wacker oxidation. We show that upon exposure to either NO, or mixtures of NO and CO, mobile and H_2O-solvated Pd^{II}-NO^- complexes form, and these observations extend to multiple zeolite topologies and rationalize a large number of observations in the literature.

2.2 Results

2.2.1 Pd Cation Speciation in the Absence of H_2O, 1Al vs 2Al

Motivated by NO- and CO-probe molecule spectroscopy-based evidence (FTIR, EXAFS and XRD)[12,64,65,85,86] and DFT calculations[64,66,87] we constructed molecular models for Pd charge-compensated by one or two Al T-sites in SSZ-13 zeolites. SSZ-13, classified as a chabazite (CHA) framework type,[88] is made up of four-, six-, and eight-membered rings (MR) arranged into an ~8 Å diameter cage with 3.8 × 3.8 × 3.8 Å pore dimensions, illustrated in **Figure 2.1a**. We denote (**Figure 2.1b**) Pd^{I} cations exchanged at one Al T-site in SSZ-13 as $[ZPd^{I}]$, and Pd^{II} cations exchanged at one and two Al T-sites as $[ZPd^{II}OH]$ and $[Z_2Pd^{II}]$, respectively. 'Z' symbolizes the Si T-site substituted by Al, and when enclosed in square brackets, represents bonding of the Pd cation and its associated ligands with the zeolite framework. CHA has one

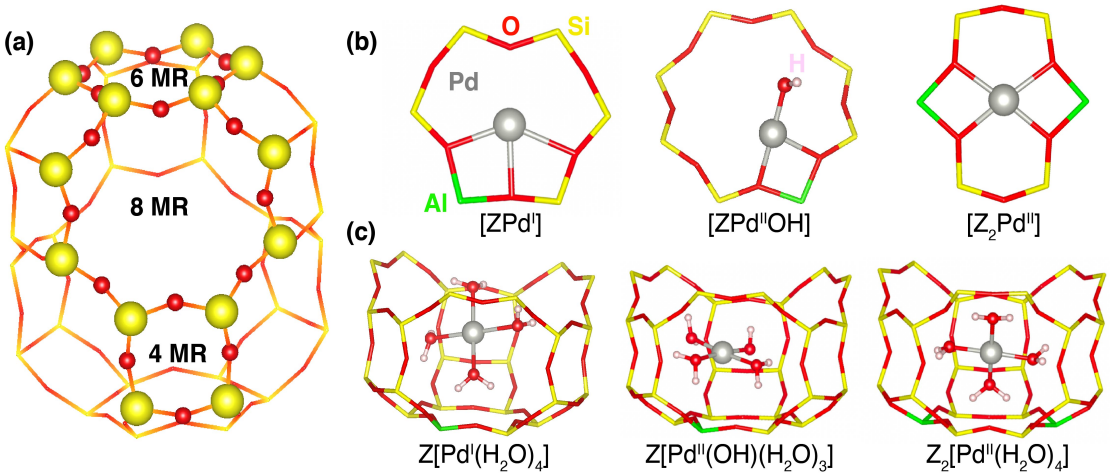

Figure 2.1: (a) Framework of the SSZ-13 cage, made up of four-, six- and eight-membered rings (MR), and HSE06-optimized structures of (b) 1Al and 2Al Pd-exchanged sites and (c) hydrated sites.

symmetry distinct T-site; therefore, substitution of a single Si^{IV} with Al^{III} encompasses all Z-structures. Pd^{I} and $[PdOH]^{+}$ can reside either in the 6MR or 8MR of the 1Al site, hence we compared the energies of both of these configurations using DFT with the GGA-PBE and HSE06 functionals. We observed that Pd^{I} prefers to locate in the 6MR, bound to two zeolitic framework oxygen (O_f) proximal to Al (Al-O_f) and one Si-O_f, with Pd-O_f bond lengths ranging from 2.18 to 2.38 Å. Pd-OH favors the 8MR, attached to two Al-O_f, with similar Pd-O_fAl bond distances of ~2.09 Å, for both PBE and HSE06. Both species have a three-fold coordinated geometry as shown in **Figure 2.1b**.

Incorporation of two Al results in multiple configurations, which can be codified by Al-Al distance and the number of T-sites separating the Al pair, denoted as nearest neighbors (NN).[89] **Figure 2.2** reports the lowest energy structure computed using the PBE functional for each of the 25 possible Al-Al configurations in a 36 T-site supercell adhering to Löwenstein's rule[90,91] (structures are included in the supporting

information CONTCARS attachment); full results are detailed in supporting information 2.1.1-1. We also optimized a subset of structures using HSE06; relative energies were analogous for both functionals (supporting information 2.1.1-2). Pd^{II} displays a proclivity for Al pairs in the same 6MR; the lowest energy corresponds to that of the 6MR 3NN configuration where Pd^{II} is present in the center of the ring and connected to four Al-O_f. This is followed by the 2NN (+65 kJ mol^{-1}) configuration, with the Pd bonded to three Al-O_f and one Si-O_f. Similar to common configurations observed for Pd^{II} homogeneous complexes, Pd has a four-fold coordinated, planar geometry with Pd-O bond distances of ~2Å in these configurations.[44,64,92,93] The other Al pair configurations are +110–210 kJ mol^{-1} higher in relative energy. Cu^{II} and Co^{II} have been observed to preferentially locate to 2Al 6MRs in SSZ-13 and our computed results for Pd^{II}, which is of similar size, are consistent with this observation.[89,94–101]

To compare the energetics of 1Al and 2Al Pd-exchanged sites, we evaluated the energy required to transfer the Pd cation from the 2Al site to 1Al. Since this mechanism is not unique, we considered different probable routes by constructing Z_2 and Z sites in the same, as well as separate, supercells; details of all the reactions considered are provided in supporting information 2.1.2.

$$\left[Z_2Pd^{II}(H_2O)\right] \rightarrow \left[ZPd^{II}OH\right] / \left[ZH\right] \quad \Delta E = +85 \text{ kJ mol}^{-1} \tag{2.1}$$

$$\left[Z_2Pd^{II}\right] + \frac{1}{2} H_2O - \frac{1}{4} O_2 \rightarrow \left[ZH\right]/\left[ZPd^{I}\right] \quad \Delta E = +82 \text{ kJ mol}^{-1} \tag{2.2}$$

Computed reaction energies are endothermic and indicate a Pd cation will preferentially exchange at 6MR Z_2 sites instead of forming $[ZPd^{I}]$ or $[ZPd^{II}OH]$.

Since Pd preferentially locates at 6MR 2Al sites, identical to Cu and Co, we utilized previously reported and validated models for Al distribution in CHA for common

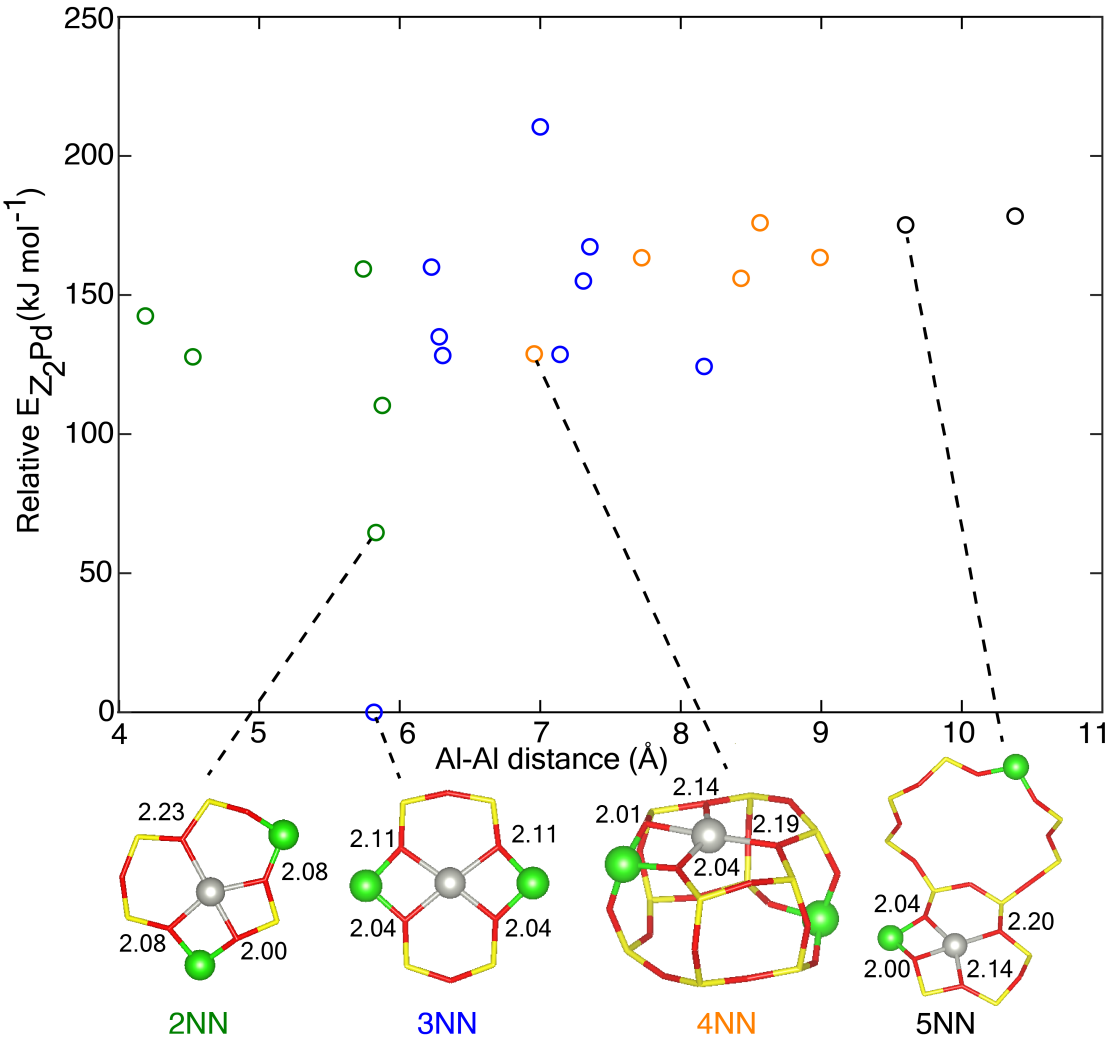

Figure 2.2: Z_2Pd energy vs Al-Al distance, relative to the lowest energy 3NN 6MR structure, based on PBE calculations. Only the lowest energy structure in each of the 25 Al-Al arrangements complying with Löwenstein's rule have been plotted. The Pd-O_f bond lengths (in Å) in each nearest-neighbor (NN) configuration are shown.

syntheses to estimate the Pd/Al ratio, expressed as a function of Si/Al, at which all 6MR 2Al sites would be saturated.[94,101,102] Cation-exchanged Pd/SSZ-13 materials used in the experiments described below (Si/Al = 9, 15, and 17, and Pd/Al = 0.016, 0.032, 0.056, and 0.046), and reported elsewhere, fall well below the threshold of Pd/Al necessary to saturate all 6MR 2Al sites (Si/Al = 9, Pd/Al = 0.146, and Si/Al = 15, Pd/Al = 0.092, Si/Al = 17, Pd/Al = 0.081).[94] We next confirmed the absence of [ZPd^{II}OH] by comparing IR spectra of H/SSZ-13 and Pd/SSZ-13 under dry conditions. Similar FTIR characterization for Cu/SSZ-13 showed the appearance of $[CuOH]^+$ at 3660 cm^{-1} in materials with Cu:Al > 0.21.[94] Our DFT computed harmonic frequency for the O-H stretch in [ZPd^{II}OH] is an analogous 3661 cm^{-1}. Thus, a feature for $[PdOH]^+$ at a similar frequency would appear in the FTIR spectra of Pd/SSZ-13 sample, should it contain a population of [ZPd^{II}OH] sites. To validate this hypothesis, we synthesized and characterized ion-exchanged Pd/SSZ-13 zeolites (Si/Al = 9 and 15, and Pd/Al = 0.016, 0.032 and 0.056) using a modified ion-exchange method.[64] Full details of the synthesis and characterization are reported in section 2.4.4. We pretreated all H/SSZ-13 and Pd/SSZ-13 samples at 873 K in 10% O_2 for 1 hour, and then collected diffuse reflectance infrared Fourier-transform spectra (DRIFTS) at 473 K in 10% O_2. As illustrated in **Figure 2.3a**, we observed features attributed to Brønsted sites at 3600 cm^{-1} and 3580 cm^{-1}, and silanol at 3730 cm^{-1}.[102–104] We do not observe a difference in the peak intensity around 3660 cm^{-1} between the H/SSZ-13 and Pd/SSZ13 materials. The absence of a new feature at 3660 cm^{-1}, where other M-OH stretches have been observed,[94] along with our DFT-computed $[PdOH]^+$ frequency, implies an absence of [ZPd^{II}OH]. Taken together, our results indicate that, in the absence of other adsorbates, exchanged Pd ions are solely [Z_2Pd^{II}] at the 6MR 2Al sites. This observation is consistent across all synthesized samples with varying Si/Al and Pd/Al ratios (supporting information 2.1.3).

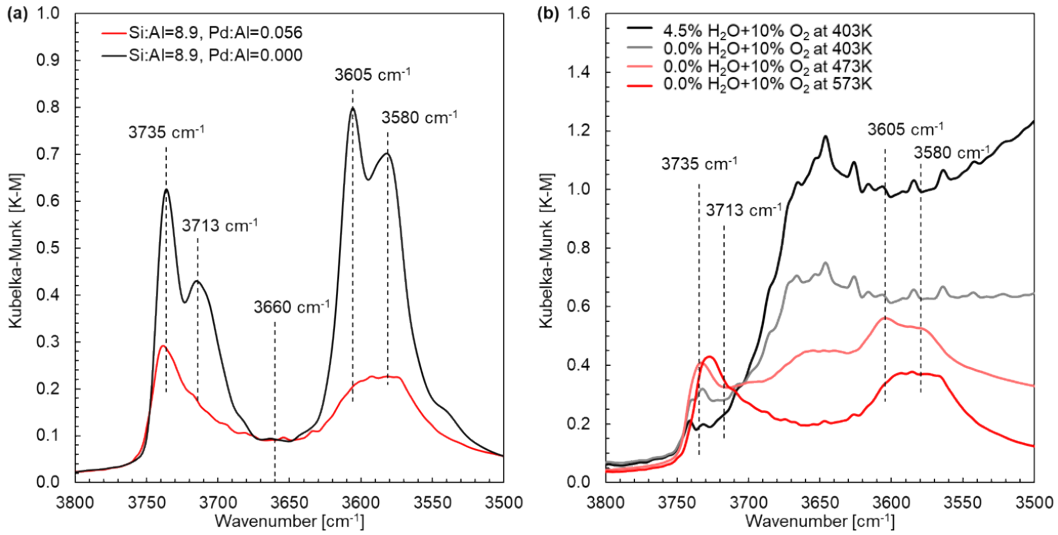

Figure 2.3: (a) Ex-situ DRIFTS spectra of Pd/SSZ-13 (red solid line) and H/SSZ-13 (black solid line) collected at 473 K in 10% O_2 after 873 K 10% O_2 pretreatment. (b) EXAFS spectra of Pd/SSZ-13 collected at: 298 K after exposed to ambient (blue); 473 K with 10% O_2 and 3.1% H_2O (light purple); 573 K with 10% O_2 and 3.1% H_2O (light blue); 773 K with 10% O_2 and 4.5% H_2O (pink); 473 K after dehydration in 10% O_2 at 873 K (red).

2.2.2 Pd Speciation in the Presence of H_2O

To follow the coordination of H_2O with exchanged Pd at 1Al and 2Al sites, we computed the structures and adsorption energies of xH_2O molecules (x = 1 - 6) on three commonly proposed Pd cation motifs: [Z_2Pd^{II}], [$ZPd^{II}OH$], and [ZPd^{I}].[13,66,67,87,105]

$$1Al : ZPd^{I}(H_2O)_{(x-1)} + H_2O \xrightarrow{\Delta E_{ads}} ZPd^{I}(H_2O)_x \tag{2.3}$$

$$ZPd^{II}(OH)(H_2O)_{(x-1)} + H_2O \xrightarrow{\Delta E_{ads}} ZPd^{II}(H_2O)_x \tag{2.4}$$

$$2Al : Z_2Pd^{II}(H_2O)_{(x-1)} + H_2O \xrightarrow{\Delta E_{ads}} Z_2Pd^{II}(H_2O)_x \tag{2.5}$$

The lowest energy structures for each of the xH_2O adsorbed geometries obtained after AIMD simulations, (full details in section 2.4.1) were computed using both PBE and

Table 2.1: H_2O Adsorption Energies (ΔE_{ads}), and Mobilities and Coordination Numbers of Pd sites with xH_2O (x = 1 - 4), Calculated Using HSE06-D3(BJ)vdw[a].

		$+xH_2O$			
adsorption site		$x = 1$	$x = 2$	$x = 3$	$x = 4$
$[ZPd^{I}]$	ΔE_{ads} (kJ mol^{-1})	-105	-76	-77	-63
	O_f / CN	2/3	0/2	0/3	0/4
	mobility	0.8	2.2	1.4	1.8
$[ZPd^{II}OH]$	ΔE_{ads} (kJ mol^{-1})	-147	-53	-126	-71
	O_f / CN	2/4	1/4	0/4	0/4
	mobility	0.4	1.0	1.4	2.6
$[Z_2Pd^{II}]$	ΔE_{ads} (kJ mol^{-1})	-52	-127	-88	-87
	O_f / CN	3/4	2/4	1/4	0/4
	mobility	0.2	0.4	0.4	1.0

[a]CN and O_f denote the coordination number of Pd and the number of zeolitic framework oxygen bonded to it, respectively.

HSE06 functionals with the Becke-Johnson damping method (D3(BJ)vdw) included for dispersion corrections. HSE06 calculation results are summarized in **Table 2.1**. Calculated energies are similar for PBE and HSE06 (supporting information 2.2.1-1, and optimized structures are in the supporting information CONTCARS attachment) and show good agreement with reported PBE adsorption energies of xH_2O (x = 1 - 4) ligands on $[ZPd^{II}OH]$ and $[ZPd^{I}]$ sites in H/BEA zeolite, and $x = 1$ on the $[Z_2Pd^{II}]$ site in SSZ-13.[64,66,86] Normalized Pd oxidation states evaluated using Bader charge analysis are detailed in supporting information 2.2.1-2.

Hydration of $[Z_2Pd^{II}]$ facilitates the movement of the Pd ion from 6MR (**Figure 2.1b**) to 8MR and finally, to the center of the zeolite cage (**Figure 2.1c**). Each H_2O molecule adsorbed replaces the zeolitic framework oxygen (O_f), until at $x = 4$, the

Pd^{II} cation detaches from the framework, attaining a four-fold, square planar geometry, which is commonly observed in Pd-organometallic complexes.[44,64,92,93] Additional H_2O molecules ($x = 5$, 6) are physisorbed on the completely hydrated Pd complex, without altering the coordination chemistry and are ignored in the subsequent calculations. [$ZPd^{II}OH$] displays identical behavior and coordination chemistry with H_2O, forming a four-fold, square planar hydrated Pd complex at $x = 3$ as shown in **Figure 2.1c**. In contrast to the Pd^{II} species, [ZPd^{I}] evidences a different coordination behavior with H_2O. Adsorption of a single H_2O molecule on Pd^{I} forms a two-fold coordinated linear complex, still attached to the zeolite framework. Subsequently adsorbed H_2O molecules change the Pd^{I}-hydrated complex to a linear, two-fold coordinated geometry, followed by three-fold and four-fold coordinated structures, separated from the zeolite framework. These H_2O-solvated Pd complexes, detached from the zeolite framework and mobile, have not been considered in the previous Pd/zeolite literature.

To further quantify the observed H_2O-promoted Pd mobility in the zeolite cage, we resolved the supercell into a 0.2 × 0.2 × 0.2 Å grid, and accounted for the number of cubes the Pd ion moved to during the course of an AIMD simulation at 298 K. The count was scaled by the grid volume and normalized by the scaled volume of $Z_2[Pd^{II}(H_2O)_4]$ (Pd mobility = 1.0). **Table 2.1** reports the results of the mobility analysis; we generally observe that Pd mobility is enhanced as the degree of hydration is increased. There is however, a notable exception; the Pd mobility of $Z[Pd^{I}(H_2O)_2]$ is higher than $Z[Pd^{I}(H_2O)_3]$ owing to the former's H_2O-solvated linear two-fold coordinated structure, which can traverse the zeolite cage more easily due to its smaller size.

We also considered hydration of Pd bonded to O or H ligands that have been proposed in the literature, such as PdO and PdO_2.[11,64,85,87,106] Details of all 21 Pd species

evaluated at 1Al and 2Al sites and their H_2O adsorption energies are provided in supporting information 2.2.1-2. We then compared their relative stabilities expressed as a function of temperature and chemical potentials of hydrogen and oxygen, referenced to H_2O and O_2, respectively. $\mathbf{Z}_*$ represents Z and Z_2 sites.

$$Z_*Pd + \frac{x}{2}\left(H_2O - \frac{1}{2}O_2\right) + \frac{y}{2}O_2 \xrightarrow{\Delta G_{form}} Z_*PdH_xO_y \quad (2.6)$$

The formation free energies (Δ G_{form}) of the $Z_*PdH_xO_y$ species are estimated using HSE06-D3(BJ)vdw and thermodynamic correlations described in section 2.4.2. We used the HSE06-computed energy of the exchange reaction (eq 2.1) reported in section 2.2.1 for the formation of $[ZPd^{II}OH]$ from $[Z_2Pd^{II}(H_2O)]$, to offset their 0 K energies, and collate the 1Al and 2Al structures on a common energy scale, with $[Z_2Pd^{II}]$ defined as the zero of energy. **Figure 2.4a** illustrates the formation free energies at low temperature (condition 1, 298 K, 4.5% H_2O, and 10% O_2) and elevated temperature (condition 2, 773 K, 3.1% H_2O, and 10% O_2). These temperatures are characteristic of NO storage and release in PNAs, catalytic CO and hydrocarbon oxidation, and Wacker oxidation[11,13,15,66,67,77,85,86,105,107–109] and allow comparison of our computations with DRIFTS and X-ray absorption spectroscopy (XAS) data. The lowest free energy species at 298 K (condition 1) from **Figure 2.4a** is $Z_2[Pd^{II}(H_2O)_4]$, followed by $[Z_2Pd^{II}(H_2O)_3]$ which is +32 kJ mol^{-1} higher in energy. Formation of other Pd species at the 2Al site, such as $[Z_2Pd^{II}]$, $[Z_2Pd^{III}O]$ and $[Z_2Pd^{II}O_2]$ are all endergonic, with $[Z_2Pd^{III}O]$ being the least favorable species at this temperature. The lowest free energy structure at the 1Al site is $Z[Pd^{II}(OH)(H_2O)_3]$, while the hydrated form of a Pd^{I} ion at the same site, $Z[Pd^{I}(H_2O)_4]$, is endergonic by +51 kJ mol^{-1}. This is followed by species of varying degrees of hydration of $[ZPd^{I}]$ and $[ZPd^{II}O_2]$ at the 1Al site. As the temperature is increased to 773 K (condition 2), the free energies of all

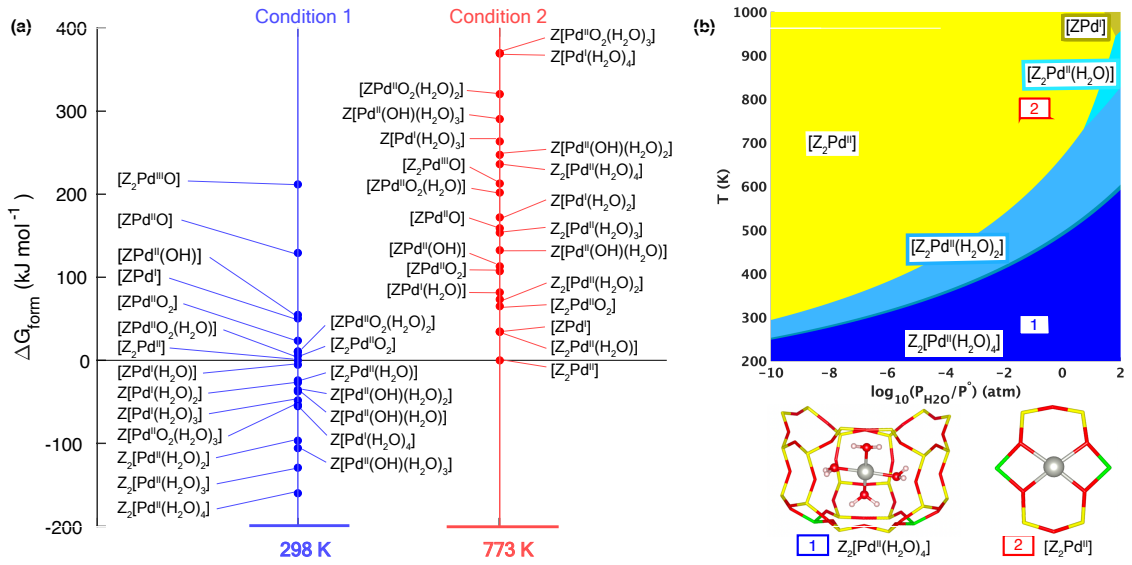

Figure 2.4: (a) Formation free energies (ΔG_{form}) of Z* PdH_x O_y species at 1Al and 2Al sites represented on a common energy scale at condition 1 (298 K, 4.5% H_2O, 10% O_2), and condition 2 (773 K, 3.1% H_2O, 10% O_2), and (b) Thermodynamic phase diagrams for 1Al and 2Al Pd-exchanged sites on a common energy scale based on HSE06-D3(BJ)vdw calculated energies. (The low and high temperature conditions are labeled accordingly on the phase diagrams with the structures shown for the corresponding minimum free energy species)

the hydrated species increase significantly, leaving $[Z_2Pd^{II}]$ as the most stable species at the 2Al site, and $[ZPd^{I}]$ at the 1Al site.

We extended the results of **Figure 2.4a** to formulate a combined phase diagram for $Z_*PdH_xO_y$ shown in **Figure 2.4b**, plotted over a range of temperatures and H_2O pressures at 10% O_2. HSE06-computed phase diagrams of individual 1Al and 2Al sites are shown in supporting information 2.2.1-3. Conditions 1 and 2 considered in **Figure 2.4a** are labeled on the phase diagram. The lowest energy species at low temperature and high H_2O pressure are the completely hydrated $Z_2[Pd^{II}(H_2O)_4]$ complexes; as the temperature is increased, waters of hydration desorb, giving the adsorbate-free $[Z_2Pd^{II}]$.

To validate the predicted characteristics of Pd cations we performed in-situ XAS

experiments on a Pd/SSZ-13 sample (Si/Al = 17, Pd/Al = 0.046) at 298 K after ambience exposure, 473 K and 773 K in the presence of 10% O_2 and 3.1% H_2O, and at 473 K following dehydration at 873 K in 10% O_2. The extended X-ray absorption fine structure (EXAFS) spectra are shown in **Figure 2.3b** and additional details of the XAS experiments and fitting are reported in supporting information 2.2.2-1. We do not observe EXAFS features associated with higher shell Pd-O-Pd scattering in any of the collected spectra, confirming the absence of PdO nanoparticles in our materials, and X-ray absorption near edge structure (XANES) results show a similar edge energy to a $Pd^{II}O$ standard, confirming all cations have an oxidation state of 2+.

We observe a first shell Pd-O bond distance of 2.01±0.1 Å with a coordination number of 4.0±0.3, and absence of second shell scatter after exposure to either ambience at 298 K or to 10% O_2 and 3.1% H_2O at 473 K (blue lines). These spectra are equivalent to those of homogeneous aqueous Pd^{II} and Cu^{II} ions.[110,111] Our results are in agreement with the phase diagram prediction shown in **Figure 2.4b,** and support the formation of H_2O-solvated $Z_2[Pd^{II}(H_2O)_4]$ complexes detached from the zeolite framework.

EXAFS spectra collected at 773 K in 3.1% H_2O and 10% O_2 (pink line), or at 473 K following treatment at 873 K in 10% O_2 and 0% H_2O (red line), exhibit second shell scattering (attributed to framework Si/Al)[94] and a slightly lower Pd-O coordination number, similar to dehydrated Cu/SSZ-13.[94] We interpret these results as the dehydration of $Z_2[Pd^{II}(H_2O)_4]$ to $[Z_2Pd^{II}]$ at 773 K in the presence of 3.1% H_2O, in agreement with the phase diagram prediction shown in **Figure 2.4b**. In-situ DRIFTS dehydration experiments reported in supporting information 2.1.3 Figure S3b, show similar trends in dehydration temperature.

2.2.3 Pd Speciation During NO Adsorption

We next follow Pd coordination chemistry in the presence of NO and H_2O.

2.2.3.1 NO Adsorption Energies

We computed NO adsorption energies, in the presence and absence of $x$$H_2O$ (x = 0 - 3), at the 1Al and 2Al Pd sites employing the AIMD and geometry optimization protocols described in section 2.4.1 using both PBE-D3(BJ)vdw and HSE06-D3(BJ)vdw per the following reactions:

$$1\text{Al} : \text{ZPd}^{\text{I}}(\text{H}_2\text{O})_x \; + \; \text{NO} \xrightarrow{\Delta E_{\text{ads}}} \text{ZPd}(\text{H}_2\text{O})_x(\text{NO}) \tag{2.7}$$

$$\text{ZPd}^{\text{II}}(\text{OH})(\text{H}_2\text{O})_x + \text{NO} \xrightarrow{\Delta E_{\text{ads}}} \text{ZPd}^{\text{II}}(\text{OH})(\text{H}_2\text{O})_x(\text{NO}) \tag{2.8}$$

$$2\text{Al} : \text{Z}_2\text{Pd}^{\text{II}}(\text{H}_2\text{O})_x + \text{NO} \xrightarrow{\Delta E_{\text{ads}}} \text{Z}_2\text{Pd}^{\text{II}}(\text{H}_2\text{O})_x(\text{NO}) \tag{2.9}$$

Full details and structure files along with the Pd oxidation states assessed by HSE06-computed Bader charges can be found in supporting information 2.3.1-1, and the CONTCARS attachment. **Table 2.2** reports the computed NO binding energies; depending on the choice of functional, we observe differences as large as +99 kJ mol^{-1} for the same structure, in contrast with H_2O binding energies (supporting information 2.2.1-1). The significant disparity in NO adsorption energies is consistent with observations in the literature, which concur that GGA methods tend to overestimate the exothermicity of NO binding energies on Cu/SSZ-13 zeolites by $>$ 90 kJ mol^{-1}.[112–114]

Regardless of the functional used, NO binding energies display similar qualitative trends, with [Z_2Pd^{II}] being the least, and [ZPd^{I}] the most exothermic. Geometries

Table 2.2: NO Adsorption Energies (ΔE_{ads}), and Mobilities and Coordination Numbers of Pd sites in the Absence and Presence of $x$$H_2O$ Molecules (x = 0 - 3), Calculated Using PBE-D3(BJ)vdw and HSE06-D3(BJ)vdw[a].

			$+xH_2O$			
adsorption site			$x = 0$	$x = 1$	$x = 2$	$x = 3$
$[ZPd^{I}(NO)]$	ΔE_{ads} (kJ mol^{-1})	PBE	-272	-239	-240	-224
		HSE06	-175	-142	-141	-146
	O_f / CN		3/4	2/4	0/3	0/4
	mobility		0.4	1.6	1.6	0.8
$[ZPd^{II}OH(NO)]$	ΔE_{ads} (kJ mol^{-1})	PBE	-195	-126	-157	-99
		HSE06	-140	-58	-103	-37
	O_f / CN		2/4	1/4	0/4	0/4
	mobility		0.4	0.6	0.4	0.8
$[Z_2Pd^{II}(NO)]$	ΔE_{ads} (kJ mol^{-1})	PBE	-123	-150	-120	-123
		HSE06	-70	-106	-60	-68
	O_f / CN		4/4	2/4	1/4	0/4
	mobility		0.2	0.4	0.4	0.2

[a]CN and O_f denote the coordination number of Pd and the number of zeolitic framework oxygen bonded to it, respectively.

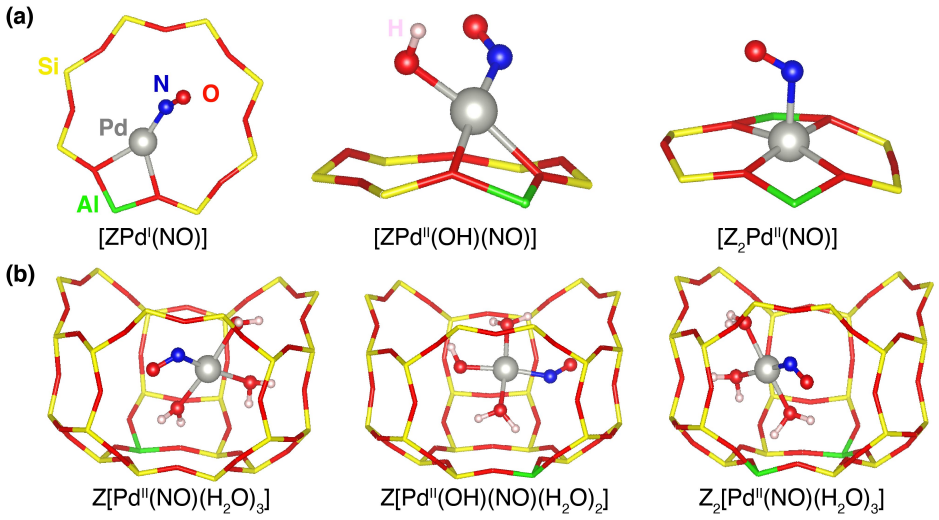

Figure 2.5: HSE06-optimized structures of (a) NO adsorbed on 1Al and 2Al Pd-exchanged sites, and (b) NO adsorbed in the presence of H_2O.

of NO-adsorbed species at 1Al and 2Al Pd sites, optimized using both PBE and HSE06 functionals, yield similar structures; HSE06-optimized structures are shown in **Figure 2.5a**. Khivantsev et al. reported a similar PBE NO binding geometry and energy on [Z_2Pd^{II}] in the 6MR.[64,66] However, for [$ZPd^{II}OH$] and [ZPd^{I}], we found that NO causes relocation of the Pd cation to a lower energy minima for both PBE and HSE06. [$ZPd^{II}OH$], initially present in the plane of the 8MR, moved to the periphery of the 6MR upon adsorbing NO. Likewise, [ZPd^{I}(NO)] migrates to a lower energy geometry in the 8MR, as opposed to the reported 6MR;[64,66] the former being +50 kJ mol^{-1} more exothermic.

Adsorption of subsequent H_2O break the Pd-O_f bonds, eventually forming the favored four-fold coordinated, square planar hydrated Pd-nitrosyl complex at the center of the zeolite cage, at $x = 2$ in [ZPd^{II}(OH)], and x= 3 in [ZPd^{I}] and [Z_2Pd^{II}], shown in **Figure 2.5b**. Similar to Cu-mixed ligand mobile complexes,[115] the hydrated Pd-nitrosyl complexes exhibited Pd mobility (normalized to $Z_2[Pd^{II}(H_2O)_4] = 1.0$) as well, although slightly reduced in comparison to their fully H_2O-solvated analogues.

The NO adsorption energy and optimized structure evaluated by Khivantsev et al. for $[Z_2Pd^{II}(NO)(H_2O)]$ using the PBE functional is consistent with our PBE results.[64,66] Formation of the mobile hydrated Pd-nitrosyl complexes detached from the zeolite framework requires adsorption of at least 2 H_2O for all three models. However, calculations with NO in the presence of >1 H_2O on either $[Z_2Pd^{II}]$ or $[ZPd^{I}]$ and $[ZPd^{II}(OH)]$ have not been reported elsewhere.

To explore the adsorption of multiple NO, we determined the energy to adsorb a second NO molecule on $[ZPd^{I}(NO)]$, $[ZPd^{II}(OH)(NO)]$, and $[Z_2Pd^{II}(NO)]$, using both PBE and HSE06; results are tabulated in supporting information 2.3.1-2 and structures files are provided in the CONTCARS attachment. PBE-computed values parallel those reported in the literature.[64,66,86] HSE06 calculations demonstrate more endothermic energies for adsorption of the second NO on all structures. Moreover, HSE06 calculations showed that the adsorption of a second NO on $[ZPd^{I}(NO)(H_2O)_2]$, $[ZPd^{II}(OH)(NO)(H_2O)]$ and $[Z_2Pd^{II}(NO)(H_2O)_2]$ was comparatively weaker than that of adsorbing a third H_2O molecule on these sites, implying the preferential adsorption of multiple H_2O molecules over multiple NO molecules for H_2O-solvated structures.

We considered NO adsorption on all 21 Pd-bound ligands at the 1Al and 2Al sites considered under hydrothermal conditions and employed thermodynamic analysis to evaluate their relative free energies with O_2, H_2O and NO as the references for oxygen, hydrogen and nitrogen, respectively. The formation free energies (ΔG_{form}) of the $Z_*PdH_xO_y(NO)_z$ species are computed as per section 2.4.2 using both PBE-D3(BJ)vdw and HSE06-D3(BJ)vdw energies, and both exchange reaction energies with both functionals (eqs 2.1 and 2.2).

$$Z_*Pd + \frac{x}{2}\left(H_2O - \frac{1}{2}O_2\right) + \frac{y}{2}O_2 + z\,NO \xrightarrow{\Delta G_{\text{form}}} Z_*PdH_xO_y(NO)_z \quad (2.10)$$

The four resulting thermodynamic phase diagrams are provided in supporting information 2.3.1-3. While both PBE and HSE06 predict the same minimum free energy species, the P_{H_2O} and T range over which the NO-bound species exist differ significantly between the two functionals. To determine which of these two DFT models are accurate, we next turn to coupled cluster theory-computed NO adsorption energies on candidate structures from our thermodynamic analysis.

2.2.3.2 Electronic Structures and Vibrational Frequencies of Pd-NO Structures.

We first constructed two sets of molecular models for the minimum free energy species resulting from our thermodynamic analysis: H_2O-solvated Pd, and zeolite cluster models. For the H_2O-solvated Pd model, we extracted the four-fold coordinated hydrated-Pd complexes, as shown in **Figure 2.1b**, from the PBE-optimized periodic geometries of $Z[Pd^{I}(H_2O)_4]$, $Z[Pd^{II}(OH)(H_2O)_3]$, and $Z_2[Pd^{II}(H_2O)_4]$. Since this model is devoid of the zeolite framework, we compensated the charge by applying an appropriate uniform background charge. Next, we computed the energy required to exchange a single H_2O with NO, forming the hydrated-Pd nitrosyl complexes depicted in **Figure 2.5b**:

$$1Al : Z[Pd^{I}(H_2O)_4] \; + \; NO \xrightarrow{\Delta E} Z[Pd^{II}(H_2O)_3(NO)] + H_2O \tag{2.11}$$

$$Z[Pd^{II}(OH)(H_2O)_3] + NO \xrightarrow{\Delta E} Z[Pd^{II}(OH)(H_2O)_2(NO)] + H_2O \tag{2.12}$$

$$2Al : Z_2[Pd^{II}(H_2O)_4] + NO \xrightarrow{\Delta E} Z_2[Pd^{II}(H_2O)_3(NO)] + H_2O \tag{2.13}$$

The calculated energies required to replace H_2O with NO were then approximated

per the method proposed by Sauer and co-workers,[116–121] and reported in **Table 2.3**:

$$E^{\text{HSE06}}_{\text{supercell}} \approx E^{\text{GGA}}_{\text{supercell}} + E^{\text{HSE06}}_{\text{cluster}} - E^{\text{GGA}}_{\text{cluster}} \tag{2.14}$$

To validate our methodology, we computed cluster model single-point energies using the HSE06 functional and def-2TZVPP basis set for comparison to our supercell HSE06 calculations. Comparison of the HSE06-computed energies for the periodic model with the H_2O-solvated Pd cluster model are within ±9 kJ mol^{-1}, demonstrating that the zeolite-excluded model is reasonably accurate. We also considered another hybrid DFT functional, B3LYP, and found the results agreed with HSE06 within ±15 kJ mol^{-1}. To benchmark our DFT results we performed WFT CCSD(T) calculations, which have been shown to be accurate for transition metal cations such as Cu, Fe, Cr, Ni, etc.[122–128] Computed CCSD(T) energies are reported in **Table 2.3**. We observe that HSE06 and B3LYP hybrid DFT functionals are within ±18 kJ mol^{-1} of the CCSD(T)-computed energies. These results substantiate the reliability of hybrid functionals over GGA for computation of NO binding energies.

Subsequently, we calculated NO adsorption energies on the 1Al and 2Al Pd-exchanged sites in the zeolite cluster model using HSE06 and B3LYP functionals with the def2-TZVPP basis set:

$$1\text{Al} : [\text{ZPd}^{\text{I}}] + \text{NO} \xrightarrow{\Delta E_{\text{ads}}} [\text{ZPd}^{\text{I}}(\text{NO})] \tag{2.15}$$

$$[\text{ZPd}^{\text{II}}(\text{OH})] + \text{NO} \xrightarrow{\Delta E_{\text{ads}}} [\text{ZPd}^{\text{II}}(\text{OH})(\text{NO})] \tag{2.16}$$

$$2\text{Al} : [\text{Z}_2\text{Pd}^{\text{II}}] + \text{NO} \xrightarrow{\Delta E_{\text{ads}}} [\text{Z}_2\text{Pd}^{\text{II}}(\text{NO})] \tag{2.17}$$

Table 2.3: Comparison of Adsorption Energies for the Periodic Model with Zeolite Cluster Models for 1Al and 2Al Pd-exchanged Sites.[a]

	PBE/ PW	HSE06/ PW	HSE06/ def2-TZVPP	B3LYP/ def2-TZVPP	CCSD(T)/ def2-TZVPP	B3LYP/def2-TZVPP NO frequency
	$Z_*[Pd(H_2O)_x] + NO \xrightarrow{\Delta E} Z_*[Pd\ (H_2\ O)_{x-1}(NO)] + H_2O$					
$Z[Pd^{II}(NO)(H_2O)_3]$	-169	-80	-78	-84	-74	1798
$Z[Pd^{II}\ OH(NO)\ (H_2O)_2]$	-49	+14	+23	+17	+5	1878
$Z_2[Pd^{II}(NO)\ (H_2O)_3]$	-52	+12	+6	+6	+8	1986
	$[Z_*PdH_xO_y] + NO \xrightarrow{\Delta E} [Z_*PdH_xO_y(NO)]$					
$[ZPd^{I}(NO)]$	-257	-159	-160	-171	NC	1853
$[ZPd^{II}\ OH(NO)]$	-185	-124	-127	-112	NC	1848
$[Z_2Pd^{II}(NO)]$	-108	-52	-50	-41	NC	1866

[a]All reported energies are in kJ mol^{-1}, and frequencies are in cm^{-1}. NC denotes not calculated and PW plane wave

The CCSD(T) method was not implemented for this model due to the computational expense. **Table 2.3** reports the NO adsorption energies on these cluster models. Analogous to the H_2O-solvated Pd model, energies of the HSE06-computed periodic model are similar to the cluster HSE06 and B3LYP calculations within ±3 kJ mol^{-1}. PBE-computed values vary by 100 kJ mol^{-1} from their hybrid functional counterparts. Our H_2O-solvated and zeolite cluster models showcase good accuracy for the NO energy landscape in Pd/SSZ-13. The structures for both models can be found in the supporting information CONTCARS attachment.

We next evaluated the vibrational frequencies for the species considered in the H_2O-solvated Pd and zeolite cluster models, using B3LYP/def2-TZVPP optimization and frequency calculations. We chose this combination of method and basis set since the scaled[129] gas-phase NO vibrational frequency (1904.0 cm^{-1}) is in close agreement

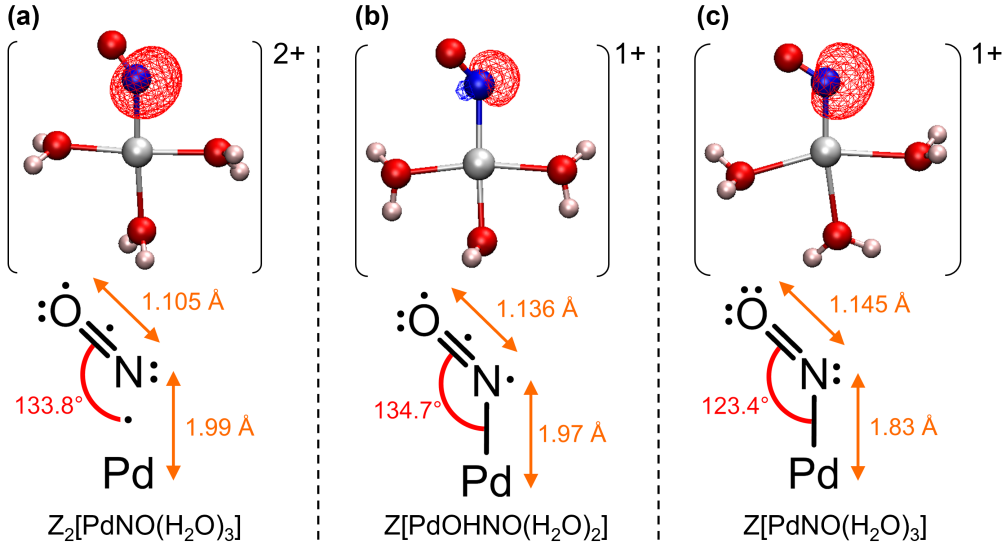

Figure 2.6: CCSD(T) calculated NBOs for B3LYP optimized geometries of (a) $Z_2[PdNO(H_2O)_3]$, (b) $Z[PdOH(NO)(H_2O)_2]$, and (c) $Z[PdNO(H_2O)_3]$. Red and blue isosurfaces indicate the different phases of the NBOs. NBO assigned Lewis dot structures for each species' Pd-NO moiety are beneath their NBO representations, with emphasis on the occupancy of the unbound N valence electrons. Pd-NO bond angles and distances are also displayed. The isovalues used for NBO plots are ±0.15.

with experiment (1904.1 cm^{-1}).[130] **Table 2.3** reports the computed frequencies for each structure, additional details of the calculations can be found in section 2.4.3 and supporting information 2.3.2-1. Nitrosyl frequencies range from 1798 to 1986 cm^{-1}. We demonstrate below that these deviations are closely tied to the electronic structure of the Pd-NO complexes.

To gain insight into the nature of the Pd-NO moieties for H_2O-solvated structures, we performed Natural Bond Order (NBO) analysis[131–137] on the B3LYP optimized structures using CCSD(T)-computed electronic structures. Electron occupancies along with geometries of the Pd-NO moieties are depicted in **Figure 2.6**, and further detailed in supporting information 2.3.2-2. NBO analyses assign neutral nitrosyl ligands for $Z_2[Pd(NO)(H_2O)_3]$ and $Z[Pd(OH)(NO)(H_2O)_2]$, confirming the Bader charge assignment of Pd^{II} for both species. However, localization of the electron densities of N

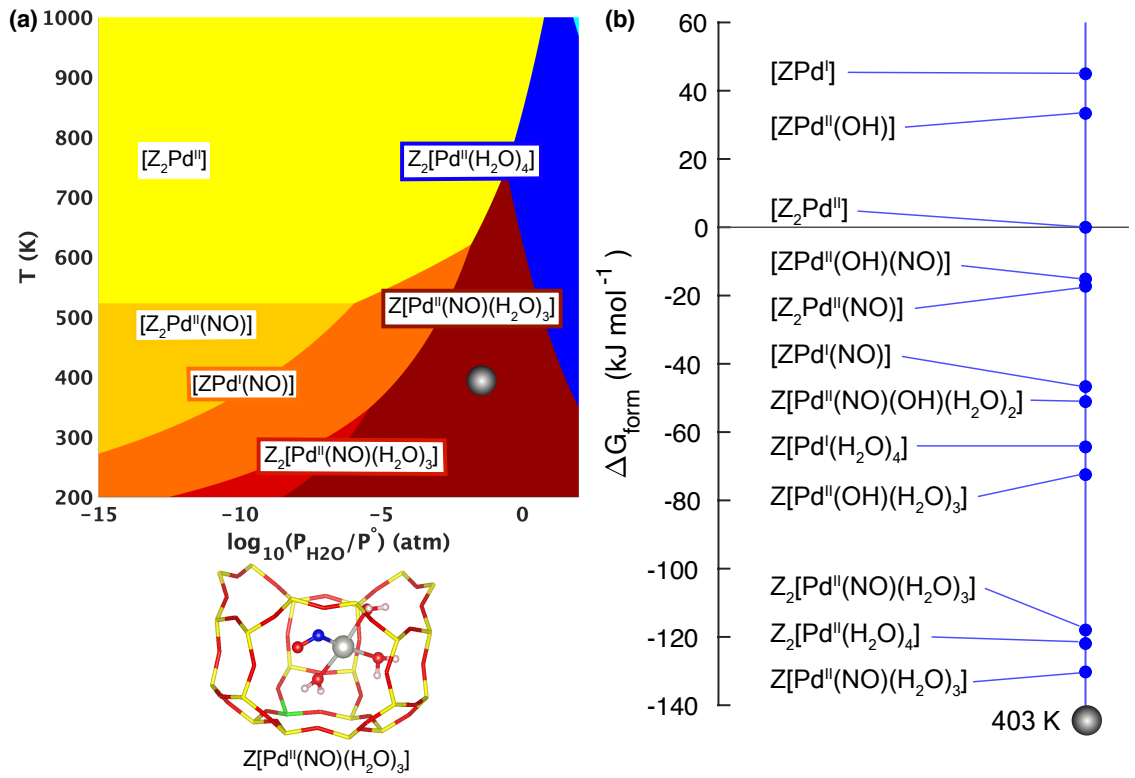

Figure 2.7: (a) Thermodynamic phase diagram for Z∗PdH$_x$O$_y$(NO)$_z$ species at 1Al and 2Al Pd-exchanged sites on a common energy scale incorporating the zero-point, and vibrational free energies, and HSE06-computed energies, and (b) Formation free energies (ΔG_{form}) of Z∗ PdH$_x$O$_y$(NO)$_z$ species at 1Al and 2Al sites represented on a common energy scale at 403 K, 4.5% H_2O, 10% O_2, 200 ppm NO.

and Pd-N bond is different among the two structures. NBO analyses yield electron populations of 1.89 and 0.98 for the N lone pairs, and populations of 0.99 and 1.95 for the Pd-N bonding orbitals, for Z$_2$[Pd^{II}(NO)(H$_2$O)$_3$] and Z[Pd^{II}(OH)(NO)(H$_2$O)$_2$], respectively. This discrepancy elongates the Pd-N distance and shortens the nitrosyl bond length for Z$_2$[Pd^{II}(NO)(H$_2$O)$_3$], resulting in a 100 cm^{-1} increase in its frequency in comparison to Z[Pd^{II}(OH)(NO)(H$_2$O)$_2$]. NBO analysis of Z[Pd(NO)(H$_2$O)$_3$] yields a full lone pair of electrons to the N atom, and a full pair of electrons to the Pd-N bond. NBO results are consistent with an oxidation state of -1 to the nitrosyl ligand (NO$^-$) and 2+ to Pd, which we assign as Z[Pd^{II}(NO$^-$)(H$_2$O)$_3$].

We next incorporated zero-point, and vibrational free energies (detailed in supporting information 2.3.2-3), and HSE06-D3(BJ)vdw-computed energies to formulate a thermodynamic phase diagram of $Z{*}PdH_xO_y(NO)_z$ species. **Figure 2.7a** reports the lowest free energy species as a function of temperature and H_2O partial pressure, with O_2 and NO concentrations of 10% and 200 ppm, respectively. The lowest free energy species in the absence of H_2O and at 298 K is $[Z_2Pd^{II}(NO)]$. Reduction of Pd^{II} to $[ZPd^{I}(NO)]$ is predicted for low P_{H_2O} (-15 < $\log(P_{H_2O}/P^{\circ})$ < -6), amounting to ppm levels of H_2O, at ambient temperatures. $[ZPd^{I}(NO)]$ and $[Z_2Pd^{II}(NO)]$ are close in free energy across this range of P_{H_2O}, and possess similar NO vibrational frequencies, making it difficult to discern which species might be observed during experiments performed in the absence of H_2O. For 1–4.5% H_2O, conditions more representative of application and experiment, the lowest energy species from 298–660 K is $Z[Pd^{II}(NO^{-})(H_2O)_3]$. As temperature increases to 403 K at 4.5% H_2O, the lowest energy species at the 1Al site, $Z[Pd^{II}(NO^{-})(H_2O)_3]$, and the 2Al site, $Z_2[Pd^{II}(H_2O)_4]$ are 8 kJ mol^{-1} apart. The Boltzmann distribution of species at these conditions predicts that 10% of the Pd sites will be H_2O-solvated as $Z_2[Pd^{II}(H_2O)_4]$. The subtle difference in free energy between these two species at 403 K, and between $Z[Pd^{II}(NO^{-})(H_2O)_3]$ and $[ZPd^{I}(NO)]$ near 600 K, are sensitive to the inclusion of vibrational free energies. With further increase in temperature, $Z[Pd^{II}(NO^{-})(H_2O)_3]$ loses water of hydration along with NO to revert to the original adsorbate-free $[Z_2Pd^{II}]$ site at 700 K. Results suggest the following nominal NO adsorption stoichiometry and computed free energy at 4.5% H_2O, 10% O_2 and 200 ppm NO:

$$Z_2[Pd^{II}(H_2O)_4] + NO \xrightarrow[-8\ \text{kJ mol}^{-1}]{\Delta G(403\ K)} Z[Pd^{II}(NO^{-})(H_2O)_3]/[ZH] + \frac{1}{2}\ H_2O + \frac{1}{4}\ O_2 \tag{2.18}$$

Similarly, the NO desorption stoichiometry is:

$$\mathrm{Z[Pd^{II}(NO^{-})(H_2O)_3]/[ZH]} + \frac{1}{4}\ \mathrm{O_2} \xrightarrow[-16\ \mathrm{kJ\ mol^{-1}}]{\Delta G(773\ K)} \mathrm{[Z_2Pd^{II}]} + \frac{7}{2}\ \mathrm{H_2O} + \mathrm{NO} \quad (2.19)$$

Our thermodynamic model thus, predicts a reaction environment-induced change in the number of Al sites charge compensating the Pd cation in the zeolite upon exposure to NO and during subsequent dehydration. The underlying kinetics of this non-elementary process are still unclear.

We next performed isothermal NO adsorption at 353 K followed by temperature programmed desorption (TPD) experiments (30 K/min ramp rate) under 4.5% H_2O, and dry conditions (< 5 ppm H_2O), to qualitatively compare the relative NO binding energies of the most abundant surface intermediates, namely, $[Z_2Pd^{II}(NO)]$ or $[ZPd^{I}(NO)]$ under dry conditions, and $Z[Pd^{II}(NO^{-})(H_2O)_3]$ in the presence of 4.5% H_2O. The NOx-TPD profile from Pd/SSZ-13 under dry conditions before peak deconvolution is shown in supporting information 2.3.2-4, as is the one from H/SSZ-13. Peak deconvolution, also shown in supporting information 2.3.2-4, was performed using these two profiles to separate NO adsorption on Pd-related species from NO interacting with zeolitic AlO_4^{-} sites. As shown in **Figure 2.8**, the majority of NOx desorbs from Pd at temperatures near 500 K under dry conditions, whereas the NOx desorption profile peaks at around 750 K in the presence of 4.5% H_2O. This difference in NO desorption temperatures agrees with the phase diagram prediction in **Figure 2.7b** featuring lower free energy of $Z[Pd^{II}(NO^{-})(H_2O)_3]$ compared to $[Z_2Pd^{II}(NO)]$ or $[ZPd^{I}(NO)]$, and thus a higher NOx desorption temperature in the presence of H_2O (**Figure 2.7a**). In the presence of 4.5% H_2O, we also observed additional NOx adsorption at around 440 K, likely due to the small difference (8 kJ mol^{-1})

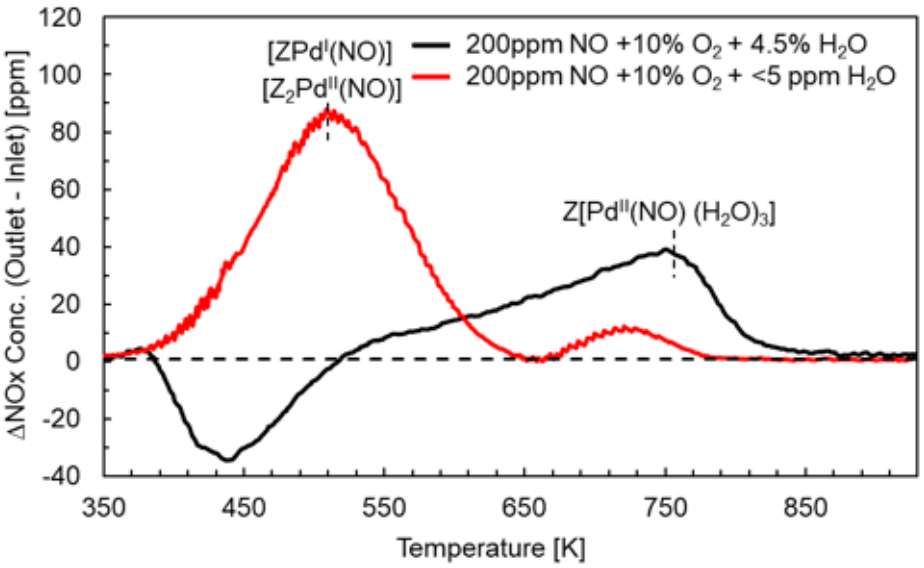

Figure 2.8: NO_x temperature programmed desorption (NO_x-TPD) pro-files of Pd/SSZ-13 (Si/Al = 9, Pd/Al = 0.056) in the presence of 200 ppm NO, 10% O_2, 4.5% H_2O (red) and < 5ppm H_2O (black) at a ramp rate of 30 K/min.

in free energies between $Z_2[Pd^{II}(H_2O)_4]$ and $Z[Pd^{II}(NO^-)(H_2O)_3]$ in this temperature range, or the kinetics of H_2O desorption and NO adsorption. Integrating the desorption peak gives a 1.05±0.1 NO:Pd ratio in the presence of H_2O, in agreement with the HSE06-computed prediction for endothermic adsorption of a second NO on $Z[Pd^{II}(NO^-)(H_2O)_3]$. The free energy calculations discussed above are based on thermodynamics, without considering differences between H_2O and NO adsorption and desorption kinetics. Nevertheless, the difference between NOx-TPD profiles is captured by the computed phase diagram.

2.2.3.3 Experimental IR Frequencies

To further validate the structures predicted by our molecular models, we collected in-situ NO adsorption DRIFTS spectra at 473 K and 403 K in 10% O_2, 200 ppm NO and a wide range of P_{H_2O}. As is shown in **Figure 2.9a,** a spectrum collected at 473 K

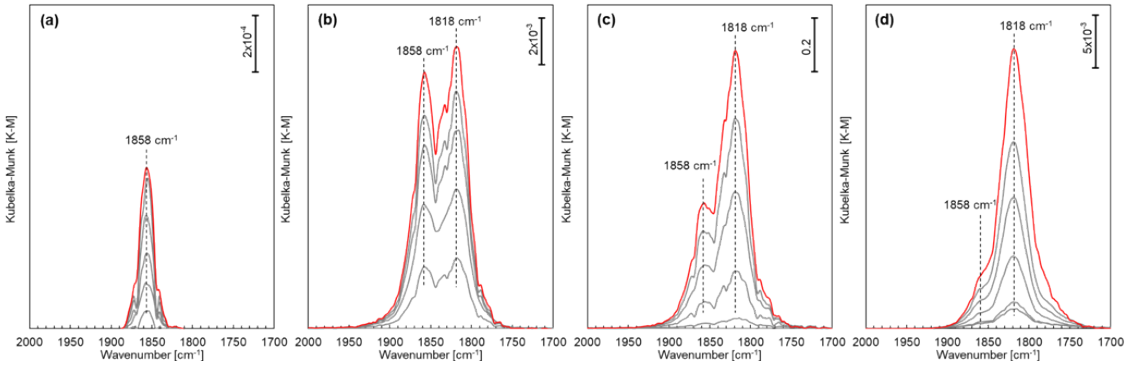

Figure 2.9: In-situ NO adsorption DRIFTS spectra of Pd/SSZ-13 (Si/Al = 9, Pd/Al = 0.056) collected at: (a) 473 K with 200 ppm NO, 10% O_2; (b) 473 K with 200 ppm NO, 10% O_2 and 1.3% H_2O; (c) 403 K with 200 ppm NO, 10% O_2 and 1.3% H_2O; (d) 403 K with 200 ppm NO, 10% O_2 and 4.5% H_2O. Red spectra are the final spectra collected after saturation and grey traces are time resolved spectra collected before saturation with 10 min time intervals. Background spectra were collected at (a) 473 K with 10% O_2; (b) 473 K with 10% O_2 and 1.3% H_2O; (c) 403 K with 10% O_2 and 1.3% H_2O; (d) 403 K with 10% O_2 and 4.5% H_2O.

under dry conditions in the presence of 200 ppm NO and 10% O_2 has an IR absorption peak at 1858 cm^{-1}, and another at 2200 cm^{-1}, the latter is shown in supporting information 2.3.3-1. Peak assignments for the > 2100 cm^{-1} IR features have been widely discussed in the literature, appearing on H-zeolites, and are assigned to stretching of NO^+ interacting with zeolitic AlO_4^- sites.[63,79,138,139] The identity of the Pd-related NO stretching feature at 1858 cm^{-1} can be assigned to either $[Z_2Pd^{II}(NO)]$ or $[ZPd^{I}(NO)]$, substantiated by the DFT-calculated vibrational frequencies of 1866 cm^{-1} and 1853 cm^{-1} in **Table 2.3**. Although we cannot differentiate between $[Z_2Pd^{II}(NO)]$ and $[ZPd^{I}(NO)]$ based on IR frequencies, we posit that only one of these two species should exist under dry conditions due to the single symmetric peak observed.

To determine the effect of H_2O on Pd-NO speciation we collected DRIFTS spectra in the presence of 200 ppm NO, 10% O_2 and 1.3% H_2O at 473 K and 403 K shown in Figure 2.9b,c. We observed the appearance of a new IR feature at 1818 cm^{-1} in

the presence of 1.3% H_2O and the disappearance of the >2100 cm^{-1} features, the latter is shown in supporting information 2.3.3-1 Figures S10-S12. The intensity of the 1818 cm^{-1} peak was larger at the lower temperature. **Figure 2.9d** shows the spectrum collected at 403 K with 200 ppm NO, 10% O_2 and 4.5% H_2O, where the peak intensity at 1818 cm^{-1} increases significantly relative to the peak at 1860 cm^{-1}. A similar peak shift upon addition of H_2O was observed by Chen et. al.[77] We attribute this behavior to the formation of $Z[Pd^{II}(NO^-)(H_2O)_3]$, the lowest free energy species in the presence of H_2O according to the phase diagram in **Figure 2.7,** and the DFT-computed NO vibrational frequency of 1798 cm^{-1} for $Z[Pd^{II}(NO^-)(H_2O)_3]$ in **Table 2.3**. The NO stretching frequency at around 1818 cm^{-1} has been previously reported as $[ZPd^{I}(NO)]$ in the absence of H_2O.[64,66,67] However, our DRIFTS experiments clearly demonstrate that this feature has P_{H_2O} and T dependencies indicating a H_2O-solvated structure. We observed no nitrate or nitrite formation in the presence of percentage-level H_2O and have reported spectra with these regions included in the supporting information 2.3.3-1 Figures S10-S12. Spectra taken (supporting information 2.3.3-1) in the presence of 200 ppm NO, 10% O_2 and 20 ppm H_2O are representative of those reported as being in the absence of H_2O elsewhere.[64]

2.2.3.4 CO Adsorption and Oxidation

The effect of H_2O noted above could also impact other reactions since Pd cations formed in the presence and absence of H_2O are two intrinsically different species. CO has been reported to adsorb on Pd cations in Pd/SSZ-13 and may also contribute to irreversible degradation of PNAs.[13] Therefore, we chose CO adsorption and oxidation as probe reactions to further investigate the H_2O-solvation effect.

We collected DRIFTS spectra in the presence of 200 ppm CO, 200 ppm NO, 10% O_2

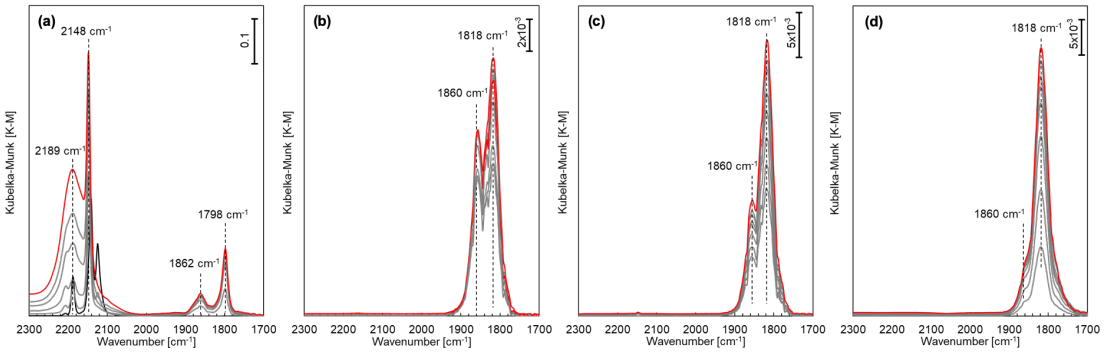

Figure 2.10: In-situ DRIFTS spectra of Pd/SSZ-13 (Si/Al = 9, Pd/Al = 0.056) collected at: (a) 353 K during 200 ppm NO addition after exposure to 10% O_2, 20 ppm H_2O and 200 ppm CO; (b) 403 K during 200 ppm CO addition after exposure to 10% O_2, 1.3% H_2O and 200 ppm NO; (c) 473 K during 200 ppm CO addition after exposure to 10% O_2, 1.3% H_2O and 200 ppm NO; (d) 403 K during 200 ppm CO addition after exposure to 10% O_2, 4.5% H_2O and 200 ppm NO. Background spectra were collected at (a) 353 K with 10% O_2 and 20 ppm H_2O; (b) 403 K with 10% O_2 and 1.3% H_2O; (c) 473 K with 10% O_2 and 1.3% H_2O; (d) 403 K with 10% O_2 and 4.5% H_2O.

and 20 ppm – 4.5% H_2O. At 20 ppm H_2O, CO stretching frequencies appear at 2148 and 2189 cm^{-1} (**Figure 2.10a**), consistent with spectra reported by Khivantsev et al. under similar conditions.[67] However, exposure to 1.3–4.5% H_2O (**Figure 2.10b-d**) causes the disappearance of all CO stretching frequencies (~2100–2300 cm^{-1}), resulting in the recovery of the spectra collected in the absence of CO reported in **Figure 2.9b-d**.

We attribute the vanishing of CO frequencies to the more exothermic binding of NO on Pd as compared to CO, in the presence of H_2O, forming predominantly $Z[Pd^{II}(NO^-)(H_2O)_3]$ under these conditions. The HSE06 computed binding energy of CO is -59 kJ mol^{-1} on $Z[Pd^{I}(H_2O)_4]$, and -80 kJ mol^{-1} for NO (supporting information 2.3.4-1), which supports this hypothesis. Further, replacement of H_2O with CO on $Z[Pd^{II}(NO^-)(H_2O)_3]$ is computed to be endothermic (+44 kJ mol^{-1}), indicating co-adsorption of CO is prohibitive.

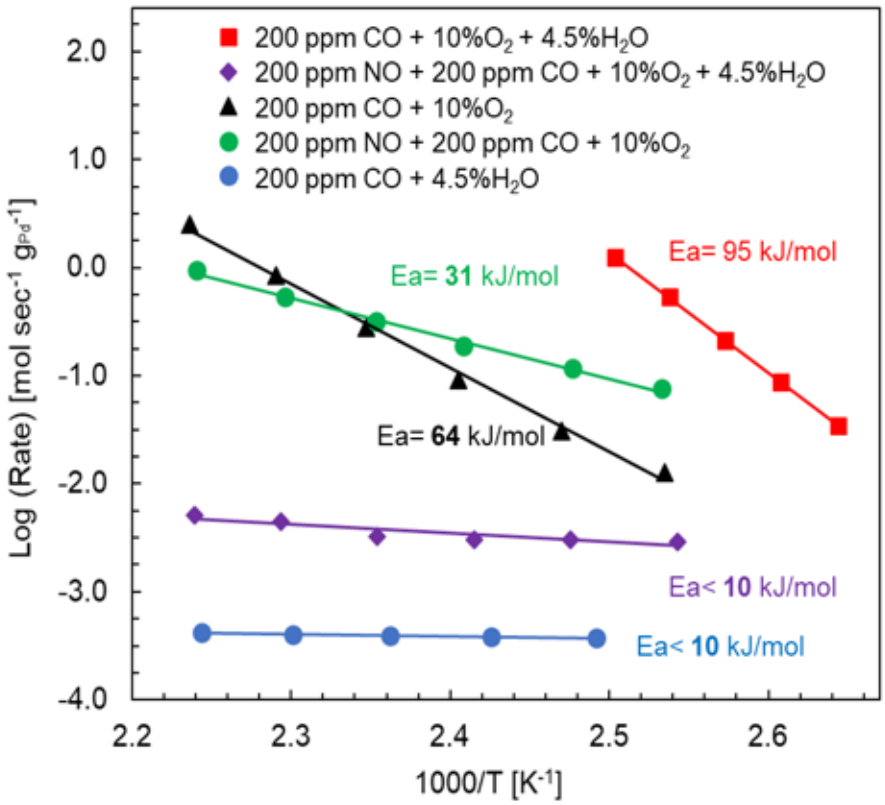

Figure 2.11: CO oxidation rates measured on Pd/SSZ-13 (Si/Al = 9, Pd/Al = 0.056) in the presence of: 200 ppm CO, 10% O_2 and 4.5% H_2O (red square); 200 ppm NO, 200 ppm CO, 10% O_2 and 4.5% H_2O (purple diamond); 200 ppm CO and 10% O_2 (black triangle); 200 ppm NO, 200 ppm CO and 10% O_2 (green circle). Water gas shift rates measured on Pd/SSZ-13 (Si/Al = 9, Pd/Al = 0.056) in the presence of 200 ppm CO and 4.5% H_2O (blue circle).

We performed steady-state CO oxidation experiments between 373 K to 473 K in the presence and absence of 4.5% H_2O, where 200 ppm CO was present at all times (**Figure 2.11,** additional details in supporting information 2.3.4-2). We also measured water gas shift (WGS) activity on the same catalyst to eliminate a possible change in activation energy due to the onset of the WGS reaction (blue circles). CO oxidation rates measured in the presence of 4.5% H_2O are significantly higher than those measured in the absence of H_2O. Formation of Pd nanoparticles is not detected under these conditions Figure S14, additional details in supporting information 2.3.4-3), suggesting H_2O-solvated Pd complexes are the active site for catalytic CO oxidation. The different CO oxidation activation energies further highlight the distinction between H_2O-solvated and dehydrated Pd. This may be due H_2O assisted O_2 activation, or mobilization of Pd cations to form transient multinuclear complexes.[37,40,41,140] **Table 2.1** suggests a possible correlation between Pd cation mobility and CO oxidation activity. We also performed steady-state CO oxidation experiments in the presence of NO, with and without 4.5% H_2O, with 200 ppm CO, 200 ppm NO and 10% O_2. The near-zero CO oxidation activity in the presence of 200 ppm NO and 4.5% H_2O provides further evidence that CO adsorption is prohibitive on $Z[Pd^{II}(NO^{-})(H_2O)_3]$.

Taken together, our results show that CO oxidation is promoted by formation of H_2O-solvated Pd complexes in the absence of NO. However, in the presence of NO and practically relevant H_2O pressures at $\leq$ 473 K CO adsorption is inhibited. We find no evidence to support the formation of $Pd^{II}(NO)(CO)$ complexes under these conditions.

2.2.4 Comparison with ZSM-5 and BEA Zeolites

We have demonstrated that the presence of H_2O leads to the solvation of Pd and Pd-NO complexes. The EXAFS spectrum of H_2O exposed Pd/SSZ-13 reported in **Figure 2.3** lacks second shell scattering at $T \leq 473$ K, which suggests that these hydrated complexes are detached from the zeolite framework. A similar solvation effect induced by NH_3 has also been observed in Cu/SSZ-13. At temperatures lower than 523 K NH_3-solvated Cu complexes form and interact with the zeolite framework through electrostatic tethering.[37,39] Motivated by these observations, we hypothesized that the nature of hydrated Pd-NO complexes within different zeolite frameworks should be similar, although the Pd-NO complexes formed in the absence of H_2O can differ due to differences in initial Pd speciation.

To test this hypothesis, we extended our in-situ NO adsorption DRIFTS experiments on Pd/SSZ-13 (Si/Al = 9, Pd/Al = 0.056) to Pd/ZSM-5 (Si/Al = 15, Pd/Al = 0.094) and Pd/BEA (Si/Al = 12.5, Pd/Al = 0.079), and first performed NO adsorption in the absence of H_2O at 423 K, followed by NO adsorption in the presence of 4.5% H_2O at 353 K. **Figure 2.12** shows that the DRIFTS spectra collected in the absence of water (solid lines) for Pd/BEA and Pd/ZSM-5 are significantly different from Pd/SSZ-13 in terms of both the number of features and their frequencies. NO stretching features at 1881 cm^{-1} and 1836 cm^{-1} on Pd/ZSM-5, and 1849 cm^{-1} on Pd/BEA are consistent with the reported NO stretching features in the Pd/zeolite literature.[11,63,107,141] The primary NO adsorption sites in the absence of H_2O for BEA and ZSM-5 are unknown, and appear to give rise to different NO stretching frequencies and potentially different Pd/zeolite binding energies.[77] Additionally, more than one NO stretching feature is observed with Pd/ZSM-5 and Pd/BEA, indicating more heterogeneous Pd cation speciation resulting from different framework topology and Al distributions compared

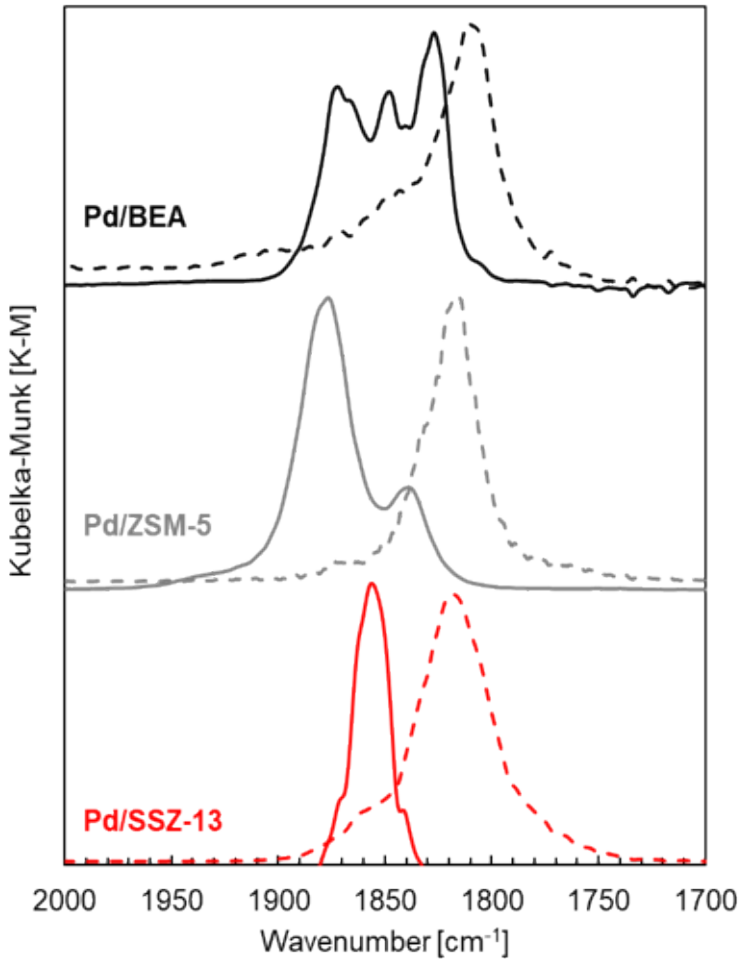

Figure 2.12: In-situ NO adsorption DRIFTS spectra of Pd/SSZ-13 (red), Pd/ZSM-5 (gray) and Pd/BEA (black). Spectra are collected at: 473 K with 200 ppm NO, 10% O_2 (solid line) and 403 K with 200 ppm NO, 10% O_2 and 4.5% H_2O (dashed line) for Pd/SSZ-13; 373 K with 200 ppm NO, 10% O_2 (solid line) and 373 K with 200 ppm NO, 10% O_2 and 4.5% H_2O (dashed line) for Pd/ZSM-5; 353 K with 200 ppm NO, 10% O_2 (solid line) and 353 K with 200 ppm NO, 10% O_2 and 4.5% H_2O (dashed line) for Pd/BEA. Background spectra were collected at: 473 K with 10% O_2 (solid line) and 403 K with 10% O_2 and 4.5% H_2O (dashed line) for Pd/SSZ-13; 373 K with 10% O_2 (solid line) and 373 K with 10% O_2 and 4.5% H_2O (dashed line) for Pd/ZSM-5; 353 K with 10% O_2 (solid line) and 353 K with 10% O_2 and 4.5% H_2O (dashed line) for Pd/BEA. Peak heights are normalized to the intensity of the dominating feature of each spectrum to highlight the difference in peak numbers and positions.

to SSZ-13.[80,142–145] However, DRIFTS spectra collected after NO adsorption in the presence of 4.5% H_2O (dashed lines) show similar IR features regardless of zeolite topology. Dominating features at 1818 cm^{-1} for Pd/SSZ-13, 1814 cm^{-1} for Pd/ZSM-5, and 1808 cm^{-1} for Pd/BEA demonstrate a more homogenized distribution of Pd cations, even though the peak positions of these features are slightly different, likely due to the effect of zeolite cage geometry.[77] This result supports the hypothesis that the hydration of Pd cations causes them to detach from the zeolite and give way to homogenized and H_2O-solvated $Z[Pd^{II}(NO^{-})(H_2O)_3]$ complexes within different zeolite frameworks.

2.3 Conclusions

We show here that Pd ions and Pd-NO complexes are sensitive to environmental conditions and interrogation of their speciation is possible through a combined approach of experiment and computational modeling. Exposure of Pd-zeolites to H_2O and NO causes profound changes that are captured through condition-dependent spectroscopic and kinetic experiments, and by previously unexplored computational models that incorporate H_2O-solvation, AIMD simulations, hybrid-exchange DFT functionals, and WFT calculations. As shown here, GGA functionals, such as PBE, do not accurately describe Pd-NO complexes.

We show that exchanged Pd cations in SSZ-13 zeolites with Si/Al = 9 and Si/Al = 15 preferentially locate to 2Al 6MR sites as $[Z_2Pd^{II}]$, similar to their Cu and Co analogues. In contrast to Cu, and consistent with Co, the computed energies of forming $[ZPd^{II}OH]$ moieties are prohibitive, and we do not detect their presence in any of our materials. Our findings may shed light on experimental difficulties with

exchanging Pd-cations in SSZ-13, especially at higher Si/Al ratios where the density of 2Al 6MR sites may be small. Neither our computational or experimental results suggest the presence of Pd^{I}, or the higher oxidation states Pd^{III} and Pd^{IV} in as-synthesized Pd-zeolites, consistent with prior assertions.[66] Exposure to H_2O at < 573 K solvates and mobilizes Pd ions, similar to observations for Cu/zeolites.[94] Catalytic CO oxidation and IR experiments further emphasize the chemical differences between $[Z_2Pd^{II}]$ and $Z_2[Pd^{II}(H_2O)_4]$. These conditions are similar to those used for catalytic Wacker oxidation (378 K, ~0.3–3% H_2O) on Cu-Pd/zeolite Y:

$$2C_2H_4 + O_2 \rightarrow 2C_2H_4O \tag{2.20}$$

where a H_2O apparent order of 0.73 was measured.[75] Under these conditions we expect both Pd and Cu cations[94] to be H_2O-solvated, and the mobility of both ions could play an important role in the mechanism.

Exposure to NO facilitates transformation from 2Al $\rightarrow$ 1Al Pd-exchange sites. At $<$ 5 ppm of H_2O, both $[Z_2Pd^{II}NO]$ and $[ZPd^{I}NO]$ are close in free energy. Under conditions of more practical relevance, $Z[Pd^{II}(NO^{-})(H_2O)_3]$ becomes the dominant and lowest free energy species, desorbing NO at a higher temperature than its dehydrated counterparts, and prohibits the adsorption of CO. The recognition of H_2O-solvated Pd-nitrosyl complexes unifies disparate and contradictory assignments in the Pd/zeolite literature, draws strong connections to homogeneous Pd inorganic chemistry, and provides a molecularly detailed description of the Pd-complexes relevant to PNA and catalytic oxidation. These solvated Pd-nitrosyl complexes are less mobile than their fully H_2O-solvated counterparts, which may have mechanistic consequences for CO oxidation, and could be beneficial for preventing Pd deactivation processes in these materials.

Zeolites of varying topology evidence a heterogeneous distribution of Pd-NO complexes that coalesce into one spectral feature upon exposure to H_2O. Although reported NO adsorption and desorption concentration vs time profiles, and NO desorption temperatures, vary with zeolite topology, the formation of homogeneous-like nitrosyl complexes among multiple zeolites potentially removes one of the constraints for optimizing PNA materials.

Our results suggest the following nominal stoichiometry for NO adsorption/desorption processes:

$$\xrightarrow{\text{temperature}} \qquad (2.21)$$

$$Z_2[Pd^{II}(H_2O)_4] \underset{-OH}{\overset{+NO}{\rightleftharpoons}} Z[Pd^{II}NO^{-}(H_2O)_3]/[ZH] \underset{-3H_2O,\ -H,\ -NO}{\rightleftharpoons} [Z_2Pd^{II}]$$

This cascade is obviously non-elementary and involves activated processes for NO adsorption and desorption. The transport and kinetics of these adsorption and desorption processes are likely influenced by zeolite topology, but their mechanistic details remain unclear. Nevertheless, our results provide the thermodynamic roadmap for future mechanistic studies. Our findings underscore the importance of environmental conditions in the formation of metal complexes in zeolites, and the need for experimental and computational approaches that interrogate their chemical nature under practical conditions.

2.4 Methods

2.4.1 Details of DFT and AIMD Calculations

We performed periodic DFT calculations employing a plane-wave basis set with an energy cutoff of 400 eV, and a triclinic SSZ-13 supercell consisting of 24 T-sites for 2Al Pd-exchanged sites. We performed calculations in both 12 and 24 T-site supercells for the 1Al Pd-exchanged sites reported in supporting information 4.1.1 and found that the energies were consistent irrespective of the supercell size. Hence, we used the 12 T-site supercell for the 1Al Pd-exchanged sites to avoid unnecessary computational expense. Since the zeolitic system is an insulator, we considered only the Γ point for sampling the first Brillouin zone. To determine plausible local minima of the structures studied, we carried out spin-polarized ab initio molecular dynamics (AIMD) simulations beginning with initial guess structures in the NVT ensemble using the Vienna ab initio Simulation Package (VASP),[146] version 5.4.4. Simulations of at least 60 ps, with a time step of 0.5 fs, were run at temperatures of 298 K and 473 K applying the Perdew-Becke-Ernzerhof (PBE)[147] generalized gradient approximation (GGA) exchange-correlation functional coupled with Becke-Johnson damping (D3(BJ)vdw) dispersion correction method.[148,149]

Thereafter, we optimized five low energy structures selected from the AIMD simulations, first with GGA-PBE functional and subsequently with the Heyd-Scuseria-Ernzerhof (HSE06)[146–153] hybrid functional for computational efficacy. All geometry optimizations were spin-polarized with the projector augmented wave (PAW) method used for computing core-valence interactions,[154,155] along with the D3(BJ)vdw correction. We used a convergence criterion of 10^{-8} eV and 0.01 eV/Å for self-consistent-field (SCF) electronic energies and atomic forces, respectively. We applied the Bader

charge method[156–160] on HSE06-optimized structures to compute the oxidation state of Pd, represented as a superscript on Pd. The obtained charges were normalized to Pd^{I} and Pd^{II} using [ZPd^{I}] and [Z_2Pd^{II}] as references, and rounded to the nearest integer. All the optimized geometries have been provided in the supporting information CONTCARS attachment.

2.4.2 Calculation of Ab Initio Formation Free Energies

We expressed the formation free energies of the adsorbed species involving O and H atoms, as a function of the reaction conditions and the DFT-calculated energies using O_2 and H_2O as references:[161,162]

$$\Delta G^{\text{form}}_{x,y}\ (T, \Delta\mu_{O_2},\ \Delta\mu_{H_2O}) = \Delta E^{\text{form}}_{x,y} - T\ \Delta S^{\text{ST}}_{x,y}\ (T)\ -\ \frac{x}{2}\left(\Delta\mu_{H_2O}\ -\ \frac{1}{2}\ \Delta\mu_{O_2}\right) - \frac{y}{2}\ \Delta\mu_{O_2} \quad (2.22)$$

$$\Delta E^{\text{form}}_{x,y} = \Delta E_{Z_*PdH_xO_y} - \Delta E_{Z_*Pd} - \frac{x}{2}\ \left(\Delta E_{H_2O} - \frac{1}{2}\ \Delta E_{O_2}\right) - \frac{y}{2}\ \Delta E_{O_2} \quad (2.23)$$

$\Delta\mu$ represents the difference in the chemical potential of the species between 0 K (μ°) and the reaction conditions ($\mu\ (P,T)$), and is calculated using the ideal gas equation; P° is the pressure at standard state (1 atm).

$$\mu\ (P,T) =\ \mu^{\circ} + RT \ln\left(\frac{P}{P^{\circ}}\right) \quad (2.24)$$

Translational, rotational, and vibrational contributions to the entropy and enthalpy

of the gaseous species were calculated according to standard statistical mechanics approximations.[163]

Previous studies have reported that sole use of the harmonic oscillator approximation underestimates adsorption free energies on zeolites, since they retain a significant component of their translational and rotational free energy.[164–169] We estimated the entropy difference between a clean and adsorbate-covered site, ΔS^{ST} from an empirical approximation validated by potential of mean force AIMD simulations, using the Sackur-Tetrode equation and assuming that the adsorbate retains 2/3 of its gas-phase translational entropy:[170,171]

$$\Delta S^{\mathrm{ST}}_{x,y} = \left(S_{\mathrm{Z_*PdH_xO_y}} - S_{\mathrm{Z_*Pd}}\right) \approx \frac{2}{3}\, k_B \ln\left[\left(\frac{2\pi M_{x,y} k_B T}{h^2}\right)^{\frac{3}{2}} \left(\frac{k_B T}{P^\circ}\right) \frac{e^{\frac{5}{2}}}{N_A}\right] \quad (2.25)$$

where $\mathrm{M}_{x,y}$ represents mass of the adsorbate.

Analogous to the expressions above, when NO is present in addition to O and H atoms, the equations can be modified to incorporate the chemical potential of NO.

$$\begin{aligned}\Delta G^{\mathrm{form}}_{x,y,z}\ (T,\ \Delta\mu_{\mathrm{O_2}},\ \Delta\mu_{\mathrm{H_2O}},\ \Delta\mu_{\mathrm{NO}}) &= \Delta E^{\mathrm{form}}_{x,y,z} - T\ \Delta S^{\mathrm{ST}}_{x,y,z}\,(T) \\ &- \frac{x}{2}\left(\Delta\mu_{\mathrm{H_2O}} - \frac{1}{2}\,\Delta\mu_{\mathrm{O_2}}\right) - \frac{y}{2}\,\Delta\mu_{\mathrm{O_2}} - z\Delta\mu_{\mathrm{NO}} \quad (2.26)\end{aligned}$$

2.4.3 Details of H_2O-solvated Pd, and Zeolite Cluster Calculations

Starting with the PBE-optimized periodic geometries of [$\mathrm{ZPd^{I}}$], [$\mathrm{ZPd^{II}OH}$], and [$\mathrm{Z_2Pd^{II}}$], we created the zeolite clusters by isolating the Pd cation in the associated 6 (or 8) MR, along with four of the neighboring 4MRs and 8 (or 6) MR, and Si T-

sites bound to the terminal oxygen atoms. We replaced these terminal T-sites with a hydrogen atom while maintaining the O-H bond length of 0.97 Å and orientation of original bond angles of the periodic zeolite framework intact. We calculated single-point energies of the species considered in both the models using Gaussian 16[172] and DFT methods of GGA-PBE, and hybrid functionals of HSE06 and B3LYP.[173,174] Single-point energy calculations using the CCSD(T) method were performed only for the species considered in the H_2O-solvated Pd model. All calculations were carried out spin unrestricted with the basis set def2-TZVPP.[175,176]

For solvated structures, harmonic vibrational frequencies were calculated by first optimizing the geometries using B3LYP and the def2-TZVPP basis set. In the case of non-solvated structures, only the Pd atom and the bound nitrosyl ligand were allowed to relax before performing frequency calculations.

NBO analyses were performed on B3LYP-optimized geometries employing NBO 3.1[177] as implemented in Gaussian 16. The visualization of the analyses was done in GaussView 6.[178]

2.4.4 Zeolite Synthesis and Characterization

We synthesized Pd/SSZ-13, Pd/ZSM-5, Pd/BEA catalysts via incipient wetness impregnation using the SSZ-13 zeolites purchased from ACS materials: Type HC (Si/Al = 15, H^+ form) and Type B (Si/Al = 10, NH_4^+ form), ZSM-5 and BEA zeolites purchased from Zeolyst Inc: CP814E*(Si/Al = 12.5, NH_4^+ form) and CBV 3024E (Si/Al = 15, NH_4^+ form). We followed a three-step calcination process (80°C for 2 hours, 105°C for 10 hours and 600°C for 4 hours with a 1°C/min ramp rate in between) to transform the zeolites into the proton form and dehydrate the zeolites before intro-

ducing Pd. We used palladium (II) nitrate dihydrate as the precursor and dissolved the Pd into 28% ammonia hydroxide solution, both of which were purchased from Sigma Aldrich. The mass of Pd and parent zeolites were measured to achieve 1 wt.% or 0.5 wt.% Pd weight loading. The volume of Pd containing solution was the same as the pore volume of the zeolite. Immediately following the calcination to gain the proton form, the Pd precursor solution was added drop-wise with rigorous stirring and mixing to form a slurry. We then repeated the same calcination process on the slurry after Pd was introduced. Si/Al ratios and Pd/Al ratios of the resulting samples were confirmed by inductively coupled plasma optical emission spectroscopy (ICP-OES) analysis at Galbraith Laboratories, Knoxville TN. We also used X-ray diffraction (XRD) to confirm the zeolite morphology and crystallinity of the Pd/SSZ-13 (Si/Al = 8.9, Pd/Al = 0.056). XRD patterns were collected using a PANalytical X'Pert Pro multi-purpose diffractometer with Cu K X-ray source and a vertical circle theta:theta goniometer at an incident radius of 240 mm. We performed H_2 temperature programmed reduction (H_2-TPR) on a Micromeritics AutoChem 2920 system with 5% H_2 (Ultra-high purity, Paxair) and a temperature range from 313 K to 873 K to identify Pd speciation and confirm Pd ion-exchange level in Pd/SSZ-13 (Si/Al = 8.9, Pd/Al = 0.056). We first pretreated the sample at 873 K in 10% O_2 and cooled down to 313 K in 10% O_2 before turning off O_2 and flowing H_2. The sample was purged by H_2 for 1 hour before the temperature ramp. A repetition of the exact same procedure including O_2 pretreatment was also performed right after the first H_2-TPR experiment. XRD and H_2-TPR results are reported in supporting information 4.1.2.

2.4.5 Details of Spectroscopic Methods (DRIFTS, XAS, EXAFS)

We collected DRIFTS spectra at 4 cm^{-1} resolution on a Thermo Scientific Nicolet iS50 FTIR spectrometer with a Harrick Praying Mantis DRIFTS cell and accessories installed. We averaged 64 spectra for background collection and 32 spectra for each sample spectrum, of which the acquisition time is 48 seconds and 24 seconds, respectively. We used Praxair research purity gas cylinders as the source of NO, CO, O_2 and He, and applied moisture and O_2 traps purchased from Matheson on the He carrier gas line. We used a homemade bubbler and deionized H_2O to introduce H_2O vapor into the manifold, and confirmed the H_2O concentration using an MKS MG2030 IR analyzer. We measured the temperatures of the cell and the bubbler using K-type thermocouples. When conducting ex-situ characterization, a cold trap was also applied to further eliminate any trace amount of H_2O and we collected spectra with KBr in the cell under the exact same conditions for background subtraction. We also performed in-situ NO adsorption, NO+CO co-adsorption, and CO addition experiments in the presence and absence of H_2O. A moisture trap and a cold trap were used to collect NO adsorption spectra in the absence of H_2O, and we collected background from a sample at 473 K in 10% O_2 that had been pretreated at 873 K in 10% O_2 to be consistent with the NO adsorption experiments. We also collected background spectra from 873 K O_2 pretreated and H_2O hydrated samples to be consistent with NO adsorption and CO addition experiments in the presence of H_2O.

We collected Pd K edge (23450 eV) X-ray absorption spectra for Pd/SSZ-13 (Si/Al = 8.9, Pd/Al = 0.056) at beam 8-ID of the National Synchrotron Light Source II, Upton NY. All measurements were performed with an electron storage ring operated

at 3 GeV and a beam current of 400 mA. We pelletized the catalysts to 225–425 μm and loaded them into 0.25-inch stainless steel tube placed inside an aluminum heating jacket. We collected spectra of the ambient exposed sample with no additional treatment. More details of the in-situ reactor cell can be found elsewhere.[179] Pd K edge in-situ XAS dehydration experiments were performed at beam 10-ID of the Advanced Photon Source, Lemont IL. Measurements were taken in transmission mode with a stainless-steel sample holder, a quartz tube reactor and X-ray transparent windows.

2.4.6 NO Temperature Programmed Desorption and Steady-State CO Oxidation

We conducted the NO temperature programmed desorption and CO oxidation experiments in a 0.25-inch quartz tube reactor placed in a horizontal tubular Thermo Fisher furnace. 40 mg of catalyst were pelletized into 225-425 μm particles and loaded into the quartz tube reactor, kept in place by quartz wool on both sides of the bed. All gas components except H_2O and N_2 were metered from Praxair-supplied ultra-high purity gas cylinders. N_2, the carrier gas in all cases, was purified from compressed air by a Parker N_2 generator. Deionized H_2O was injected using a Bronkhorst controlled evaporator mixer (CEM). We kept the total flow rate at 546 standard cubic centimeters per minute, to achieve a monolith equivalent gas hour space velocity of 30,000 hr^{-1}. We measured and recorded catalyst bed temperature and outlet gas compositions using a K-type thermocouple at the outlet of the catalyst bed and an MKS MG2030 IR analyzer, respectively. Between each NOx-TPD and CO oxidation experiment, we changed and pretreated samples at 873 K in 10% O_2 balanced by N_2 for 45 min. Inlet concentrations were 200 ppm NO, 10% O_2 and 0 or 4.5% H_2O for

the NOx-TPD experiments, and 0 or 200 ppm NO, 200 ppm CO, 10% O_2 and 0 or 4.5% H_2O for the CO oxidation experiments. The temperature ramp was performed from 350 K to 900 K at a ramp rate of 30 K/min. We performed the same 873 K in 10% O_2 pretreatment followed by N_2 purge at 873 K and cooling in N_2 before measuring the steady state water gas shift activity with the inlet concentrations as 200 ppm CO and 4.5% H_2O.

Acknowledgements

The authors acknowledge financial support by the Department of Energy Office of Energy Efficiency & Renewable Energy (DE-EE0008233) (W.S.E., L.C.G.). Collaboration with Oak Ridge National Laboratory was funded by the U.S. Department of Energy Vehicle Technologies Office (W.S.E., Y.G.), and the UVA Engineering Research and Innovation Award (C.P., K.M.). S.L. acknowledges financial support by a PLSPostdoctoral Grant of the Lawrence Livermore National Laboratory during the preparation of this manuscript. This manuscript has been authored in part by UT-Battelle (J.A.P.), LLC under Contract No. DE-AC05-00OR22725 with the U.S. Department of Energy. The United States Government retains and the publisher, by accepting the article for publication, acknowledges that the United States Government retains a nonexclusive, paid-up, irrevocable, worldwide license to publish or reproduce the published form of this manuscript, or allow others to do so, for United States Government purposes. The Department of Energy will provide public access to these results of federally sponsored research in accordance with the DOE Public Access Plan (http://energy.gov/downloads/doe-public-access-plan). This

research used beamline 8-ID (ISS) of the National Synchrotron Light Source II, a U.S. Department of Energy (DOE) Office of Science User Facility operated for the DOE Office of Science by Brookhaven National Laboratory under Contract No. DE-SC0012704. This research used resources of the Advanced Photon Source, a U.S. Department of Energy (DOE) Office of Science User Facility operated for the DOE Office of Science by Argonne National Laboratory under Contract No. DE-AC02-06CH11357. MRCAT operations are supported by the Department of Energy and the MRCAT member institutions. The authors thank Prof. Jeffrey T. Miller, Matthew A. Conrad, Nicole J. Libretto, and Christopher K. Russell for their assistance with the XAS experiments. The authors acknowledge Research Computing at the University of Virginia for providing computational resources and technical support that have contributed to the results reported within this publication.

Chapter 3

Kinetic and Thermodynamic Factors Influencing Palladium Nano-particle Redispersion into Mononuclear Pd(II) Cations in Zeolite Supports

This chapter has been reproduced in its entirety with permission from Lardinois, T. M.; Mandal, K.; Yadav, V.; Wijerathne, A.; Bolton, B. K.; Lippie, H.; Li, C. W.; Paolucci, C., and Gounder, R. *J. Phys. Chem. C* **2022**, 126, 19, 8337–8353. The supplementary materials for this paper/ chapter are available on https://doi.org/10.1021/acs.jpcc.2c01613. This chapter builds up on our knowledge about the Pd cation speciation in SSZ-13 zeolites to further explore the structural interconversion between Pd nanoparticles and cations in zeolites, that plays a prominent role in the thermal deactivation of these materials, and plausible routes of catalyst regeneration. My key contributions to this study have been performing DFT calculations for computing the energies of bulk Pd, PdO, Pd^{2+} cations using DFT, and developing a theoretical model for estimating the ther-

modynamic extent of Pd particle redipsersion to cations as a function of particle size and reaction conditions. As a co-first author on the paper, I was also responsible for writing the introduction and computational results, formatting the manuscript, and addressing reviewer comments.

3.1 Introduction

The dynamic processes responsible for the sintering of metal nanoparticles and their redispersion into smaller clusters and isolated atoms and ions on oxide supports strongly influence the reactivity, selectivity, deactivation, and regeneration of heterogeneous catalysts and adsorbent materials.[2,180–184] The redispersion of nanoparticles and clusters to single atoms results in catalyst deactivation for methane oxidation on Pd supported on Al_2O_3[185] and Pt supported on CeO_2,[186] NO reduction in the presence of CO on Pt supported on aluminosilicate MWW zeolites,[8,187] CO oxidation on various metals (Ru,[188] Rh,[188] Ir,[188] Pt,[189] and Pd[190]) supported on CeO_2, and propane dehydrogenation on Pt-Sn clusters supported on CeO_2.[191] Conversely, the formation of metal nanoparticles from single atoms causes deactivation of Pt,[186,192] Pd,[188,192] Cu,[193] and Rh[192] on CeO_2 for CO oxidation, Au on $CeZrO_4$[194] and CeO_2[195] for the water-gas shift reaction, Au on carbon for acetylene hydrochlorination,[196,197] and Rh on aluminosilicate zeolites or TiO_2 for methane oxidation to methanol.[198] Compared to catalysts containing larger nanoparticles, catalysts composed of single atoms and sub-nanometer sized clusters are typically more susceptible to structural changes in response to their reaction environment, and thus tend to sinter more readily via Ostwald ripening (OR) under reducing conditions at high temperatures.[2,199] Redispersion of nanoparticles to single atoms and ions can facilitate catalyst regener-

ation;[200,201] however, the atomistic details of the thermodynamic driving forces and kinetic mechanisms governing such redispersion processes are not well-understood.

The structural interconversion between oxide-supported Pd nanoparticles and cations is strongly affected by reaction conditions and nanoparticle sizes,[8,14,185,202–208] and is of particular relevance for several catalytic and adsorption applications including CO oxidation,[188,190,209–211] Wacker oxidation,[75,212,213] methane oxidation,[15,214–217] alkene hydrogena-tion,[70,218–220] and low-temperature (<473 K) NO trapping in diesel engine emissions.[11,77,109,221,222] While the dominant active sites for methane oxidation are located on Pd nanoparticles,[185,223] isolated Pd atoms and cations are the active sites for Wacker[75,212,213] and CO oxidation,[224] hydrodechlorination,[225] and NO trapping in passive NOx adsorber materials.[226,227] The redispersion of Pd nanoparticles to cations is facilitated by reactants such as NO (during NOx reduction on TiO_2-supported three-way catalysts,[228] H_2-selective catalytic reduction of NO on ZrO_2 supports,[229] sequential adsorption of CO and NO on ceria-zirconia supports,[230] and solid-state ion-exchange in CHA zeolites[231]) and water (in FAU zeolites during Wacker oxidation[75,212,213]), and via hydrothermal treatments with steam and air in aluminosilicate MFI, MWW and CHA zeolites.[12,16,85] Redispersion can be further promoted when synthesis protocols are used that promote the formation of defect or cation-exchange sites in the support that are able to capture mobile metal species emitted from nanoparticles in atom trapping processes.[200,201] Metal-support interactions also play a crucial role to stabilize dispersed isolated atoms, with CeO_2 and Fe_2O_3 supports exhibiting strong binding to Pt,[189,191,192,232,233] Rh,[192] Ru,[234] and Cu.[184,193] Despite the low vapor pressure of Pd,[15] atom trapping mechanisms have been shown to stabilize isolated Pd on CeO_2,[188,192,225,235] TiO_2,[236] γ-Al_2O_3,[185,224] and aluminosilicate zeolites. Yet, numerous questions regarding the kinetic and thermodynamic factors that influence

conversion of Pd nanoparticles to single atoms and cations, and their dependence on reaction conditions, initial Pd particle size, and the metal-support interaction remain unanswered.

In this work, we examine the thermodynamic and kinetic factors and reaction mechanisms that govern the interconversion of Pd nanoparticles and cations, studying Pd supported on aluminosilicate zeolites, given that these concepts are particularly relevant for Pd-exchanged zeolites being explored in practical applications as materials for passive NOx adsorption (PNA)[77,226,227] in automotive exhaust, Wacker[75,212,213] and methane oxidation.[15,74,235,237] Zeolite supports are also a versatile materials platform for performing fundamental experimental studies because of the structural uniformity of their crystalline frameworks and the ability to synthesize them with precise modifications in bulk and atomic composition, which enable more faithful comparisons to the structures modeled by theoretical studies. Pd-zeolites typically contain various Pd structures[85,238] of different nuclearity (mono- and polynuclear)[226,239,240] and valence (zero- to tetravalent),[66,241–244] but only extraframework, mononuclear cation sites charge-compensated by framework Al atoms (ion-exchanged Pd) are the purported binding sites for NOx adsorption in the context of PNA applications[64] and the active sites for Wacker oxidation.[75,212,213] The structural lability of Pd allows interconversion between agglomerated domains and mononuclear ion-exchanged sites,[245] which depends on the size of Pd nanoparticle domain sizes and their density on the support,[185] and causes undesirable agglomeration and deactivation under PNA and Wacker-relevant conditions.[13,16,82,227] Yet, such structural lability allows for the redispersion of agglomerated domains to ion-exchanged sites under high-temperature (>500 K) air[17] or NO[76,231] regeneration. Together, these challenges and observations motivate improved fundamental understanding of the critical thermodynamic and

kinetic factors that govern Pd structural interconversion in zeolites, to guide the design of these materials and regeneration protocols based on solid-state ion-exchange routes.

Here, we combine experiment and theory to understand the influence of initial Pd nanoparticle size and external gas conditions on the thermodynamic and kinetic factors influencing structural conversion between Pd nanoparticles and ion-exchanged Pd^{2+} in CHA zeolites. Pd-CHA zeolites are prepared to initially contain normally-distributed or log-normally distributed Pd particles of different mean size, located at extracrystalline zeolite surfaces. These materials are then treated to high temperatures (598–973 K) in flowing air with and without H_2O, and the number of agglomerated PdO domains and ion-exchanged Pd^{2+} sites are quantified with H_2 temperature-programmed reduction (TPR). Density functional theory (DFT) computed thermodynamic phase diagrams are constructed for a range of Pd particle sizes under various gas environments (P_{O_2}, P_{H_2O}, temperature) to quantitatively compare with experimentally measured ion-exchanged Pd^{2+} contents on samples exposed to similar treatments to show that H_2O can promote the formation of PdO agglomerates from Pd^{2+} cations. Apparent rates of conversion of metallic Pd domains to ion-exchanged Pd^{2+} sites under flowing air are measured as a function of temperature (598–673 K) and H_2O pressure (0–2 kPa) to deduce mechanistic information and determine kinetic implications of H_2O and O_2 pressures and the Pd particle size on the redispersion to ion-exchanged Pd^{2+} sites. Kinetic Monte Carlo (kMC) simulations are performed to rationalize the observed kinetics, and show that Pd redispersion at temperatures <900 K does not occur through a gas-phase process, but rather through a surface-mediated OR mechanism whereby mobile monomers diffuse on the zeolite support and bind at ion-trapping sites.

3.2 Methods

3.2.1 Pd-Zeolite Characterization

The amounts of agglomerated PdO and mononuclear Pd^{2+} cations were quantified with H_2 TPR procedures described elsewhere[17] using a Micromeritics AutoChem II 2920 Chemisorption Analyzer equipped with a thermal conductivity detector (TCD) to quantify H_2 consumption. In brief, the TCD response factor was generated using varied partial pressures (0.5–5.0 kPa) of H_2 in balance Ar, which quantified the amount of Ag on a Ag_2O reference material (Micromeritics) to within a factor of 1.12. After a given treatment sequence, samples (0.3–0.6 g) were exposed to flowing Ar (0.50 cm^3 s^{-1}, UHP, 99.999%, Indiana Oxygen) with 1–2 kPa H_2O for >0.5 h to hydrate mononuclear Pd^{2+} cations at 303 K. Samples were then cooled to 203 K (0.167 K s^{-1}) in flowing Ar (0.167 cm^3 s^{-1}) using a Micromeritics Cryocooler II accessory. An isopropanol slurry (cooled to 184 K with liquid N_2) was inserted between the TCD detector and the sample to trap any condensable gases. The Ar stream was replaced with 5 kPa H_2 in balance Ar (0.167 cm^3 s^{-1}, certified mixture, Indiana Oxygen), and once a stable TCD signal was achieved, the sample was treated to 573 K (0.167 K s^{-1}) and held for 0.5 h. All H_2 TPR profiles and discussion of data fitting procedures are reported in Section S4, SI.

Volumetric O_2 chemisorption experiments were performed with a Micromeritics ASAP 2020 Plus Chemisorption unit. Samples (~0.2 g) were treated in flowing H_2 (UHP, 99.999%, Praxair) to 673 K or 873 K in O_2 (UHP, 99.98%, Matheson) before preparing for chemisorption. Samples were first flushed in flowing He then degassed under vacuum (< 3 mHg) for 1 h at 373 K. Next, a leak test was performed to confirm that leak rates were below the threshold of < 600 mHg h^{-1} (recommended

by Micromeritics). Samples were then treated in H_2 to 573 K (0.167 K s^{-1}) for 1 h, evacuated at 573 K for 1 h, then another leak test was performed at 313 K. Then, the sample was evacuated for 0.3 h at 313 K before collecting two O_2 adsorption isotherms (313 K, 2−42 kPa), with an evacuation step after the first isotherm to remove non-chemisorbed O_2. Isothermal uptakes were linearly extrapolated to zero pressure, and the difference in uptakes at zero partial pressure yielded the amount of chemisorbed O_2. The dispersion was calculated assuming one O atom titrates one surface Pd atom.

3.2.2 Isothermal Pd Redispersion Kinetics.

The as-exchanged $[Pd(NH_3)_4]^{2+}$-CHA (2.2 wt% Pd) material was first pelleted then sieved to retain 180–250 μm diameter aggregates. Treatment sequences and H_2 TPR analysis were performed with a Micromeritics Autochem II 2920 Chemisorption Analyzer. Samples (0.03–0.05 g) were first pretreated in flowing H_2 in Ar (0.5 cm^3 s^{-1}; 5 kPa H_2, certified mixture, Indiana Oxygen) to 673 K for 1 h, and cooled to ambient temperature. Samples were then cycled through H_2 treatments, inert purge treatments, air treatments (i.e., isothermal redispersion treatments), and then the amounts of PdO and Pd^{2+} cations were quantified by H_2 TPR. As an example procedure for an isothermal redispersion measurement at 648 K in air without added H_2O, the sample was treated in flowing (0.5 cm^3 s^{-1}) 5 kPa H_2 in Ar to 648 K (0.167 K s^{-1}) for 0.5 h, then the 5 kPa H_2 in Ar stream was replaced with flowing Ar (0.5 cm^3 s^{-1}; UHP, 99.999%, Indiana Oxygen) to purge the system for 0.083 h. Then, the Ar stream was replaced with flowing air (0.5 cm^3 s^{-1}; Air Zero, Indiana Oxygen) for a specified amount of time (0.003–1 h), and then rapidly cooled (0.67 K s^{-1}) from 648 K to ambient temperature in flowing Ar (0.5 cm^3 s^{-1}) Ar using a Micromeritics Cry-

ocooler II accessory. In cycling experiments, the air exposure times were randomly varied between 0.003–1 h to avoid any systematic errors that may have been caused by this step in the procedure.

3.2.3 Details of DFT, and Ab Initio Formation Free Energies Calculations.

We used the Vienna ab initio simulation package (VASP, version 5.4.4)[146] to perform plane-wave, periodic DFT calculations with an energy cutoff of 400 eV and projected augmented wave (PAW)[154] pseudopotentials for core-valence interactions. We used the bulk structures reported in the Materials Project[246] database for metallic Pd and PdO, and the 24 T-site 1Al and 2Al Pd-exchanged SSZ13 species in the study by Mandal et al.[247] as initial guesses, and optimized them with the Perdew-Becke-Ernzerhof (PBE)[147] functional and subsequently, the Heyd-Scuseria-Erzenhof (HSE06)[146–153] hybrid exchange-correlation functional. Dispersion corrections were calculated using the Becke-Johnson damping (D3(BJ)-vdw) method.[148,149] We used the HSE06 functional with D3(BJ) dispersion corrections because it correctly captures the formation energy of PdO within 2 kJ mol^{-1} of the experimental value (Table S5.2, SI). We used a convergence threshold of 10^{-8} eV and 0.01 eV/Å for the electronic energies and atomic forces, respectively. We used the Monkhorst-Pack k-point mesh detailed in the Materials Project database to sample the first Brillouin zone for bulk metallic Pd and PdO; only the Γ point was used for zeolitic structures. The optimized geometries of 6-MR 3NN Z_2H_2 and Z_2Pd have been provided in the CONTCARS attachment of the SI. Additional details about the formation energy calculations can be found in Section S5, SI.

3.2.4 Details of Particle Size Dependent Models.

To estimate surface energies, we used the Python Materials Genomics (*Pymatgen*) package and its built-in *Slabgenerator* function[248–250] to construct symmetric slabs of up to Miller index 2 for metallic Pd and PdO from their respective optimized bulk structures. The slab thickness was set to 10 Å, and a 15 Å vacuum space was applied to eliminate interactions between the periodic images of the surfaces in the z direction. The k-point mesh for the slabs in the x and y directions was appropriately scaled by using the k-points per reciprocal Å for the bulk structures, with a single k-point applied in the z direction. We optimized and computed the energies of the unconstrained slabs using the PBE-D3(BJ)-vdw functional due to computational expense, and the same convergence criteria as that for the bulk structures. The surface energies (γ_{slab}) of the slabs were calculated as:[251]

$$\gamma_{\text{slab}}(P_{\text{O}_2},\ T) = \frac{E_{\text{slab}} - n_{\text{Pd}}E_{\text{bulk}} - n_{\text{O}}\mu_{\text{O}}(P_{\text{O}_2},\ T)}{2A} \tag{3.1}$$

where n_{Pd} and n_{O} represent the number of Pd atoms and excess or deficit O atoms in the slab, respectively, μ_{O} is the chemical potential of O, A denotes the surface area of one side of the slab, E_{slab} and E_{bulk} are the total energy of the slab and the energy of the bulk per formula unit, respectively. The equilibrium shapes of metallic Pd and PdO nanoparticles were determined from their respective Wulff constructions which represent the minimum surface energy for a given crystal. We used the *Wulffshape* function in *Pymatgen* to generate the Wulff constructions for a range of μ_O values,[252] and evaluated the average surface energy (γ).

Based on data fitted to calorimetric measurements of the chemical potentials of transition metals on oxide supports, Campbell et al.[253–255] expressed the free energy

of supported hemispherical nanoparticles of an effective diameter d relative to bulk (ΔG) as follows:

$$\Delta G\left(d, P_{O_2},\ T\right) = \left(3\gamma\left(P_{O_2},\ T\right) - E_{\text{adh}}\right)\left(1 + \frac{1.5}{d}\right)\left(\frac{2\rho}{d}\right) \tag{3.2}$$

where ρ represents the volume normalized per mole of metal. The adhesion energy between the nanoparticle and the support E_{adh} is expressed according to the Young equation:

$$E_{\text{adh}} = \gamma(1 + \cos\,\theta) \tag{3.3}$$

where θ is the contact angle between the particle and support. While $\theta = 66 - 90°$ has been reported for Pd on SiO_2,[256,257] it is unknown for PdO on SiO_2; therefore, we considered multiple values of $\theta = 60°, 90°$, and $120°$ which are representative of varying degrees of adhesion (Figures S5.9-10, SI).

Subsequently, we evaluated the formation free energy of PdO nanoparticles ($\Delta G^{\text{form}}_{\text{PdO}}$) by incorporating the size-dependent free energy of PdO nanoparticles (ΔG_{PdO}) with respect to bulk Pd (Eq. 3.2) as:

$$\Delta G^{\text{form}}_{\text{PdO}}\left(d_{\text{PdO}}, P_{O_2}, T\right) = \Delta G^{\text{form}}_{\text{PdO}_{\text{bulk}}}\left(P_{O_2}, T\right) + \Delta G_{\text{PdO}}\left(d_{\text{PdO}}, P_{O_2},\ T\right) - \Delta G_{\text{Pd}}\left(d_{\text{Pd}}\right) \tag{3.4}$$

To relate the increment in volume associated with the formation of PdO from Pd, we used the ratio of the particle diameters of PdO and Pd ($d_{\text{PdO}}/d_{\text{Pd}} = 1.19$) from the reported densities of bulk Pd ($\rho_{\text{Pd}} = 11.41$ g cm^{-3}) and PdO ($\rho_{\text{PdO}} = 7.79$ g cm^{-3}).[246]

3.3 Results

3.3.1 Effects of Initial Pd Particle Size and Treatment Conditions on the Conversion of Agglomerated Pd Particles to Exchanged Pd^{2+} ions

3.3.1.1 Synthesis of Monodisperse Pd Nanoparticles Supported on CHA Zeolites

To isolate the effects of Pd particle size on their structural interconversion to mononuclear Pd^{2+} cations that are charge-compensated by framework Al in zeolite supports (denoted "ion-exchanged Pd^{2+}") during high-temperature air treatments, Pd particles of monodisperse size distributions were synthesized using solution-phase colloidal synthesis methods[185] and then deposited onto the exterior of CHA zeolite crystallites (details of Pd deposition procedures in Section S1, SI). Three different colloidal Pd nanoparticle solutions were characterized with TEM to contain monodisperse particles that were nominally 2, 7, and 14 nm in diameter (Figures S2.3–S2.6, SI). These colloidal solutions were diluted in a hexane solvent and mixed with the H-form CHA zeolite powder, and then sonicated to deposit the oleylamine-capped Pd particles (denoted "as-deposited Pd-CHA"). Samples are referred to as Pd-CHA-X-ND, where X is the average particle diameter (in nm) on as-deposited samples and where the suffix ND denotes that a normal distribution of particle sizes are present initially, as determined by TEM.

Figure 3.1 shows *ex situ* TEM images of the as-deposited Pd-CHA-X-ND samples, and **Table 3.1** lists their particle size distributions and elemental analysis. Pd particle size distributions were similar on as-deposited Pd-CHA-X-ND samples as in the

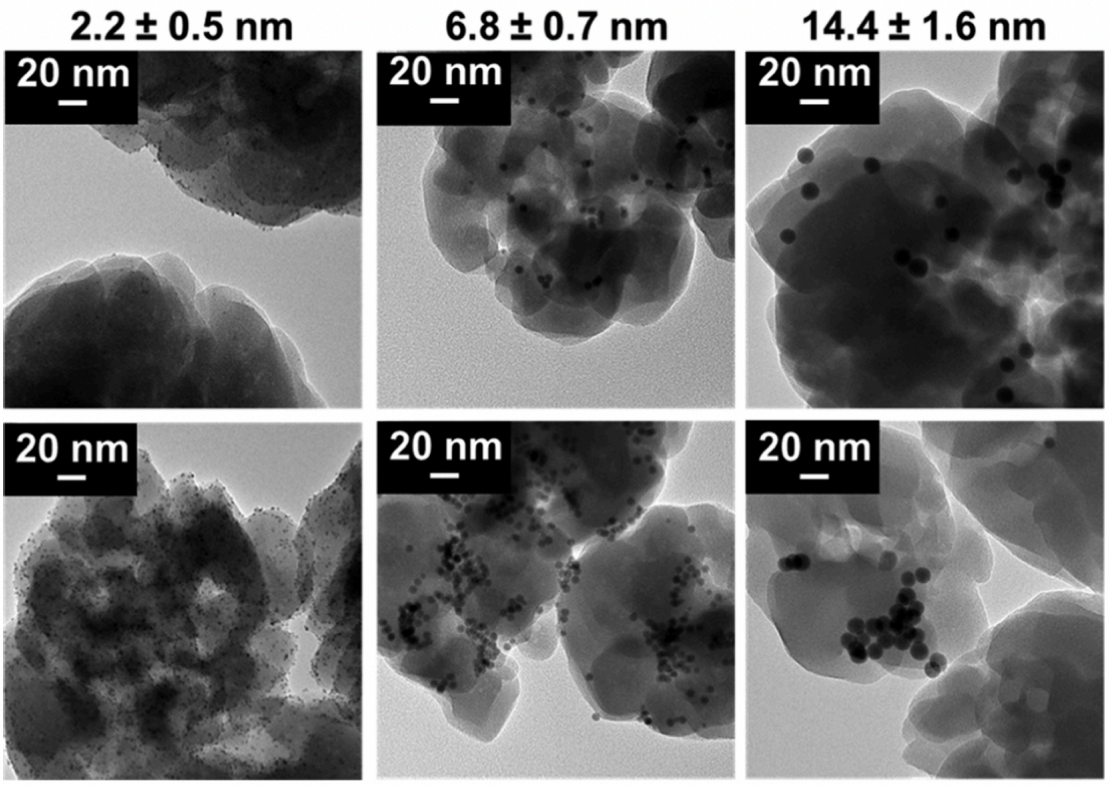

Figure 3.1: *Ex situ* TEM images of the as-deposited Pd-CHA-X-ND materials: Pd-CHA-2-ND (left), Pd-CHA-7-ND (middle), Pd-CHA-14-ND (right).

Table 3.1: Characterization Data on As-deposited Pd-CHA-X-ND Samples[a]

sample[b]	nominal Pd particle size / nm	TEM characterized particle size / nm[c]	Pd wt%[d]	Pd/Al[d]
Pd-CHA-2-ND	2	2.2 ± 0.5	1.12	0.082
Pd-CHA-7-ND	7	6.8 ± 0.7	0.72	0.053
Pd-CHA-14-ND	14	14.4 ± 1.6	0.84	0.061

[a]Particle size distributions are reported in Figure S2.7−2.9,Supporting Information. [b] Samples are denoted as Pd-CHA-X-ND, where X denotes the nominal Pd particle size and ND denotes a normal particle size distribution. [c] The average particle size plus or minus one standard deviation. [d] The Pd wt % and Pd/Al molar ratio were determined by inductively coupled plasma (ICP) spectroscopy.

colloidal precursor solutions, demonstrating the deposition procedure used did not alter the monodisperse distributions of oleylamine-capped Pd nanoparticles; however, this deposition procedure did result in some non-uniformities in how Pd particles were spatially distributed at external crystallite surfaces, with some localized Pd nanoparticle aggregation observed for the Pd-CHA-7-ND and Pd-CHA-14-ND samples. To remove organic species without altering the Pd particle size distribution, as-deposited Pd-CHA-X-ND samples were first treated in air to 548 K for 4 h, before studying the effects of higher temperature air treatments. Samples treated with this protocol were analyzed in a subsequent TGA experiment and did not show desorption events for organic species (460–600 K), and TGA profiles were similar to that of the parent H-CHA support (Figures S3.1 and S3.2, SI), indicating that the majority of organic content at exterior Pd surfaces was successfully removed. TEM images of Pd-CHA-X-ND samples treated to 548 K in air showed similar Pd particle size distributions as present in their as-deposited form (Figures S2.10–S2.13, SI). Therefore, we conclude that treatment of as-deposited Pd-CHA-X-ND samples in air to 548 K successfully removed the majority of organic species while retaining the Pd particle size distribution and zeolite support intact, enabling subsequent studies of the conversion of such particles to Pd^{2+} cations upon treatment to higher temperatures (>548 K).

3.3.1.2 Effects of Pd Particle Size on Pd Oxidation and Structural Interconversion

The as-deposited Pd-CHA-X-ND samples were treated to high temperatures (598–873 K) in flowing air to determine the effects of Pd particle size on the extent of oxidation with O_2 and conversion to Pd^{2+} cations. The amounts of agglomerated PdO domains and Pd^{2+} cations after high-temperature air treatments were charac-

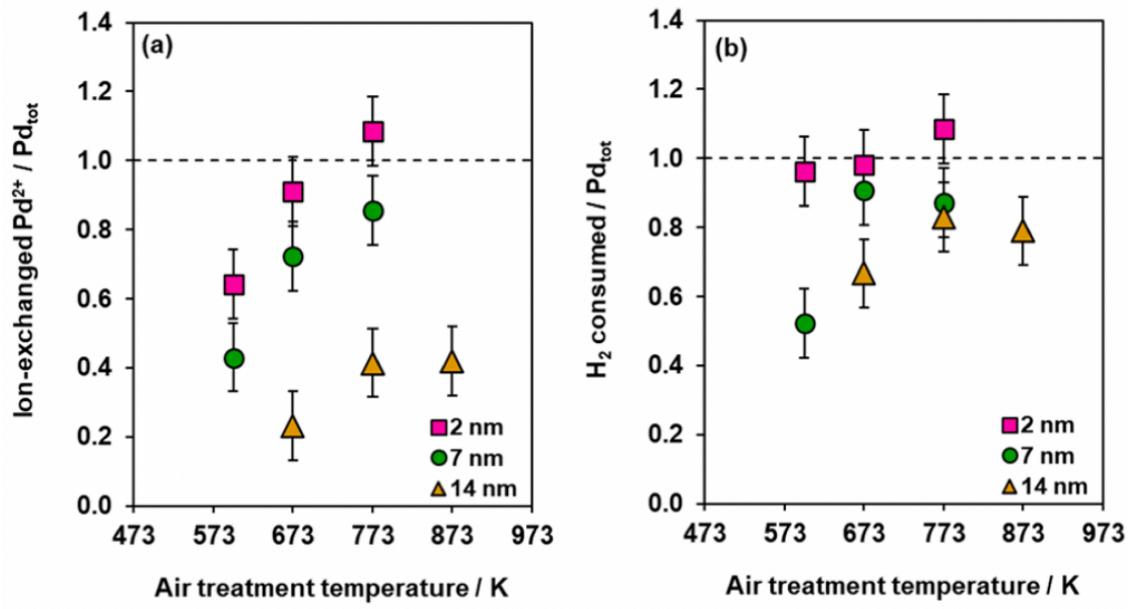

Figure 3.2: (a) The amount of ion-exchanged Pd^{2+} (per total Pd) after treatment in flowing air (593 873 K) for Pd-CHA-2-ND (squares), Pd-CHA-7-ND (circles), and Pd-CHA-14-ND (triangles). (b) Total H_2 consumed (per total Pd) from (a). Dashed lines represent theoretical maximum amounts. H_2 TPR profiles reported in Figures S4.1 S4.3, SI.

terized with H_2 TPR (profiles reported in Figures S4.1–S4.3, SI). Previous reports concluded that agglomerated PdO domains have a lower barrier for reduction by H_2 than hydrated Pd^{2+} ion sites; thus, H_2 consumption features can be quantified and assigned to agglomerated PdO and ion-exchanged Pd^{2+} (further discussed in Section S4, SI).[17,245,258,259]

The total H_2 consumption (per total Pd) and the amount of ion-exchanged Pd^{2+} (per total Pd) after treatment in flowing air Pd-CHA-X-ND samples are reported in **Figure 3.2**. At a given air treatment temperature, the amount of ion-exchanged Pd^{2+} formed on CHA increased as the initial Pd nanoparticle size decreased, consistent with previous reports that smaller Pd nanoparticles (at fixed Pd density) were converted to greater amounts of mononuclear $Pd(OH)_2$ on γ-Al_2O_3.[185] For Pd-CHA-

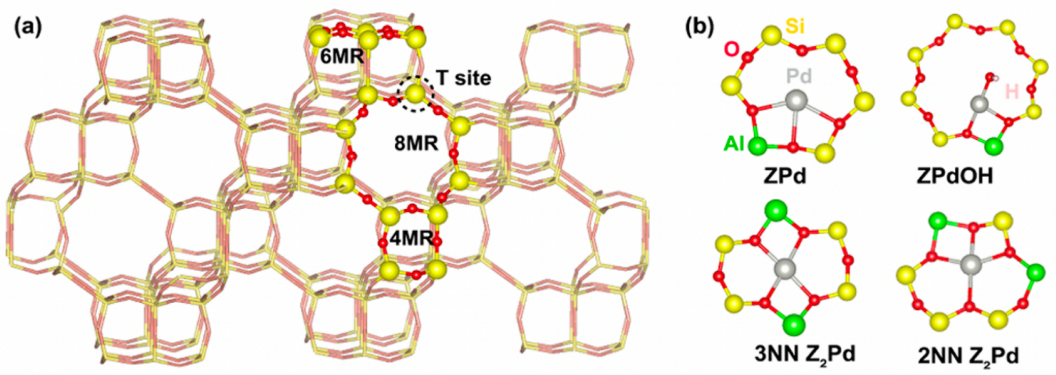

Figure 3.3: (a) Framework of chabazite (CHA) made up of four-, six-, and eight-membered rings (MR). (b) Pd cations exchanged at 1Al and 2Al sites.

2-ND, the total H_2 consumed per Pd was near unity at all air treatment temperatures studied; thus, all of the 2 nm Pd nanoparticles were oxidized to Pd^{2+} during the air treatment. In contrast, Pd-CHA-7-ND and Pd-CHA-14-ND showed sub-unity H_2 consumption per Pd for low-temperature air treatments (598–673 K), suggesting that a fraction of the 7 nm or 14 nm Pd nanoparticles were not fully oxidized during the air treatment, consistent with a report by Chin et al. showing that higher O_2 pressures were needed to fully oxidize larger metallic Pd particles supported on γ-Al_2O_3 at a fixed temperature of 973 K.[260]

3.3.1.3 Thermodynamics of Conversion of Agglomerated Pd Particles to Exchanged Pd^{2+} Ions

Estimating the maximum fraction of Pd atoms in nanoparticles that can convert to ion-exchanged Pd^{2+} based on thermodynamic considerations requires calculation of both nanoparticle and ion-exchanged zeolite energies. Previous studies have shown that Pd^{2+} cations charge-compensating two Al tetrahedral sites (2Al) in the six-membered ring (6-MR) are the most thermodynamically stable ion-exchanged Pd^{2+}

Table 3.2: HSE06-D3(BJ)vdw-calculated 0 K Formation Energies (ΔE), and Formation Free Energies of Bulk PdO ($\Delta G^{\mathbf{form}}_{\mathbf{PdO_{bulk}}}$), and 3NN $\mathbf{Z_2Pd}$ ($\Delta G^{\mathbf{form}}_{\mathbf{Z_2Pd}}$) at 598 K and 873 K, 20 kPa $\mathbf{O_2}$, 0.014 kPa $\mathbf{H_2O}$.

		ΔG^{form} kJ (mol Pd)$^{-1}$	
reaction	ΔE kJ (mol Pd)$^{-1}$	598 K	873 K
$Pd_{bulk} + \frac{1}{2}O_2 \xrightarrow{\Delta G^{form}_{PdO_{bulk}}} PdO_{bulk}$ (3.5)	-111	-46	-16
$Pd_{bulk} + Z_2H_2 + \frac{1}{2}O_2 \xrightarrow{\Delta G^{form}_{Z_2Pd}} Z_2Pd + H_2O$ (3.6)	+8	-50	-74
$Pd_{bulk} + Z_2H_2 \rightarrow Z_2Pd + H_2O$ (3.7)	+119	-4	-58

species in CHA, represented here by Z_2Pd where 'Z' denotes the substitution of framework Si with Al (**Figure 3.3**).[242,247,261] The lowest energy Z_2Pd structure has 2Al in a third nearest neighbor (3NN) arrangement (0 kJ mol^{-1}), followed by the 2NN configuration (+65–80 kJ mol^{-1}).[242,247,261,262] One Al T-site (1Al) can be charge-compensated by Pd^+ cations (ZPd), or by Pd^{2+} as $[PdOH]^+$ (ZPdOH). The ZPd structure is +28–60 kJ mol^{-1} higher in energy than 3NN Z_2Pd.[242,247] The existence of Pd^+ after high temperature treatments in air with and without H_2O is debated in literature;[242] direct characterization of Pd^+ has been reported only from EPR measurements of Pd/Y zeolites performed under vacuum and after H_2 treatment at 298 K.[84] ZPdOH has been identified in detectable amounts only for CHA materials containing a larger number of ion-exchanged Pd^{2+} species than the number of 2Al sites in the 6-MR,[17] and is computed to be +60–79 kJ mol^{-1} higher in energy than 3NN Z_2Pd.[242,247,262] The Pd content of the Pd-CHA-X-ND samples here (Pd/Al = 0.05–0.08) are much lower than the number of available 2Al 6-MR sites quantified by Co^{2+} titration (Co^{2+}/Al = 0.12). Thus, we expect Pd^{2+} in the 6MR 3NN configuration to be the predominant cationic species in our materials; however, for comparison, we also considered 2NN Z_2Pd, ZPd and ZPdOH in the analyses below.

We next computed the thermodynamics of oxidation of bulk metallic Pd (Pd_{bulk}) with O_2 to form either bulk PdO (PdO_{bulk}) or ion-exchanged Pd cations (additional details in Section S5, SI). **Table 3.2** reports reaction energies (ΔE) and free energies (ΔG^{form}) for the formation of PdO_{bulk} from Pd_{bulk} (Eq. 3.5), and for the formation of 3NN Z_2Pd sites from either Pd_{bulk} (Eq. 3.6) or PdO_{bulk} (Eq. 3.7), at conditions representative of the high-temperature air treatments (598–873 K, 20 kPa O_2, impurity H_2O estimated as 0.014 kPa H_2O) of the Pd-CHA-X-ND samples discussed in Section 3.1.2. The conversion of either Pd_{bulk} or PdO_{bulk} to 3NN Z_2Pd sites is endothermic, but thermodynamically favorable (exergonic) at temperatures >576 K (0.014 kPa H_2O, $\log_{10}(P_{O_2}/P^{\circ}) >$ -9.5 (Figure S5.2, SI). Reaction energies to form 2NN Z_2Pd, ZPd and ZPdOH sites are >27 kJ mol^{-1} more endothermic than to form 3NN Z_2Pd sites (Table S5.1 and Figure S5.2, SI). These results demonstrate that conversion of bulk metallic Pd to either PdO agglomerates or to 3NN Z_2Pd sites is thermodynamically favorable over the range of high-temperature air treatments studied experimentally and suggest that the relative difference in the free energies of PdO agglomerates and Z_2Pd cations will influence Pd speciation.

To compare our thermodynamic predictions to the experimental Pd redispersion data in **Figure 3.2**, we estimated the thermodynamic limit of conversion of Pd particles to Z_2Pd (X_{Z_2Pd}) for a range of particle sizes (d_{Pd} = 2–100 nm) by considering a Boltzmann distribution of the equilibrium population of PdO particles and Z_2Pd cations (Eq. 3.8):[185]

$$X_{Z_2Pd}\left(P_{O_2}, P_{H_2O}, d_{Pd}, T\right) = \frac{\left(\frac{N_{2Al}}{N_{Pd}}\right) \exp\left(\frac{-\Delta G^{form}_{Z_2Pd}\left(P_{O_2},P_{H_2O},T\right)-\Delta G^{form}_{PdO}\left(P_{O_2},d_{Pd},T\right)}{k_B T}\right)}{\left(\frac{N_{2Al}}{N_{Pd}}\right) \exp\left(\frac{-\Delta G^{form}_{Z_2Pd}\left(P_{O_2},P_{H_2O},T\right)-\Delta G^{form}_{PdO}\left(P_{O_2},d_{Pd},T\right)}{k_B T}\right) + 1} \tag{3.8}$$

where N_{2Al}/N_{Pd} is the ratio of the number of 6-MR 2Al sites as quantified by Co^{2+} titration,[101] and the number of Pd quantified by ICP. Analogous results for 2NN Z_2Pd, ZPd and ZPdOH are reported in Figure S5.4, SI. Particle size-dependent free energies of Pd and PdO nanoparticles were determined relative to bulk free energies using the free energy model for nanoparticles adhered to a support developed by Campbell and coworkers[253–255] using calorimetric measurements:

$$\Delta G\left(d, P_{O_2},\ T\right) = \left(3\gamma\left(P_{O_2},\ T\right) - E_{adh}\right)\left(1 + \frac{1.5}{d}\right)\left(\frac{2\rho}{d}\right) \tag{3.9}$$

where γ is the particle surface energy (estimated from DFT), E_{adh} is the adhesion energy of the particle to the support (estimated from literature values and our TEM data), d is the particle diameter, and ρ is the volume normalized per mole of Pd; additional details are reported in Section 3.2.4. Expansion of particle volume due to the oxidation of Pd to PdO was accounted for by including a volume expansion factor of 1.19 (described in Section 3.2.4).

Figure 3.4a shows the results for the compositional parameters (N_{2Al}/N_{Pd} and d_{Pd}) corresponding to the Pd-CHA-X-ND zeolites (**Table 3.1**) and their respective air treatment conditions (**Figure 3.2**). Blue and yellow regions of **Figure 3.4a** denote complete conversion of metallic Pd particles to PdO agglomerates and to Z_2Pd sites, respectively. **Figure 3.4a** shows that complete conversion of 2 nm (squares), 7 nm (circles), and 14 nm (triangles) Pd particles to Z_2Pd is thermodynamically feasible at all the air treatment conditions in **Figure 3.2** (598–873 K, 20 kPa O_2, 0.014 kPa H_2O), and these results are insensitive to perturbations in PdO adhesion energy (contact angle varied from 60° to 120°) and surface free energy ($\pm$ 0.2 J m^{-2}) within the particle size-dependent free energy model (Figures S5.5-5.6, SI). The thermodynamic predictions for 2 nm particles are consistent with the experimental results for Pd-

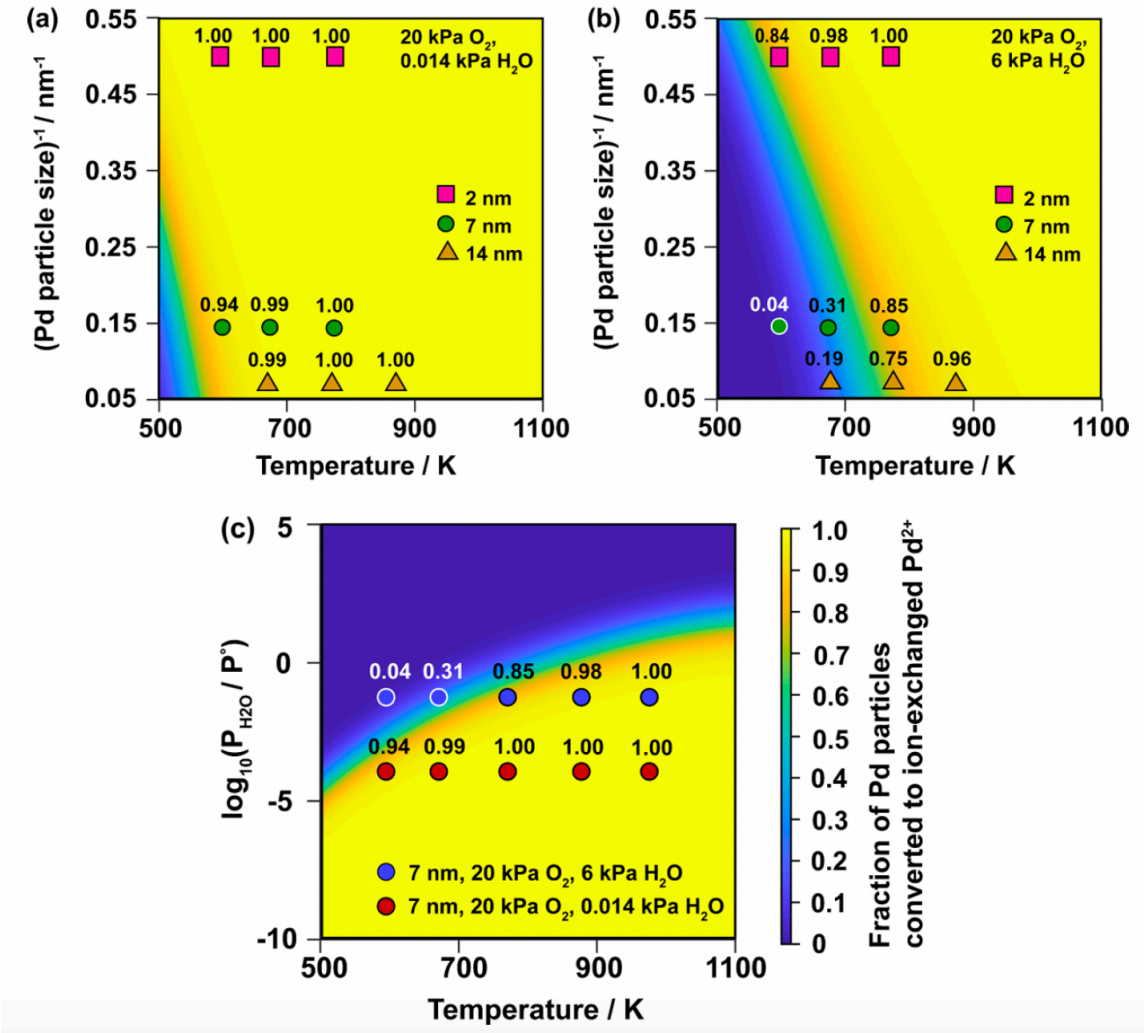

Figure 3.4: Pd particle size-dependent thermodynamic phase diagram for the conversion of Pd particles to Z_2Pd in CHA (Si/Al =12, Pd/Al = 0.06) under (a) 20 kPa O_2, 0.014 kPa H_2O and (b) 20 kPa O_2, 6 kPa H_2O, based on HSE06-D3(BJ)vdw calculated energies. The fraction of Pd particles converted to Z_2Pd for 2 nm (squares), 7 nm (circles), and 14 nm (triangles) Pd particles at the experimental air treatment conditions for Pd-CHA-X-ND samples are labeled. (c) Thermodynamic phase diagram for the conversion of 7 nm Pd particle to ion-exchanged Pd^{2+} cations on CHA (Si/Al =12, Pd/Al = 0.06) as a function of temperature and P_{H_2O}. The fraction of Pd particles converted to ion-exchanged Pd^{2+} cations at 20 kPa O_2, 0.014 kPa H_2O (red circles), and 20 kPa O_2, 6 kPa H_2O (blue circles) at treatment temperatures of 598–1023 K are labeled.

CHA-2-ND, which contained predominantly ion-exchanged Pd^{2+} after treatment to 673 or 773 K. However, for 7 and 14 nm particles, the computed fractions of Pd particles converted to Z_2Pd sites (~1.00) are significantly higher than the amount of ion-exchanged Pd^{2+} observed experimentally for Pd-CHA-7-ND and Pd-CHA-14-ND (598–773 K). Further, our model predicts complete oxidation of metallic Pd with O_2 to mononuclear Pd^{2+} species (i.e., either agglomerated PdO or Z_2Pd) under these conditions; yet, a residual fraction of metallic Pd persists on both Pd-CHA-7-ND and Pd-CHA-14-ND following air treatments (598 K for Pd-CHA-7-ND and 598–873 K for Pd-CHA-14-ND). Air treatment of Pd-CHA-14-ND at 673 K for 1 h and 5 h formed the same amount of ion-exchanged Pd^{2+} and consumed the same amount of H_2 per Pd (Table S4.1 and Figure S4.3, SI). These results, together with our thermodynamic modeling, suggest that complete conversion of large Pd particles (7–14 nm) to ion-exchanged Pd^{2+} is not thermodynamically limited at these conditions (598–873 K, 20 kPa O_2, 0.014 kPa H_2O), and that kinetic barriers are instead responsible for the incomplete oxidation and disintegration of large Pd particles into ion sites.

3.3.1.4 Effect of H_2O on the Conversion of Agglomerated Pd Particles to Exchanged Pd^{2+} Ions.

The addition of H_2O to the air stream has been proposed to facilitate the mobility of Pd, causing a greater fraction of agglomerated PdO domains to convert to Pd^{2+} cations.[12] To determine the thermodynamic influence of H_2O pressure on Pd structural interconversion, we constructed phase diagrams for air treatment conditions with higher H_2O partial pressures (6 kPa). **Figure 3.4b** shows the fraction of Pd particles converted to Z_2Pd at the different treatment temperatures studied for Pd-CHA-X-ND samples, which are labeled for comparison with **Figure 3.4a**. We

considered a representative Pd particle size of 7 nm and show its conversion to Z_2Pd as a function of temperature and P_{H_2O} in **Figure 3.4c** at treatment conditions of 20 kPa O_2 with 0.014 kPa H_2O (red circles) and 6 kPa H_2O (blue circles). Analogous phase diagrams for Pd particle sizes of 2 and 14 nm are reported in Figure S5.12, SI.

Our results predict that increasing P_{H_2O} thermodynamically limits the amount of Z_2Pd formed, and while the X_{Z_2Pd} values predicted vary within ± 20% (Figures S5.9–5.11, SI) depending on the precise values used for nanoparticle adhesion and surface energy, they are consistently lower than those predicted in dry air conditions (**Figure 3.4a**). The inhibiting effect of H_2O is especially pronounced for larger Pd particles at temperatures <773 K. Our model predicts that 7 and 14 nm Pd particles almost fully convert to ion-exchanged Pd^{2+} during air treatments >600 K in the presence of 0.014 kPa H_2O (**Figure 3.4a**), but that the conversion of Pd particles decreases (to 0.31 and 0.19 for 7 and 14 nm, respectively) when P_{H_2O} is increased to 6 kPa (**Figure 3.4b**). Conversely, the effect of higher P_{H_2O} at temperatures >600 K is negligible for 2 nm Pd particles, which are predicted to fully convert to Z_2Pd during air treatments in the presence of 0.014 or 6 kPa H_2O. At conditions typically representative of practical PNA applications (2.5–6 kPa H_2O),[109] an increase in P_{H_2O} favors formation of larger fractions of PdO agglomerates at temperatures <800 K for d_{Pd} = 2–14 nm. The H_2O promoted formation of agglomerated PdO becomes attenuated with increasing temperature due to the increase in the entropic contribution of H_2O formation relative to the enthalpy of reaction (Figure S5.13, SI). Consequently, complete conversion of Pd particles to Z_2Pd is again predicted for all the Pd-CHA-X-ND zeolites at temperatures >800 K.

Our thermodynamic predictions suggest that adding H_2O to air streams would inhibit the structural transformation of agglomerated PdO domains to ion-exchanged Pd^{2+}

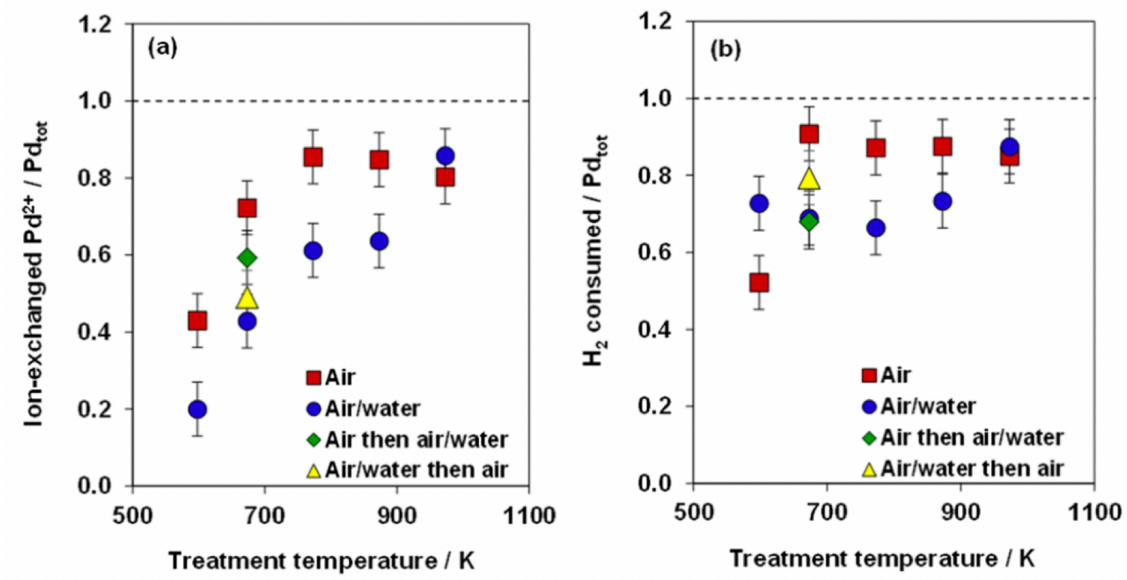

Figure 3.5: (a) The amount of ion-exchanged Pd^{2+} and (b) total H_2 consumed normalized per total Pd as a function of treatment temperature in flowing air (squares), 6 kPa H_2O in balance air (circles), air (1 h) then adding 6 kPa H_2O (1 h, diamond), and 6 kPa H_2O in balance air (1 h) then air (1 h, triangle) for the Pd-CHA-7-ND material. Dashed line represents theoretical maximum values. H_2 TPR profiles are reported in Figure S4.7, SI.

cations. To experimentally test these predictions, the as-deposited Pd-CHA-7-ND sample was treated in either flowing air with 6 kPa H_2O or without H_2O at temperatures between 673–973 K, and the ion-exchanged Pd^{2+} content and H_2 consumption (per Pd) were quantified with H_2 TPR. **Figure 3.5** and Table S4.3, SI show that fewer ion-exchanged Pd^{2+} sites were formed and the PdO content increased after the wet air treatment in comparison to the dry air treatment at temperatures <900 K, which is qualitatively consistent with our thermodynamic predictions (**Figure 3.4**) that increasing H_2O pressures should reduce Pd^{2+} cation content and increase the agglomerated PdO content. Similar results have been reported for atomically dispersed Pt on CeO_2[263] where steam exposure led to an increase in particle agglomeration. Additionally, a larger fraction of residual metallic Pd remained after wet air treatments than after dry air treatments for temperatures between 673 and 873 K, an effect that may be due to H_2O-induced hydroxylation of particle surfaces inhibiting the complete oxidation of Pd.[264] Treatment of Pd-CHA-7-ND in air at 973 K with and without H_2O resulted in the same amount of ion-exchanged Pd^{2+} (0.80–0.85 per total Pd) and H_2 consumption (0.87–0.88 per total Pd), consistent with the absence of an H_2O pressure dependence on our thermodynamic predictions at 973 K (**Figure 3.4**). Analogous experiments on Pd-CHA-2-ND (Figures S4.4-4.5, SI) evidence no residual metallic Pd, and similar fractions of Pd^{2+} and PdO when either air alone or air and 6 kPa H_2O were co-fed, consistent with thermodynamic predictions that the effect of H_2O becomes attenuated for small particle sizes (**Figure 3.4b**). Together, our thermodynamic and experimental results demonstrate that co-feeding H_2O at temperatures of 673–873 K does not facilitate the transformation of PdO to ion-exchanged Pd^{2+}, in contrast to proposals in previous studies[12] wherein the treatment temperature itself was likely the dominant influence on the extent of agglomerated PdO converted to ion-exchanged Pd^{2+} cations. Instead, water promotes the formation of PdO, and this

Table 3.3: Pd Speciation After 673 K and 773 K Sequential Air and Air/Water Treatments on Pd-CHA-2-ND[a]

	673 K air	673 K subsequent air/ water	773 K air	773 K subsequent air/ water
PdO agglomerates/ Pd_{tot}	0.17	0.27	0.00	0.02
Mononuclear Pd^{2+}/ Pd_{tot}	0.83	0.71	1.08	1.00
H_2 consumed/ Pd_{tot}	1.00	0.98	1.08	1.02

[a] H_2 TPR profiles reported in Figure S4.14, Supporting Information.

effect becomes attenuated with decreasing particle size and increasing temperature.

The decrease in cation formation when H_2O is co-fed (673–873 K) could reflect consequences of H_2O inhibiting the kinetics of Pd redispersion to Pd^{2+} cations, or changing the thermodynamic equilibrium to promote the formation of PdO agglomerates from Pd^{2+} cations, in the latter case as suggested by our thermodynamic calculations and formation of H_2O as a product in the cation exchange reaction (Eq. 3.7). To determine if Pd^{2+} cations could reversibly transform to PdO agglomerates under wet conditions, the as-deposited Pd-CHA-7-ND sample was first treated in flowing dry air to 673 K and held for 1 h, and then exposed to a wet air stream (6 kPa H_2O) stream for 1 h (**Figure 3.5**, green diamond). The amount of ion-exchanged Pd^{2+} (per total Pd) decreased from 0.72 (dry air) to 0.59 (dry air followed by wet air), but did not reach the value measured on the sample exposed only to the wet air treatment (0.43). These results demonstrate that starting from a distribution of Pd^{2+} cations and PdO agglomerates the addition of H_2O to the air stream results in the loss of Pd^{2+} cations, an effect that shows that the reaction Z_2H_2 + PdO $\Leftrightarrow$ Z_2Pd + H_2O becomes reversible at 6 kPa H_2O, an effect that must be driven by thermodynamics.

To further confirm that PdO agglomerates form from Pd^{2+} cations under hydrous conditions, and the generality of this observation, analogous experiments were performed at 673 K and 773 K on the Pd-CHA-2-ND sample. The sample was treated in flowing dry air to 673 K and held for 1 h, and then exposed to a wet air stream (6 kPa H_2O) stream for 24 h, and the Pd speciation quantified using H_2 TPR (Figure S4.5 and **Table 3.3**). Exposure to the wet air stream decreased the fraction of ion-exchanged Pd^{2+} (per total Pd) from 0.83 (dry air) to 0.71 (dry air followed by wet air), and resulted in a concomitant increase of PdO from 0.17 (dry air) to 0.27 (dry air followed by wet air). Similar experiments performed at 773 K (Figure S4.14, Table S4.5, SI) showed an increase from 0.00 to 0.02 of the fraction of PdO after air/water exposure, consistent with the suppression of PdO formation at small particle sizes and higher temperatures predicted in **Figure 3.4b**.

Introducing H_2O to the 673 K air stream after 1 h treatment of Pd-CHA-7-ND did not reversibly generate the same distribution formed after the H_2O-only treatment; moreover, a longer treatment time (18 h) in the wet air stream following an air-only treatment did not change the ion-exchanged Pd^{2+} content or H_2 consumption per total Pd (Table S4.2 and Figure S4.6, SI), demonstrating that the values reported after a 1 h treatment in **Figure 3.5** reflect a pseudo steady-state distribution of agglomerated PdO and ion-exchanged Pd^{2+}. Additionally, the reverse experiment was performed where the Pd-CHA-7-ND sample was first treated in wet air (6 kPa H_2O) to 673 K for 1 h, followed by removing the H_2O from the air stream and holding for 1 h. The resulting ion-exchanged Pd^{2+} (per total Pd) increased slightly from 0.43 (wetted air only) to 0.49, which was significantly below the result on the sample exposed only to a dry air treatment (0.72). The partially irreversible nature of Pd structural interconversion between dry and wet (6 kPa H_2O) air treatments can be

rationalized from conclusions of prior work[17] that showed sample treatment history influences the spatial distribution and particle sizes of Pd domains. Here, the first dry air treatment (673 K, 1 h) of Pd-CHA-7-ND converted the 7 nm Pd particles initially present at the exterior zeolite crystallite to different PdO domain sizes and ion-exchanged Pd^{2+} sites distributed deeper within the interior of zeolite crystallites; thus, upon subsequent addition of H_2O to the flowing air stream, there was a different distribution of PdO particle sizes with some amount of ion-exchange Pd^{2+}. Consistent with these observations, exposure of the Pd-CHA-2-ND sample to air at 1023 K, followed by air/water at 773 K did not result in formation of PdO (Figure S4.14, SI). Taken together, our results show that at low temperatures the addition of H_2O to flowing air generates a thermodynamic driving force for the reverse exchange reaction to occur (Eq. 3.7), forming PdO agglomerates from Pd^{2+} cations, and that the sample history and spatial distribution of Pd^{2+} sites are important factors in the extent of reversibility between Pd^{2+}/PdO distributions.

3.3.2 Quantifying Apparent Rates of Pd Redispersion

3.3.2.1 Effect of Treatment Temperature and H_2O on Rates of Pd Redispersion.

To deduce mechanistic information for structural interconversion, we monitored the conversion of agglomerated, metallic Pd domains to ion-exchanged Pd^{2+} sites as a function of time under flowing air at different temperatures. To explore the effects of the functional form of the particle size distribution on redispersion rates, a suite of Pd-CHA-X-LND samples were synthesized to contain varying average particle sizes (X=2.1, and 2.9 nm), using synthesis approaches that led to a more log-normally

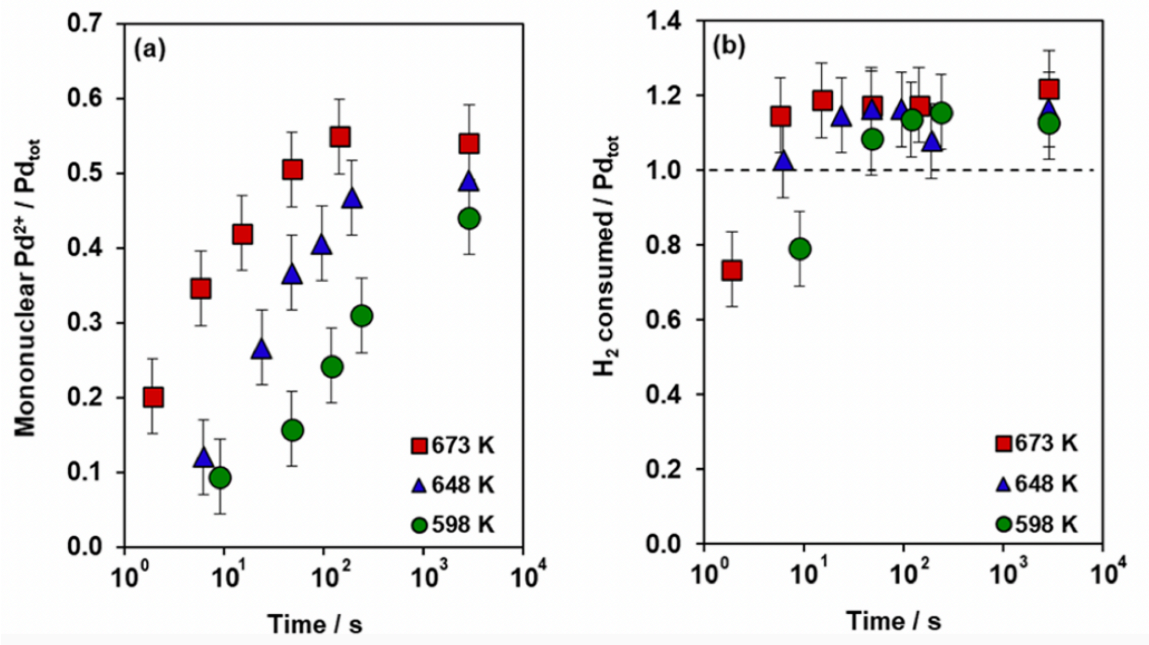

Figure 3.6: (a) The amount of ion-exchanged Pd^{2+} normalized per total Pd as a function of time during isothermal switching experiments for three different treatment temperatures (square: 673 K, triangle: 648 K, circle: 598 K) using the Pd-CHA-2.9-LND sample, (b) The total H_2 consumed normalized per total Pd from (a). Dashed line represents theoretical maximum amount. H_2 TPR profiles are in Figures S4.9 S4.11, SI.

distributed particle size distribution (denoted by 'LND' in the sample nomenclature, synthesis and characterization details in Section S1, SI) than samples prepared by colloidal Pd nanoparticle synthesis approaches.[76]

Figure 3.6 shows the amount of ion-exchanged Pd^{2+} as a function of time and temperature for the isothermal Pd redispersion rate measurements (further discussion on rate measurements in Section S6, SI) of the Pd-CHA-2.9-LND sample. The amount of ion-exchanged Pd^{2+} formed after treatment in air for 1 h increased systematically with temperature, which agrees with thermodynamic predictions (Section 3.3.1.3) that higher temperatures facilitate the conversion of agglomerated PdO particles to ion-exchanged Pd^{2+}, and is consistent with an activated process for structural

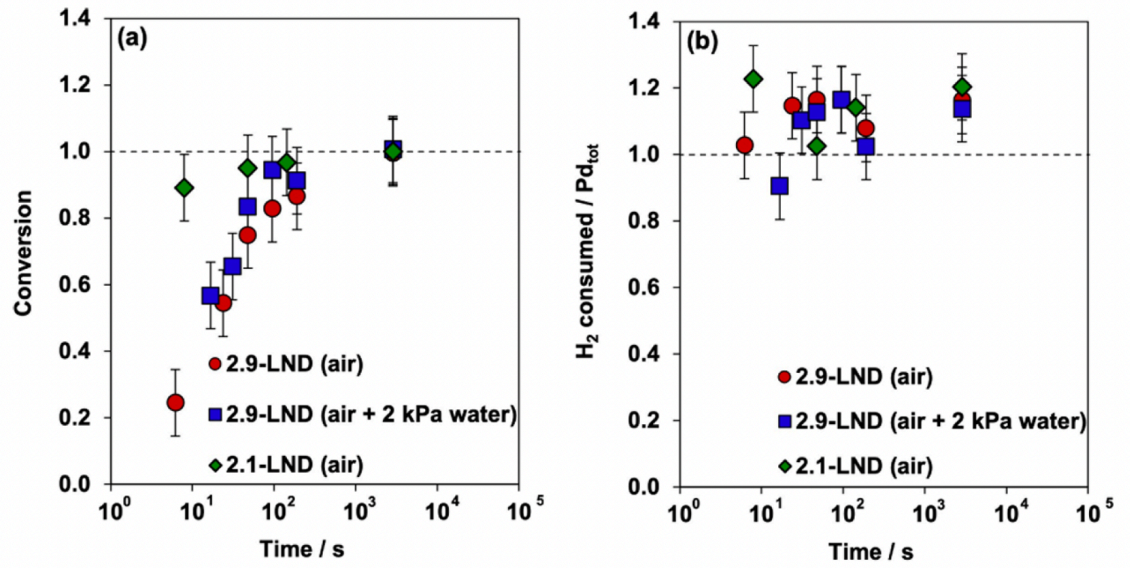

Figure 3.7: (a) The amount of ion-exchanged Pd^{2+} (normalized per ion-exchanged Pd^{2+} content after treatment for 1 h, and denoted as conversion) as a function of time during isothermal switching experiments performed at 648 K for Pd-CHA-2.9-LND sample in air (circles), 2 kPa H_2O in balance air (squares), and Pd-CHA-2.1-LND in air (diamonds). H_2 TPR profiles are in Figures S4.10, S4.12, and S4.13, SI. (b) H_2 consumed normalized to total Pd of materials in (a).

interconversion. **Figure 3.6b** shows that the H_2 consumption per Pd was approximately unity for all time points after 10 s, suggesting the observed ion-exchanged Pd^{2+} formation rates were not limited by metallic Pd oxidation to PdO with O_2. This observation demonstrates the mechanistic role of O_2 is only to oxidize metallic Pd; thus, the reported formation of ion-exchanged Pd^{2+} as a function of time reflects the rate of structural conversion of agglomerated PdO domains to ion-exchanged sites.

To determine the kinetic influence of H_2O on the apparent redispersion rate, we performed isothermal redispersion experiments on the Pd-CHA-2.9-LND sample with and without 2 kPa H_2O (**Figure 3.7**). Consistent with previous thermodynamic arguments, adding 2 kPa H_2O to the inlet air stream decreased the amount of ion-exchanged Pd^{2+} cations after treatment for 1 h (Figure S6.1, SI); however, when the

amount of exchange was normalized to the pseudo steady state value after 1 h (i.e., normalizing rates to the reversible fraction of Pd that can interconvert), the apparent rates of redispersion with and without H_2O were similar within error. Additionally, the H_2 consumption per total Pd was approximately unity for all time points measured, again demonstrating the rate of Pd redispersion was not limited by Pd oxidation. Therefore, co-feeding H_2O did not have a significant kinetic effect on the redispersion of PdO particles to ion-exchanged Pd^{2+} and, for this material and conditions of these measurements, H_2O apparently only influences the thermodynamics of the redispersion process.

Time-dependent redispersion measurements of the Pd-CHA-2.1-LND sample (**Figure 3.7**) showed faster apparent rates of redispersion to ion-exchanged Pd^{2+}. Notably, the shortest time point of 10 s resulted in almost complete conversion (0.9) of the Pd species that reversibly convert between agglomerated domains and ion-exchanged Pd^{2+}. Additionally, all the redispersion rates measured for Pd-CHA-2.1-LND showed H_2 consumptions per Pd near unity. These data suggest smaller Pd nanoparticles disintegrate at a faster rate for structural interconversion to ion-exchanged Pd^{2+}.

3.3.2.2 Kinetic Models for Pd Redispersion

Experimental data and atomistic simulation results for supported metal particles suggest that Ostwald ripening (OR) is the predominant mechanism for the disappearance of small nanoparticles and sintering compared to particle migration and coalescence.[199,265] The OR process is associated with the rapid disappearance of particles smaller than a critical radius, generating a pool of monomers that transport between particles through either gas phase or surface diffusion processes, resulting in the formation of larger particles. In contrast to conventional OR mechanisms, in the pres-

Scheme 3.1: Proposed scheme for Pd ion exchange via monomers generated from Ostwald ripening.

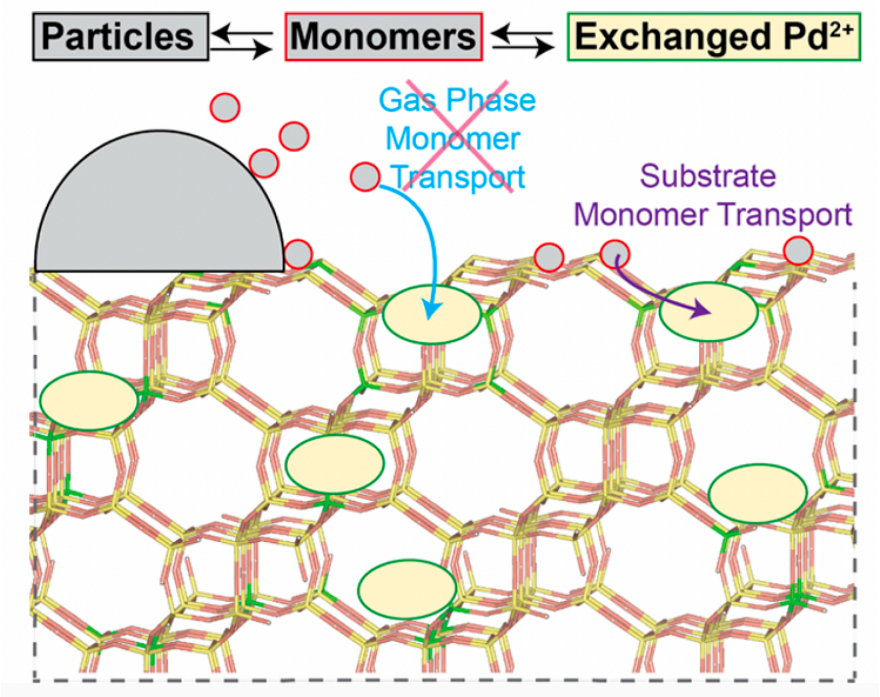

ence of framework Al ion-exchange sites in the zeolite support, we hypothesize that monomers ejected from the surface of PdO particles form either larger PdO agglomerates or ion-exchanged Pd^{2+} via an atom trapping mechanism (**Scheme 3.1**). **Figures 3.6** and **3.7** demonstrate that oxidation of metallic Pd to PdO is rapid relative to the rate of redispersion to Pd^{2+} cations, therefore we consider PdO to be the initial state of the particles in the redispersion mechanism. Plausible monomer-facilitated mechanisms proposed for the conversion of PdO nanoparticles to ion-exchanged Pd^{2+} involve the detachment of neutral, mobile species, such as Pd_1O_1 and $Pd_1(OH)_2$ from PdO agglomerates, and their successive reactions with the zeolitic Brønsted acid sites.[17,185,266] There are established kinetic models for OR-based particle sintering for supported metal catalysts,[204,267,268] however, kinetic models have not been reported that incorporate monomer migration and subsequent atom trapping of monomers on

surface/lattice defect or cation exchange sites.

Ripening of nanoparticles occurs by diffusion of monomers through the gas phase or on a substrate.[204,269–275] Wynblatt and Gjostein proposed that monomer transport via the gas phase takes place for metals with volatile metal oxides such as Pt.[267] Simulation results reported by Plessow et al. for dispersed Pt particles on silica using a modified Wynblatt-Gjostein gas-phase sintering model show agreement with the experimental data in the high-temperature regime (>1023 K) where higher oxygen pressures accelerated sintering via formation of volatile Pt_1O_2(g).[276] Recently, Goodman et al. performed similar gas-phase sintering simulations for Pd/SiO_2 to demonstrate that emission of Pd atoms in the vapor phase becomes substantially higher (5 atoms s^{-1} from a 8.8 nm Pd particle) with an increase in Pd vapor pressure at temperatures >1173 K.[277] Although the air treatment temperatures reported here (598–1023 K) are lower than those where gas-phase sintering has been shown to become appreciable, we explored the possibility of both gas-phase and substrate-mediated Pd redispersion.

To determine the feasibility of a gas phase OR process, we next computed the rate of formation of the most stable gas-phase Pd monomer, which was found to be $Pd(OH)_2$(g) (details in Section S8.1.1, SI), consistent with prior reports.[185] We estimated the pressure (P_k) of ejected $Pd(OH)_2$ (g) monomers in equilibrium with a PdO nanoparticle comprised of k atoms as:[185]

$$PdO_{bulk} + H_2O \xrightarrow{\Delta G^{form}_{Pd(OH)_2(g)}} Pd(OH)_2(g) \tag{3.10}$$

$$P_k = P_{H_2O} \exp\left(\frac{-\Delta G^{form}_{Pd(OH)_2(g)} + \frac{A_k\gamma}{k}}{k_B T}\right) \tag{3.11}$$

where γ is the average surface energy of the PdO surface from which monomers detach, A_k is the surface area of the particle, and $\Delta G^{\text{form}}_{\text{Pd(OH)}_2\text{(g)}}$ denotes the formation free energy of $Pd(OH)_2$(g) relative to bulk PdO. For a system with a distribution of particle sizes, the background pressure (P_b) of $Pd(OH)_2$(g) is given by:[271]

$$P_\text{b}=\frac{\sum_k A_k n_k P_k}{\sum_k A_k n_k} \tag{3.12}$$

where n_k is the surface density of the nanoparticle, and P_k is the equilibrium pressure of monomers calculated using Eq. 3.11. Subsequently, the influx of $Pd(OH)_2$(g) monomers J_k (monomers nm^{-2} s^{-1}) received by a PdO nanoparticle comprised of k atoms can be estimated using kinetic theory of gases:

$$J_k = \frac{(P_\text{b} - P_\text{k})}{\sqrt{2\pi m_{\text{Pd(OH)}_2\text{(g)}} k_\text{B} T}} \tag{3.13}$$

where $m_{\text{Pd(OH)}_2\text{(g)}}$ is the molecular mass of $Pd(OH)_2$(g). A lower background monomer pressure would correspondingly result in a lower monomer flux. For example, at 6 kPa H_2O, 20 kPa O_2, and 873 K, the particle size distribution for the Pd-CHA-7-ND sample (Figure S2.8, SI) generates a background monomer pressure of only 3.2×10^{-16} kPa, and 3.6×10^{-7} $Pd(OH)_2$ (g) monomers per second colliding with the surface of a 7 nm particle in the distribution. In comparison, a similar Pt particle size distribution has a collision frequency of 25 PtO_2 (g) monomers s^{-1} because of its substantially higher background monomer pressure (2.8×10^{-8} kPa). We also considered other plausible scenarios (e.g. PdO(g)) for gas phase monomer formation (Table S8.2, SI), but all such routes have fluxes that are even lower than the formation of $Pd(OH)_2$(g) from PdO agglomerates. The maximum rates of ion-exchange (Section S8.1.3, SI) for

the Pd-CHA-7-ND and Pd-CHA-2.9-LND samples (**Figure 3.7**) are 10^{-15} s^{-1} (673 K, d_{avg} = 7 nm), and 10^{-13} s^{-1} (648 K, d_{avg} = 2.9 nm), respectively. The observed rate of ion-exchange for Pd-CHA-2.9-LND (~10^{-4} s^{-1}) and the time scale reported in our experiments (**Figure 3.2**) for complete ion-exchange of Pd-CHA-7-ND (~1 h) are orders of magnitude faster than the computed gas phase rates.

The available data show that Pd redispersion does not occur through the gas phase at temperatures <900 K. First, the observed redispersion rates at the conditions of our experiments are at least ~9 orders of magnitude faster than what would be expected for a gas phase process. Challa et al.[272] invoked similar calculations for emission of Ni monomers to show that monomers transport on the support during the disappearance of small Ni nanoparticles supported on $MgAl_2O_3$. Second, since $Pd(OH)_2$(g) monomer flux is directly proportional to P_{H_2O} in a gas phase process (Eq.s 3.10 and 3.11) changes in P_{H_2O} should reflect changes on the rates of formation of ion-exchanged Pd^{2+}.

For example, comparison of experimental and simulation results for isothermal Pt sintering (873 K) showed faster rates of sintering with increases in P_{O_2}.[276] However, as evidenced by the results of the isothermal redispersion air treatment with and without 2 kPa H_2O (**Figure 3.7**), there was no change in the apparent rates of redispersion, again suggesting that diffusion of monomers on the zeolite substrate is the dominant process. Finally, if the OR process occurred via gaseous monomers, it would be expected that all oxidized Pd would disintegrate and form cations, but this is not the case as demonstrated in **Figure 3.2**. Taken together, these results imply that interconversion of Pd particles to ion-exchanged Pd occurs through diffusion of monomer species on the zeolite substrate at temperatures <900 K.

To elucidate the particle size dependent nature of the redispersion of PdO agglomer-

ates and ion exchange process, we next incorporated an atom trapping surface reaction assumed to be first order in both Z_2H_2 exchange sites and mean-field substrate monomer concentration:

$$\frac{\mathrm{d}Z_2H_2}{\mathrm{d}t} = -k_{\mathrm{rxn}}[Z_2H_2]\,[\mathrm{monomer}] \tag{3.14}$$

into the system of differential equations that correspond to the mass balance of a substrate-mediated OR kinetic model[270–272] that accounts for activated monomer formation, activated diffusion of monomers on a substrate, and exchange of monomers between particles comprised of k Pd atoms:

$$\frac{\mathrm{d}C_k}{\mathrm{d}t} = -K_{\mathrm{os}}C_{\mathrm{inf}}\left|\exp\left(\frac{G_{k*}}{k_BT}\right) - \exp\left(\frac{G_k}{k_BT}\right)\right|C_k d_k + (\mathrm{generation}) \tag{3.15}$$

where, C_k is the particle number density (particles nm^{-2}), ΔG_k is the nanoparticle free energy with respect to bulk PdO (computed using the relation developed by Campbell et al. in Eq. 3.9), K_{os} is the lumped pre-exponential factor for OR, C_{inf} is the far-field concentration of monomers in equilibrium with an infinite size particle at an infinite distance from the particle-support interface, and d_k is the effective particle diameter (Table S8.1, SI). Full details of the OR kinetic model are reported in Section S8.2, SI. Depending on the number of Pd atoms that correspond to the critical particle radius (k_*, determined at each time step as described in Section S8.2, SI), a particle will either grow ($k > k_*$) by consuming monomers or shrink ($k < k_*$) by detaching monomers. The generation term represents formation of a new particle with k Pd

atoms:

$$(\text{generation}) = \begin{cases} K_{\text{os}} C_{\text{inf}} \left| \exp\left(\frac{G_{k*}}{k_B T}\right) - \exp\left(\frac{G_{k-1}}{k_B T}\right) \right| C_{k-1} d_{k-1} \;\; if \;\; k > \;\; k_* \\ 0 \qquad\qquad\qquad\qquad\qquad\qquad\qquad\qquad\qquad\qquad\qquad\qquad if \;\; k = k_* \\ K_{\text{os}} C_{\text{inf}} \left| \exp\left(\frac{G_{k*}}{k_B T}\right) - \exp\left(\frac{G_{k+1}}{k_B T}\right) \right| C_{k+1} d_{k+1} \;\; if \;\; k < \;\; k_* \end{cases} \tag{3.16}$$

Eq. 3.15 shows that the driving force for the OR process, $\left| \exp\left(\frac{\Delta G_{k*}}{k_B T}\right) - \exp\left(\frac{\Delta G_k}{k_B T}\right) \right|$, originates from the free energy difference between nanoparticles of different sizes. The resulting monomer mass balance is:

$$\frac{\mathrm{d}[\text{monomer}]}{\mathrm{d}t} = \frac{\mathrm{d}[\mathrm{Z_2H_2}]}{\mathrm{d}t} + \sum_{k=2}^{k_*} \frac{\mathrm{d}C_k}{\mathrm{d}t} - \sum_{k=k_*}^{\max\ k} \frac{\mathrm{d}C_k}{\mathrm{d}t} \tag{3.17}$$

and describes monomer consumption due to atom trapping at Z_2H_2 sites, generation of monomers from smaller particles, and consumption of monomers by larger particles.

The four model parameters are the rate constant for cation exchange from monomers (k_{rxn}, nm^2 s^{-1}), the OR rate constant associated with activated diffusion of monomers (K_{os}, nm s^{-1}), the far-field concentration of monomers (C_{inf}, nm^2 related to the monomer formation energy), and the surface energy of the nanoparticles (γ, J m^{-2} implicit in ΔG_k). Typical reported values for these parameters are shown in Table S8.5, SI. We randomly generated initial Pd particle size distributions that are consistent with the log-normal distribution (LND) means and standard deviations of the experimentally observed particle size distributions for the Pd-zeolite samples in **Figure 3.7** (Table S2.1, SI). We started by assuming these particles oxidize rapidly and their initial state is PdO, as evidenced by **Figures 3.6b** and **3.7b**, and then used

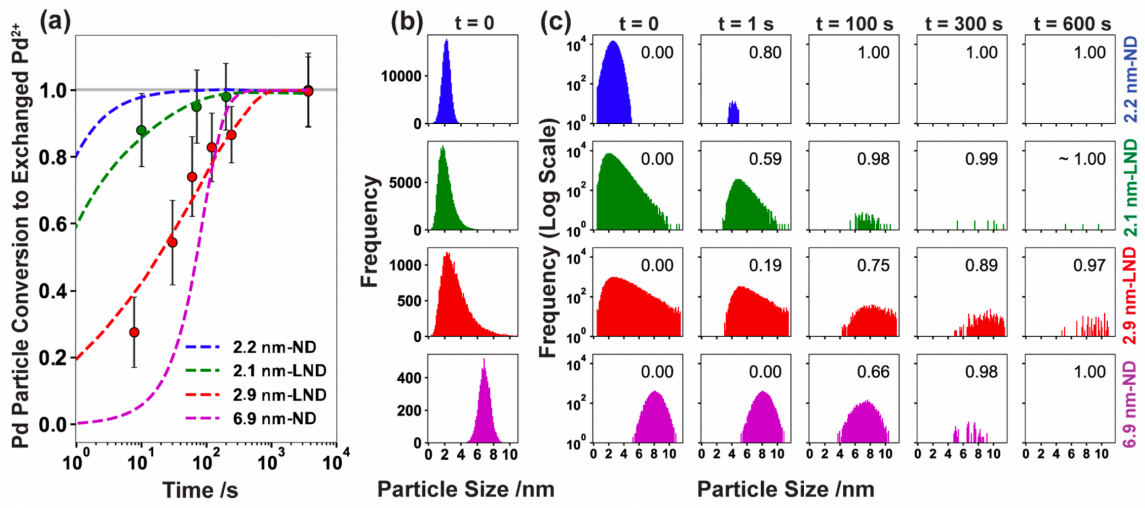

Figure 3.8: (a) The kMC predicted redispersion kinetics at $T = 648$ K. Model parameters were estimated by fitting the 2.9 nm averaged log-normally distributed (LND) sample (red traces) to experimentally measured conversion (red circles). The error bars denote one standard deviation of experimental measurements. (b) Initial simulated Pd particle size distributions. (c) The evolution of PdO particle size distributions as a function of time, the number on the top right in each histogram shows the conversion of Pd atoms in PdO particles to exchanged Pd^{2+}. Simulation results for $t < 1$ s are shown in Figure S8.4, SI.

kinetic Monte Carlo (kMC) to solve the resulting system of differential equations (Section S8.2, SI) for the particle size distribution, monomer concentration, and the fraction of ion exchange as a function of time. The randomly generated particle size distributions, and kMC itself, give stochastic results; therefore, the results from 350 independent kMC simulations were averaged to generate predictions for the fractional extent of ion exchange. Figure S8.3, SI shows that by 250 kMC simulations results are converged. We regressed the four model parameters using only the measured conversion of Pd-CHA-2.9-LND (**Figure 3.7**); regressed OR parameter values fall into the ranges of those previously reported (Table S8.5, SI) and the regressed surface energy is within 0.1 J m^{-2} of our DFT-computed value.

Figure 3.8 reports kMC results starting from a log-normal distribution (LND) of

nanoparticles, consistent with the samples prepared via incipient wetness impregnation (Pd-CHA-2.1-LND (red traces), Pd-CHA-2.9-LND (green traces)), or a normal distribution (ND), consistent with the samples prepared from monodisperse Pd particles via colloidal synthesis (Pd-CHA-2-ND (blue traces, 2.2 nm, particle size distribution in Figure S2.7, SI), Pd-CHA-7-ND (purple traces, 6.9 nm, particle size distribution in Figure S2.8, SI)). The model predicts that larger particles (2.9 nm) have slower rates of ion-exchange compared to the smaller particles (2.1 nm) and captures the differences in rate between the two particle size distributions that are observed experimentally (**Figure 3.7**). We emphasize that the regressed model parameters are not particle size-dependent, and the effect of particle size on kinetics is described solely by the physics of OR and atom trapping in the model. Smaller particles result in a higher substrate monomer concentration, which drives the exchange reaction, and has a strong dependence on particle size. As released monomers are consumed by the faster trapping reaction the particles continue to lose monomers onto the substrate, and the exchangeable fraction of Pd for all distributions is completely exhausted within 1000 s. **Figure 3.8b** shows that the narrower particle size distributions for the ND samples (Pd-CHA-2-ND) result in faster rates of ion exchange compared to the LND samples with similar average particle size (Pd-CHA-2.1-LND and Pd-CHA-2.9-LND), because the largest particles located in the trailing tail of the LND particle size distribution are the slowest to disintegrate. The Pd-CHA-7-ND sample is predicted to reach complete conversion of exchangeable Pd by 400 s, which is consistent with experimental observations that full ion-exchange is reached within 1 h. The model predicts the Pd-CHA-7-ND sample will reach complete conversion more rapidly than the Pd-CHA-2.9-LND, highlighting the effect of size distribution. The Pd-CHA-7-ND sample has a longer induction period than Pd-CHA-2.9-LND (Figure S8.4, SI), however, once redispersion starts, the majority of particles in a tighter distribution

will quickly release monomers. Although the unexchangeable fraction of Pd reported in **Figure 3.2** is not accounted for in our kinetic model, the substrate-mediated OR model accurately describes the kinetics of the exchangeable Pd fraction, suggesting that the experimentally observed incomplete ion-exchange likely reflects the non-mean-field nature of diffusion through a porous three-dimensional substrate and the spatial arrangement of particles at external zeolite crystallite surfaces. The K_{os} and k_{rxn} parameters depend on interparticle distances, and distances between particles and exchange sites, respectively, and their regressed values represent a weighted average over different local environments of particles in the samples. These parameters may vary with changes in the spatial distribution of particles[185,278] and exchange sites, and do not account for pore blocking, which may result in incomplete ion-exchange.[279,280] Further, the molecular structure(s) of the monomer intermediates formed on the zeolite substrate are unknown; their energetics in our model are described by the regressed k_{rxn}, K_{os}, and C_{inf} parameters. Nevertheless, our kinetic model captures the observed kinetic dependence of redispersion on particle size and demonstrates that integration of atom trapping kinetics with an OR kinetic model is consistent with the available experimental data.

3.4 Conclusions

We combined precise catalyst synthesis techniques, quantitative site characterization methods, and computational thermodynamic and kinetic models to examine the relative importance of the thermodynamic and kinetic factors governing the interconversion of Pd nanoparticles and ion-exchanged Pd^{2+} cation sites in CHA zeolites under high temperature (593–973 K) air treatments with and without H_2O. To facilitate

quantitative measurements of Pd particle redispersion rates and their dependence on the Pd initial particle size and particle size distribution, we prepared a series of Pd-CHA materials using two different synthetic approaches; deposition of colloidal Pd nanoparticle suspensions to form monodisperse, normally distributed Pd particles of different sizes (2–14 nm), and incipient wetness impregnation yielding log-normally distributed particles of varying average sizes (2.1 and 2.9 nm). Smaller Pd nanoparticles (2 nm) readily converted to ion-exchanged Pd^{2+} species in air. The conversion of larger metallic Pd nanoparticles (7, 14 nm) to PdO domains and ion-exchanged Pd^{2+} was observed to be lower than the thermodynamic distributions predicted by DFT, indicating that larger metallic particles have kinetic barriers for oxidation with O_2 to PdO and for the subsequent disintegration of PdO to ion-exchanged Pd^{2+} sites. Additionally, increasing the H_2O partial pressure shifts the thermodynamic distribution away from Pd^{2+} sites and toward agglomerated PdO domains, suggesting that H_2O present in exhaust streams facilitates Pd deactivation to PdO agglomerated phases. Our results suggest that the widely observed agglomeration and deactivation of Pd cation-exchanged zeolites in low temperature hydrous environments (e.g. Wacker oxidation, automotive exhaust, and PNAs) reflect thermodynamic factors that may be deleterious to the long-term storage and stability of atomically-dispersed Pd-zeolite materials.

To deduce mechanistic information of the Pd redispersion process, quantitative measurements of Pd nanoparticle conversion to ion-exchanged Pd^{2+} sites in air with and without H_2O were performed isothermally (598–673 K) with varying treatment time (0.003–1.0 h). The oxidation of metallic Pd with O_2 is complete after 0.003 h of treatment time, and thus kinetically irrelevant for apparent rates of PdO conversion to ion-exchanged Pd^{2+} sites. Additionally, a predominantly PdO-containing CHA

material treated in either inert (He) or air to 648 K resulted in similar extents of PdO conversion to ion-exchanged Pd^{2+}, further reinforcing that the dominant mechanistic role of O_2 is to oxidize agglomerated metallic Pd to PdO. In the presence of H_2O, the extent of interconversion from Pd^{2+} to PdO is lower when following higher temperature pretreatments, suggesting that Pd^{2+} ions located deeper in the zeolite crystallite are kinetically inaccessible at these conditions.[17] Under these conditions, quantum chemical calculations predict $Pd(OH)_2(g)$ is the most thermodynamically favorable gaseous Pd species, suggesting that adding H_2O to the air stream may facilitate hydroxylation of the PdO surface to increase the rate of forming $Pd(OH)_2(g)$ intermediates. However, computed rates of gas-phase redispersion kinetics are orders of magnitude slower than experimentally observed rates, and experiments performed with H_2O (2 kPa) added to the air stream (648 K) show that H_2O pressure (0–2 kPa) did not influence Pd redispersion rates normalized by the fraction of Pd that reversibly interconverts between particles and cation sites. These observations show that H_2O strongly influences the thermodynamics, but not the kinetics, of Pd structural interconversion at 648 K. Smaller Pd nanoparticles result in faster disintegration rates and a greater thermodynamic driving force to form ion-exchanged Pd^{2+}. Our kMC simulations of a surface-diffusion mediated OR process, with exchange of mobile Pd species at ion-trapping sites in the zeolite support (formed by Al substitution), are consistent with the particle size dependent kinetics observed experimentally and capture the observed trends with respect to particle size and distribution. Monodisperse particles exhibited faster rates of redispersion compared to log-normally distributed Pd particles because the largest particles in the tail of the distribution require the longest time to disintegrate to monomers.

We conclude that gas phase conditions, initial Pd nanoparticle sizes, and particle

size distributions (ND vs. LND), influence the critical thermodynamic and kinetic factors that govern Pd redispersion to ion-exchanged Pd^{2+} sites, which are the desired precursor Pd structures for PNA, Wacker oxidation, and other applications. More broadly, we show that low-temperature (<900 K) Pd redispersion does not occur through gas-phase intermediates, but rather a surface-mediated OR process in the presence of atom trapping sites, as recently suggested by Datye and coworkers for noble metals on ceria supports.[180] Our results suggest that at low temperatures (<900 K), similar processes may govern the redispersion of Pd nanoparticles on other oxide supports; thus, the non-mean field nature of diffusion on the support and the spatial distribution of particles and atom or ion trapping sites are important factors to consider in strategies to enhance or suppress the rate of redispersion of Pd and PdO particles into site-isolated cations.

Acknowledgements

The authors acknowledge the financial support from the Department of Energy, Energy Efficiency and Renewable Energy (DE-EE0008213) for the experimental work at Purdue (R.G., T.M.L., H.L., and B.K.B.) and from the NSF under Cooperative Agreement EEC-1647722 and the Engineering Research Center for the Innovative and Strategic Transformation of Alkane Resources (CISTAR) for the Pd nanoparticle synthesis and characterization work at Purdue (C.L. and V.Y.). The authors also acknowledge the UVA Engineering Research and Innovation Award (K.M. and C.P.) and the Double Hoo Research Grant (K.M.) for financial support throughout the development of this project and the National Science Foundation Faculty Early Career

Development Program under award number 2144174-CBET (C.P.). The authors acknowledge Research Computing at the University of Virginia for the computational resources and technical support and Prof. Robert J. Davis and William S. Epling for helpful technical discussions. Additionally, the Purdue co-authors thank Dr. Xinyi Wei (BASF Corporation) for providing the CHA material and all other members of the collaborative research team from the University of Kentucky, University of California Berkeley, Ford Motor Company, Oak Ridge National Laboratory, and BASF for helpful technical discussions.

Chapter 4

Effect of Reaction Conditions and SO_2 Exposure on Cu Speciation in SSZ-13 Zeolites

This chapter is part of a current paper in preparation (Mandal, K.; Chen, Y. R.; Wijerathne, A; Nam, K.; Brezicki, G.; Kiani, D. A.; Davis, R. J.; Daya, R.; Epling, W. S.; and Paolucci, C. Effect of Reaction Conditions and SO_2 Exposure on Cu Speciation in SSZ-13 Zeolites, *In Preparation*). Here, we use a combined computational and experimental approach, using DFT calculations, and thermodynamic analysis, along with SCR rate measurements, CO titration, and UV-vis spectroscoscopy, to investigate the effect of high-temperature sulfur exposure on dimeric Cu species in CHA zeolites, and its impact on SCR performance. The scope of this chapter has been limited to my contributions to the study, which involve DFT calculations and AIMD simulations of monatomic and dimeric Cu species at different Al configurations, functional sensitivity analysis, and development of the thermodynamic model for predicting the stability of Cu cationic species as a function of reaction conditions (before and after sulfur exposure) and Al configurations in the zeolite. While some of the experimental evidence will be referred to for comparison with our theoretical results, complete methodology, and detailed results of the experimental and spec-

troscopic analyses can be found in Yu-ren Chen's doctoral dissertation (Chen, Y.R. Chapter 3: Probing Cu Dimers before and after Sulfur Poisoning, *Degradation Study of Cu-SSZ-13 Selective Catalytic Reduction Catalysts*, Charlottesville, VA: University of Virginia, Chemical Engineering - School of Engineering and Applied Science, PHD (Doctor of Philosophy), **2023**, doi.org/10.18130/kp67-3d37.

4.1 Introduction

Stringent exhaust emission control regulations have become the norm worldwide, and are expected to become even more rigorous in the future, especially those pertaining to nitrogen oxides (NO_x) emissions from diesel engines.[281–283] Selective catalytic reduction (SCR) of NO_x to nitrogen, employing ammonia (NH_3) as a reductant, has been successfully implemented in automotive applications, with small-pore zeolites, such as chabazite (CHA), exchanged with copper (Cu/SSZ-13) emerging as the most widely used commercial NH_3-SCR catalyst.[283–286] Cu/CHA catalysts exhibit high selectivity and hydrothermal stability, and possess a wide range of operation temperatures (473-873 K), which are well suited for heavy-duty diesel vehicles typically operating between 473-673 K.[287–289] However, Cu/CHA catalysts are susceptible to sulfur poisoning, with severe reduction in activity reported in the presence of even ppm levels of SO_2 at low temperatures (<573 K),[22,216,290–293] thereby limiting the application of Cu/CHA for NH_3-SCR of ultralow-sulfur diesel feeds. Despite the use of ultralow-sulfur diesel fuel in places like the EU and US where the maximum permissible limit of sulfur content is 10 and 15 wt.-ppm, respectively, sulfur can accumulate over the long lifetime of a diesel vehicle, increasing the amount of sulfur exposure of the aftertreatment system.[28,31,216] Moreover, diesel fuel with much higher sulfur

content are still used in many countries, and applications such as marine transport typically utilize high-sulfur fuels.[31] Another common source of sulfur in the diesel engines is the lubricating oil which contains about 0.3–0.7 wt% of sulfur.[31] While the majority of the sulfur present in the fuel and lube oil in a diesel engine is combusted to produce SO_2 in the exhaust, the diesel oxidation catalyst (DOC) present in the aftertreatment system can oxidize SO_2 to SO_3, which can react with water vapor to form H_2SO_4, thus exposing the NH_3-SCR Cu/CHA catalyst present downstream of a DOC to a mixture of SOx (x = 2–3) and H_2SO_4.[28,31]

The impact of sulfur exposure on Cu/CHA catalysts, especially its role in catalyst deactivation, and catalyst regeneration via high-temperature deSOx treatments (773–848 K), have been widely studied in literature.[22–25,27–31,291,292,294–296] Experimental and theoretical results have revealed the influence of a number of factors affecting catalyst deactivation with SOx exposure, such as the sulfur speciation (SO_2/ SO_3) and concentration, exposure temperature and reaction environment (presence or absence of H_2O and NH_3), zeolite composition (Cu/Al, Si/Al) and the Cu cation speciation in the zeolite (Cu^{2+} or $[CuOH]^+$).[22,24–31] SO_3 exposure, compared to SO_2, was reported to deactivate Cu-zeolite more severely, leading to a reduction in low-temperature SCR activity; using spectroscopic techniques such as X-ray photoelectron spectroscopy (XPS) and X-ray absorption fine structure (XAFS), Cheng et al. found that the Cu/zeolite sample sulfated with SO_3 remained highly dispersed in the form of $[CuSO_4]^+$, and contained larger amounts of sulfur, compared to the sample treated with SO_2.[296] Moreover, the presence of NH_3 in the exposure environment in the low-temperature regime enables desulfation of Cu/CHA at lower temperatures (∼673 K)[23,28] due to the formation of ammonium sulfate $(NH_4)_2SO_4$, which as observed in the TPD profile of Cu/CHA exposed to SO_2 at 473 K SCR conditions, desorbed at

a much lower temperature of 733 K in comparison to 943 K that was assigned to the decomposition of $CuSO_4$; contrarily, TPD profile of SO_2 exposure at 673 K yielded only the high-temperature $CuSO_4$ peak.[22]

In addition to the formation of $(NH_4)_2SO_4$ that can deactivate the catalyst by blocking the catalyst pores,[22] SOx can also interact with a variety of Cu cationic intermediates that are generated during the NH_3-SCR cycle at low temperatures, and poison the Cu active sites. Cu^{2+} and $(CuOH)^+$ are the predominant ion-exchanged species in CHA, charge compensating two Al- (represented as 'Z_2') and one Al- ('Z') exchange sites, respectively, with each active site having a different response to SOx exposure. Using diffuse reflectance infrared Fourier transform spectroscopy (DRIFTS), Luo et al.[27] compared NH_3 adsorption on fresh and sulfated SSZ-13 catalysts containing a distribution of Cu^{2+} and $(CuOH)^+$ sites, and found that while there was a reduction in NH_3 adsorption on both the active sites post sulfur exposure, the zeolitic framework vibrational feature associated with $(CuOH)^+$ disappeared completely on sulfur exposure, compared to that of Cu^{2+} which decreased to a smaller extent. This suggested that sulfur binds more strongly to ZCuOH sites than Z_2Cu, which has also been further supported by DFT calculations and thermodynamic analyses, reporting that formation of $CuHSOx$ (x = 3–4) species on ZCuOH sites is more exothermic than that on Z_2Cu, and are hence, possess higher thermodynamic stability at high temperatures.[24,25,297] Moreover, Z_2Cu and ZCuOH sites are completely solvated by NH_3 during low-temperature SCR conditions, forming mobile $[Cu^+(NH_3)_2]^+$ complexes, a pair of which can be further activated by O_2 at ~473K to form a peroxo Cu species $[(NH_3)_2Cu^{2+}\text{-}O\text{-}Cu^{2+}(NH_3)_2]^{2+}$.[18–21] The reactivity of these intermediates towards SO_2 has been recently studied using X-ray absorption spectroscopy,[30] and DFT calculations,[26] which have reported that SO_2 reacts exother-

mically with $[Cu_2{}^{2+}(NH_3)_4O_2]^{2+}$, reducing Cu^{2+} to Cu^+, and forms $SO_4(NH_4)_2$ and $HSO_4(NH_4)$ in the presence of NH_3 during low temperature SCR. At these reaction conditions, $HSO_4(NH_4)$ is thermodynamically stable, and hinder the inter-cage diffusion of $[Cu^+(NH_3)_2]^+$, causing sulfur accumulation in Cu/CHA.[26] The general consensus in literature for sulfur poisoning of Cu/CHA at temperatures <623 K is that the two different monatomic Cu sites Z_2Cu and ZCuOH have distinct interactions with sulfur, which dictate the deSO_x protocols in these materials. However, less is known about the validity of these findings for the interaction of SO_x with Cu active sites in CHA following sulfur exposure at high temperatures, especially since there is evidence from zeolite-catalyzed oxidation reactions in the literature that ion-exchanged Cu^{2+} can transform from monatomic to multinuclear species under high-temperature oxidizing conditions.

High-temperature (> 573 K) oxidative activation of Cu/zeolites to form Cu dimers ($Cu_2O_xH_y$) as the active sites for applications such as low-temperature methane-to-methanol conversion,[298–308] partial methane oxidation,[309,310] oxidation of NO to NO_2,[311,312] etc…has been widely studied using various experimental and spectroscopic techniques as well as theoretical calculations. These studies have highlighted the role of the zeolite composition (Si/Al and Cu/Al ratios) as well as the reaction environment in the site density as well as speciation of Cu dimers. Cu/SSZ-13 samples with a higher concentration of Z_2Cu sites (Si/Al = 5) were found to be inactive for methanol formation, while the samples with higher Si/Al ratio (∼12-15) and high Cu loadings (∼0.5) yielded significantly higher methane to methanol conversion due to a higher distribution of ZCuOH.[301,303,313] Solvated, mobile ZCuOH complexes have been hypothesized to act as the precursors for the formation of $Cu_2O_xH_y$ species, whereby two solvated ZCuOH sites with a nearby Al pair can dimerize during dehydration at

high temperatures.[301,303,313,314] This proposed mechanism underscores the importance of proximal ZCuOH sites for the formation of Cu dimers, since ZCuOH sites too far away would prefer to remain as monatomic Cu, indicating that knowledge of the local Al distribution in the zeolite (a consequence of the synthesis route) and Cu speciation at different Al ensembles is essential in the estimation of the dimeric Cu speciation and distribution.

Here, we used computational techniques and SCR rate experiments to study the Cu cation speciation and Cu dimer formation as a function of the Al distribution in CHA zeolite and the reaction conditions (P_{H_2O}, P_{O_2}), and investigate the effect of high-temperature (> 673 K) sulfur exposure on Cu dimers, and the subsequent effect on the SCR activity of the CHA zeolite. We show, that consistent with previously reported studies, the Al configurations in CHA dictate the Cu speciation, with formation of Cu dimers thermodynamically feasible only at certain Al-Al pair arrangements. Compared to monatomic Cu, dimeric Cu species exhibit stronger binding to sulfur species ($\sim$870 K) in the absence of NH_3 coverage, resulting in a significant loss of available Cu active sites, and a decrease in SCR activity.

4.2 Methods

4.2.1 Details of DFT and AIMD Calculations

We performed plane-wave, periodic DFT calculations on a 36 T-site tetrahedral SSZ-13 supercell obtained from the international zeolite association (IZA) database[88] using the Vienna ab initio simulation package (VASP, version 5.4.4).[146] We used an energy cutoff of 400 eV, and the projector augmented wave (PAW) method for core-valence

interactions,[154] and sampled the first Brillouin zone using only the Γ point due to the large supercell and insulating properties of the zeolitic system. Using previously reported monatomic and dimeric Cu species as a reference,[24,25,94,301,305,314,315] we considered multiple initial guesses for the hydroxylated and sulfated monatomic and dimeric Cu species anchored to the zeolitic framework, and carried out spin-polarized geometry optimizations with the convergence criteria for self-consistent field (SCF) electronic energies and atomic forces set to 10^{-6} eV and 0.03 eV/Å, respectively, using the Perdew-Becke-Erzenhof (PBE)[147] generalized gradient approximation (GGA) functional with the Becke-Johnson damping (D3(BJ)-vdw) dispersion correction method.[148,149] The lowest energy structures were further optimized with the Strongly Constrained and Appropriately Normed (SCAN)[316] meta-GGA functional with D3(BJ)-vdw dispersion corrections and the same energy and force convergence criteria as stated earlier. We tested the functional sensitivity for the energy calculations of the hydroxylation Cu species, and did not find appreciable difference in energies across functionals. We selected SCAN-D3(BJ)vdw computed values since it was the functional consistent for both the hydroxylation and sulfation energies (discussed in section 4.2.4)

To consider various local minima of the H_2O-solvated monatomic Cu structures, we performed spin-polarized ab initio molecular dynamics (AIMD) simulations using VASP, version 5.4.4 by constructing initial guesses based on similar structures reported previously.[24,94] Due to the large size of the supercell considered in our calculations, we ran simulations of 30 ps with 0.5 fs time steps at 473 K using the GGA-PBE-D3(BJ)vdw functional. Next, we sampled the five lowest energy structures, and optimized them using the GGA-PBE-D3(BJ)vdw functional. The energy of the lowest energy structure so obtained was further optimized using SCAN-D3(BJ)vdw.

4.2.2 Details of Ab Initio Formation Free Energy Calculations

We calculated the formation free energies of hydroxylated ($Z_*Cu_{1,2}O_xH_y$) and sulfated ($Z_*Cu_{1,2}O_xH_yS_z$) monatomic and dimeric Cu species using O_2, H_2O, and SO_2 as references:[161]

$$\Delta G^{\text{form}}_{Z_*Cu_{1,2}O_xH_y}(T, \Delta\mu_{O_2}, \Delta\mu_{H_2O}) = \Delta E^{\text{form}}_{Z_*Cu_{1,2}O_xH_y} - T\Delta S^{ST}_{Z_*Cu_{1,2}O_xH_y}(T) - \frac{x}{2}\Delta\mu_{O_2} - \frac{y}{2}\left(\Delta\mu_{H_2O} - \frac{1}{2}\Delta\mu_{O_2}\right) \quad (4.1)$$

$$\Delta G^{\text{form}}_{Z_*Cu_{1,2}O_xH_yS_z}(T, \Delta\mu_{O_2}, \Delta\mu_{H_2O}, \Delta\mu_{SO_2}) = \Delta E^{\text{form}}_{Z_*Cu_{1,2}O_xH_yS_z} - T\Delta S^{ST}_{Z_*Cu_{1,2}O_xH_yS_z}(T) - \frac{x}{2}\Delta\mu_{O_2} - \frac{y}{2}\left(\Delta\mu_{H_2O} - \frac{1}{2}\Delta\mu_{O_2}\right) - \frac{z}{2}\Delta\mu_{SO_2} \quad (4.2)$$

$$\Delta E^{\text{form}}_{Z_*Cu_{1,2}O_xH_y} = E_{Z_*Cu_{1,2}O_xH_y} - E_{\text{reference}} - \frac{x}{2}E_{O_2} - \frac{y}{2}\left(E_{H_2O} - \frac{1}{2}E_{O_2}\right) \quad (4.3)$$

$$\Delta E^{\text{form}}_{Z_*Cu_{1,2}O_xH_yS_z} = E_{Z_*Cu_{1,2}O_xH_yS_z} - E_{\text{reference}} - \frac{x}{2}E_{O_2} - \frac{y}{2}\left(E_{H_2O} - \frac{1}{2}E_{O_2}\right) - \frac{z}{2}E_{SO_2} \quad (4.4)$$

where $E_{\text{reference}}$ is the species considered as the zero of energy, and Z_* represents one Al ('Z') and two Al ('Z_2') exchange sites.

We used the ideal gas law to calculate the difference in the chemical potential of species ($\Delta\mu = \mu - \mu^\circ$) between 0 K ($\mu^\circ$) and reaction conditions (μ (P,T)) as per:

$$\mu\ (P,T) = \ \mu^{\circ} + \mathrm{RT}\ln\left(\frac{P}{P^{\circ}}\right) \tag{4.5}$$

where P° is the pressure at standard state = 1 atm. We used values listed in the NIST-JANAF database[317] for calculation of chemical potential of the gaseous species (O_2, H_2O and SO_2).

The difference in the translational entropy between a H_2O-solvated and clean site (ΔS^{ST}) is evaluated using an empirical approximation based on the Sacker-Tetrode equation, and validated via potential of mean force AIMD simulations, with the underlying assumption that the translational entropy of the adsorbate is two-thirds that of its gas phase:

$$\begin{aligned}\Delta S^{\mathrm{ST}}_{\mathrm{Z_*Cu_{1,2}O_xH_y}} &= \left(S_{\mathrm{Z_*Cu_{1,2}O_xH_y}} - S_{\text{clean site}}\right) \\ &\approx \frac{2}{3}\ k_B \ln\left[\left(\frac{2\pi M_{x,y} k_B T}{h^2}\right)^{\frac{3}{2}}\ \left(\frac{k_B T}{P^{\circ}}\right)\frac{e^{\frac{5}{2}}}{N_A}\right]\end{aligned} \tag{4.6}$$

$M_{x,y}$ is the mass of the adsorbate. The empirical correlation for calculation of ΔS^{ST} was applied only to the solvated Cu complexes. Additionally, we have ignored zero point energy (ZPE) effects and vibrational entropy contributions in our analysis because the ΔZPE and ΔS_{vib} values are expected to be negligible for this system.

4.2.3 Details of Structure Generation

To generate the initial Z_2Cu, Z_2H_2, and dimer (ZCuOCuZ, $ZCuO_2CuZ$) structures, the pure silica form of the CHA supercell obtained from the international zeolite association (IZA) database[88] was used. We generated all possible two Al configurations

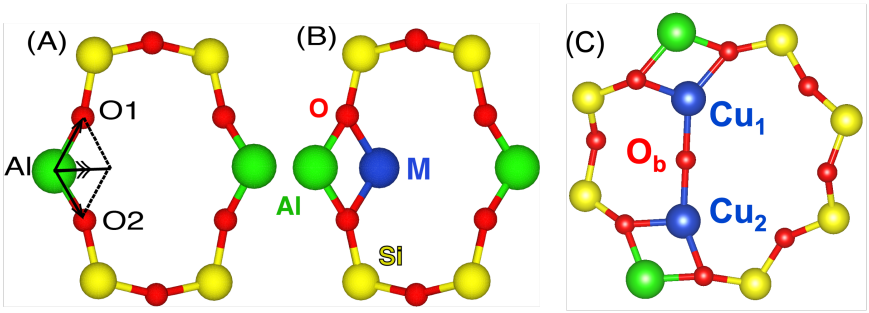

Figure 4.1: Initial geometry generation: (a)vector addition method (b) Z_2Cu geometry, and (c) ZCuOCuZ dimer generated from vector addition method.

(Z_2) < 11 Å distance. Löwenstein's rule demonstrates that the Al-O-Al bond formation is unlikely to be observed in zeolites, and therefore Z_2 configurations with Al-O-Al were removed. We used a connectivity-based graph isomorphism test using the python NetworkX code[318] to determine crystallographically unique 2Al configurations. The isomorphism test significantly reduces the number of generated configurations; for example, in CHA, we initially generated 630 Al configurations; however, only 25 were unique in terms of connectivity. Then the metal ion is placed inside a zeolite ring using the vector equation:[319]

$$\mathbf{Al} - \mathbf{Cu} = (\mathbf{Al}{-}\mathbf{O}_1) + (\mathbf{Al}{-}\mathbf{O}_2) \tag{4.7}$$

The bold letters indicate each atom's position vectors and O_1 and O_2 are the oxygens bonded to one of the Al under consideration. As depicted in Figure 4a-b, this method places the ion inside a zeolite ring on the same plane generated by **Al-O$_1$** and **Al-O$_2$**. Once the Cu cation is placed in a zeolite ring, we performed another graph isomorphism test to remove structurally similar Z_2Cu structures. Similarly, for Z_2H_2 structure generation, we used the vector equation to place the H atom in the zeolite ring with an O-H distance of 0.97 Å.[319,320]

$$\mathbf{H-O} = \frac{(\mathbf{O-T}_1) + (\mathbf{O-T}_2)}{|(\mathbf{O-T}_1) + (\mathbf{O-T}_2)|} \times 0.97 \tag{4.8}$$

Using the vector addition method, we generated the initial structures of ZCuOCuZ dimers by placing two Cu atoms in zeolite rings. Subsequently, bridging oxygen (O_b) is placed between two Cu ions in the midpoint (**Figure 4.1c**). From previous DFT calculations, the reported Cu-O_b distance is 1.70–1.78 Å.[314,321] Therefore, initial structures with Cu-O_b < 1.0 Å or Cu-O_b > 2.5 Å were removed as they do not form dimeric structures. A similar vector addition procedure was used to generate $ZCuO_2CuZ$ dimers, in which O−O was added to the Cu-Cu bisection point instead of single O_b. The orientation of O-O in $ZCuO_2CuZ$ dimers were initially set perpendicular to the Cu-Cu vector in the same plane as Cu-Cu by using the vector cross product, and the O-O distance was kept at 1.5 Å to resemble the peroxide $ZCuO_2CuZ$ dimer species reported in the literature.

Following generation of the initial guess dimer structures at the remaining valid Al pair configurations, DFT geometry optimizations were performed using both the SCAN and PBE functionals. Hydroxlated dimer structures (ZCu(OH)CuZ, $ZCu(OH)_2CuZ$) were generated manually from the optimized ZCuOCuZ and $ZCuO_2CuZ$ structures.

4.2.4 Benchmarking Calculations for Bulk Copper Sulfate

To test the functional accuracy for sulfation energy calculations, we used the structures provided for O, bulk Cu, S, $CuSO_4$, and Cu_2SO_4 provided in the Open Quantum Materials Database (OQMD)[322,323] to compute the bulk formation energies of copper sulfates as:

$$Cu + 4O + S \rightarrow CuSO_4 \tag{4.9}$$

$$2Cu + 4O + S \rightarrow Cu_2SO_4 \tag{4.10}$$

We used the force and energy convergence criteria for geometry optimization as mentioned in the previously, and used the Monkhorst-Pack k-point mesh provided in OQMD for each crystal structure, to sample the first Brillouin zone. We considered GGA-PBE, PBE+U (a Hubbard+U parameter of 6 eV was applied for Cu 3d electrons),[324] and SCAN functionals, with D3(BJ) dispersion correction, to calculate the formation energies of bulk $CuSO_4$, and Cu_2SO_4, and compared them to their experimental energies of formation reported in OQMD.

4.3 Results

4.3.1 Influence of Al Configuration on Cu Cation Speciation in SSZ-13 at High Temperatures

Results from spectroscopic evidence (DRIFTS, UV-vis, XPS, Raman, XRD, FTIR), experimental data from methane conversion, NO_x conversion during SCR,[22,27,29,301,303,313,314] along with DFT calculations[24,25,297] have demonstrated the unique behavior of ion-exchanged monatomic (Z_2Cu and ZCuOH) and multinuclear (Cu_xO_y) Cu sites in CHA. ZCuOH sites are suggested to be precursors for the formation of Cu dimers during high temperature oxidizing treatments, and displayed a greater susceptibility to low-temperature sulfur poisoning, compared to Z_2Cu. The site distribution of Z_2Cu and ZCuOH is dependent on the Si/Al ratio, Cu loading, and the syntheses protocols, which influences the local Al distribution in the zeolite. Hence, we need to first understand the Cu speciation in CHA as a function of the Al configurations, and the

reaction conditions, to then, subsequently investigate the effect of high-temperature sulfur exposure ($>$ 673 K).

We created a computational model using a 36 T-site supercell of a CHA type framework SSZ13 zeolite made up of 4, 6, and 8 member rings (MR) (**Figure 4.2a**). Monoatomic Cu species, [Z_2Cu^{II}] and [$ZCu^{II}OH$], formed at 2Al and 1Al exchange sites, respectively,[24,94,314] from the ion-exchange of a single Cu cation have been shown in **Figure 4.2b** ('Z' enclosed in brackets denotes that the Cu cation and its ligands are attached to the zeolite framework). Ion-exchanged Cu is fully solvated by H_2O (or NH_3 at SCR conditions[19,20,37,94]) forming $Z_2[Cu(H_2O)_4]$ and $Z[Cu(OH)(H_2O)_3]$ at the 1Al and 2Al sites, respectively, at ambient conditions.[37,94] However, at high temperatures, several experimental and computational studies for methane-to-methanol conversion, partial methane oxidation, NO oxidation in dry conditions,[301,303,306,313,315] have reported the formation of dimeric Cu species [$Z_2Cu_2O_xH_y$] (x =1-2, y =1-2) (**Figure 4.2b**) from hydrated $[Cu(OH)]^+$ species located at proximal Al exchange sites. Depending on the arrangement of the Al sites, [$Z_2Cu_2O_xH_y$] species can be formed at the 2Al sites present in the same 8 MR as well as between two 1Al sites present in separate MRs in a '*bridged*' configuration.

To analyze the influence of Al-Al pair proximity on the Cu speciation at high temperatures in an oxidizing environment, we considered three different example Al configurations (shown in **Figure 4.2c-e**) in the 36 T-site SSZ-13 supercell, and evaluated the formation of monatomic and dimeric Cu species from H_2O-solvated monatomic Cu species ($Z_2[Cu(H_2O)_4]$ and $Z[Cu(OH)(H_2O)_3]$) at each of the three Al-Al configurations as per the following eqs:

$$Z_2\left[Cu\left(H_2O\right)_4\right] \ / \ Z\left[CuOH\left(H_2O\right)_3\right] \rightarrow [Z_2Cu] \ / \ [ZCuOH] + 7H_2O \tag{4.11}$$

$$\mathrm{Z_2\,[Cu\,(H_2O)_4]\ /\ Z\,[CuOH\,(H_2O)_3] \rightarrow [Z_2Cu_2O_xH_y]\ /\ [ZH] + \left(4-\frac{x}{2}\right)O_2 + \left(7-\frac{y}{2}\right)\left(H_2O-\frac{1}{2}O_2\right)} \quad (4.12)$$

$$\mathrm{Z\,[CuOH\,(H_2O)_3]\ /\ Z\,[CuOH\,(H_2O)_3] \rightarrow [ZCuOH]\ /\ [ZCuOH] + 6H_2O} \quad (4.13)$$

$$\mathrm{Z\,[CuOH\,(H_2O)_3]\ /\ Z\,[CuOH\,(H_2O)_3] \rightarrow [Z_2Cu_2O_xH_y] + \left(4-\frac{x}{2}\right)O_2 + \left(7-\frac{y}{2}\right)\left(H_2O-\frac{1}{2}O_2\right)} \quad (4.14)$$

where x =1–2, and y =1–2. The forward slash represents Z_2 or Z exchange sites in separate zeolite cages.

Configuration 1 as shown in **Figure 4.2c** comprises of H_2O-solvated Z_2Cu charge-compensating Al-Al pair present in the same 6MR at a distance of 5.8 Å. To maintain the Cu stoichiometry in the formation of dimeric Cu from H_2O-solvated Z_2Cu as shown in eq 4.9, an additional 1Al exchange site was added in a separate cage in the same 36 T-site supercell, which is charge compensated by H_2O-solvated ZCuOH. Configuration 2 (**Figure 4.2b**) and 3 (**Figure 4.2c**) have two isolated 1Al sites 10.4 Å and 7.4 Å apart, respectively, each site being charge compensated by $Z[CuOH\,(H_2O)_3]$. We computed the exchange reaction energies for monatomic and dimeric Cu species as per eqs 4.11-4.14 using the SCAN functional with the Becke-Johnson damping method (D3-(BJ)vdw) for dispersion corrections (full details are in Section 4.2.1). Subsequently, we used the SCAN-D3(BJ)vdw computed exchange energies and thermodynamic correlations detailed in Section 4.2.2 to evaluate the Gibbs formation free energy (ΔG^{form}), and constructed a thermodynamic phase diagram for each of the three Al-Al configurations (**Figure 4.2c-e**) at 10% O_2 and varying degrees of

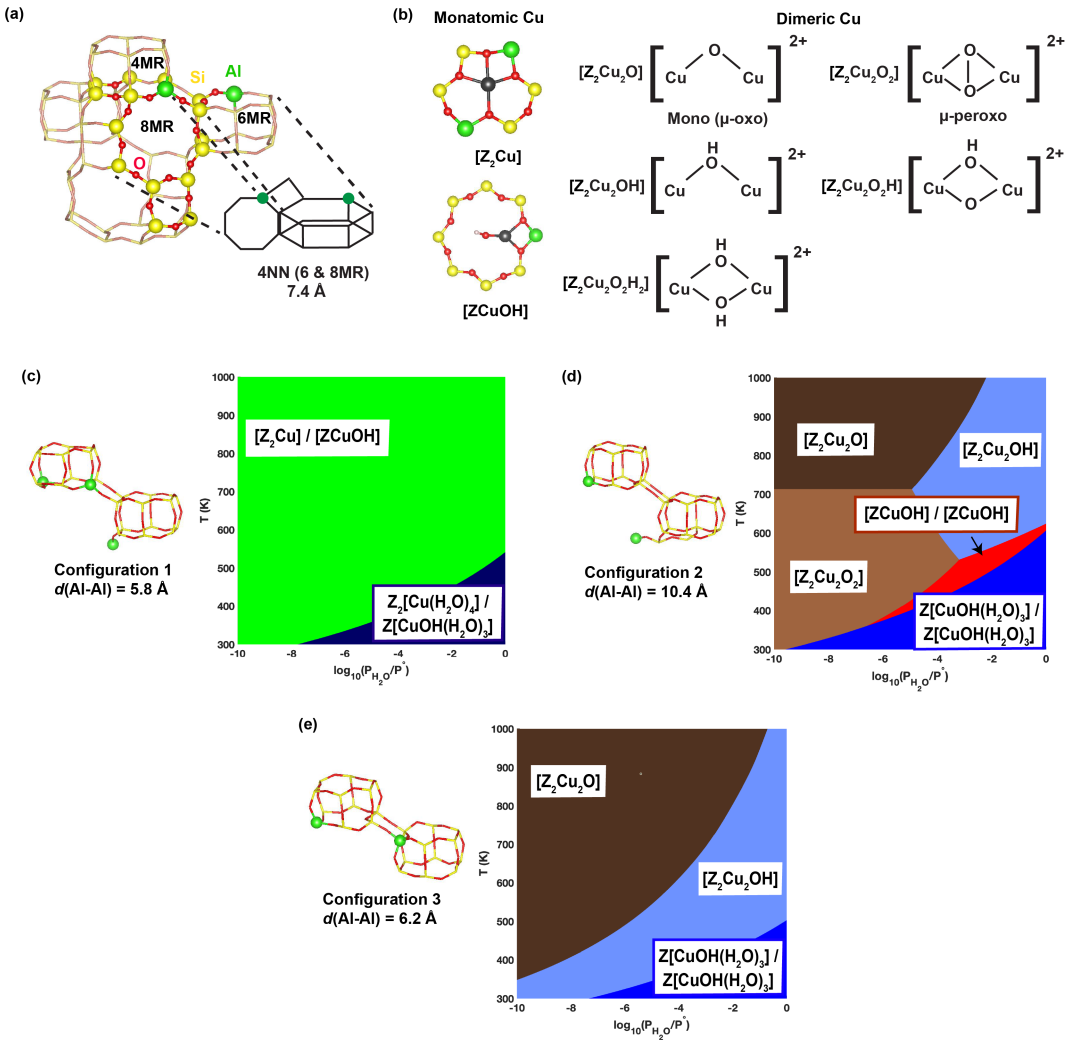

Figure 4.2: (a) Framework of SSZ-13 zeolite comprising of four-, six-, and eight membered rings (MR), and a simplified representation of an example Al-Al configuration (NN represents nearest neighors), (b) Optimized structures of monatomic and dimeric Cu species. Thermodynamic phase diagrams for example Al-Al configurations where (c) Al-Al pair is present in the same 6MR at a distance of 5.8 Å (configuration 1), preferentially forming [Z_2Cu], (d) two isolated Al exchange sites present at a distance of 10.4 Å (configuration 2), forming isolated [ZCuOH] and dimeric Cu species, and (e) Al-Al pair is present in separate rings (6 and 4MR) at a distance of 6.2 Å, thermodynamically favoring formation of dimeric Cu. The energies values of all the species considered in the phase diagrams has been provided in Table A.1, Appendix A.

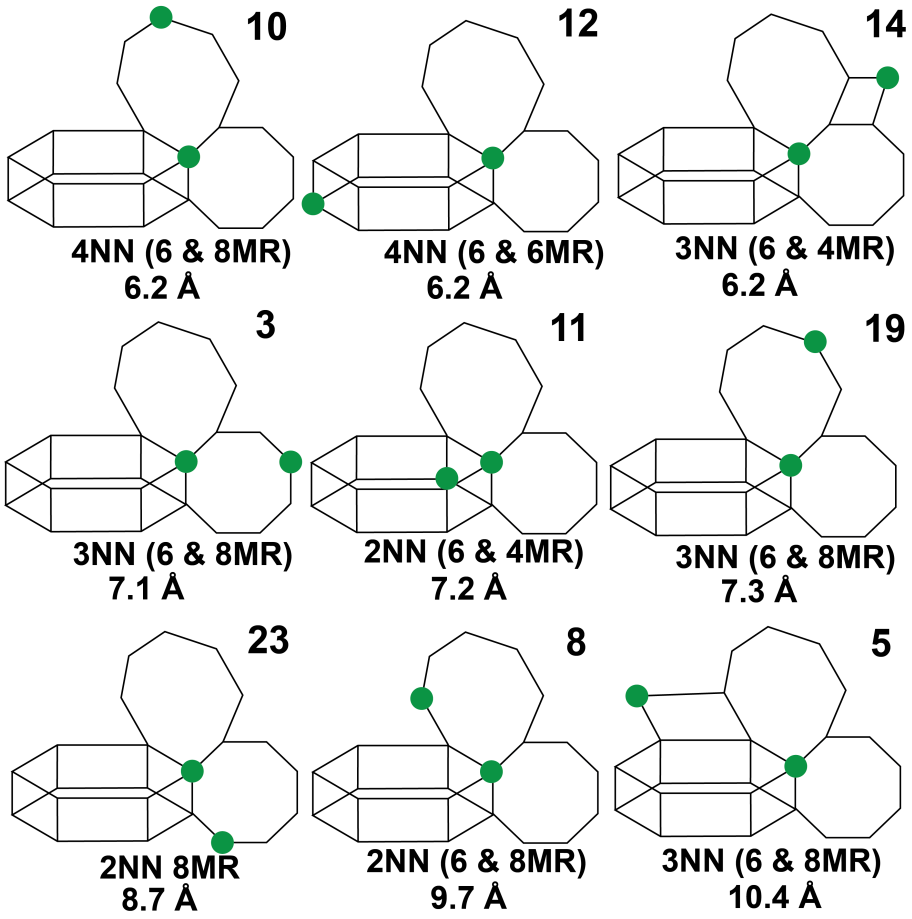

Figure 4.3: 9 Al-Al configurations forming dimeric Cu ($[Z_2Cu_2O_xH_y]$) species out of the 25 plausible 2Al configurations in 36 T-site SSZ-13 supercell. The configuration number has been shown at the top right corner of each configuration, and the configurations have been arranged in ascending order of Al-Al distance in Å. Configuration 3 from Figure 4.2e corresponds to the configuration 14 in this numbering sequence.

H_2O pressures (-5 < $\log(P_{H_2O}/P^\circ)$ < 5) and temperatures(300 K< T <1000 K). Free energies for all species are tabulated in A.1. As the temperature increases, the competition between formation of monatomic vs dimeric Cu species from H_2O-solvated monatomic Cu is dictated by the arrangement of the Al-Al pair. At 473 K, 10% O_2, 7% H_2O, configuration 1 (**Figure 4.2c**) preferentially formed monatomic Cu ($[Z_2Cu]$/[ZCuOH]), and configuration 2 (**Figure 4.2d**) remained as isolated [ZCuOH] species, respectively, post desorption of H_2O molecules; however, with further increase in temperature, the isolated [ZCuOH] sites form dimeric Cu ($[Z_2Cu_2OH]$ and ($[Z_2Cu_2O]$) species. Conversely, dimeric Cu ($[Z_2Cu_2OH]$ and ($[Z_2Cu_2O]$) species are preferred over monatomic Cu at temperatures > 450 K at configuration 3 (**Figure 4.2e**), showing that the formation of dimeric Cu species from H_2O-solvated [ZCuOH] is thermodynamically favorable only at certain Al-Al configurations.

Next, to identify the Al-Al pairs that preferentially form Cu dimers instead of monatomic Cu, we examined all 25 unique 2Al configurations plausible in a 36T site SSZ-13 supercell[89] (shown in Figure A.1 in Appendix A). First, we eliminated the Al-Al pairs violating Löwenstein's rule (no Al-O-Al), and applied an automated dimer generation model detailed in section 4.2.3, to the remaining 21 2Al configurations to evaluate the thermodynamic feasibility of formation of dimeric Cu by using probe reactions of mono μ-oxo Cu dimer ($[Z_2Cu_2O]$) and peroxo dimer ($[ZCuO_2CuZ]$) formation. We compared the PBE-D3-BJ(vdw) computed dimer formation energies to that of monatomic Cu ($[Z_2Cu]$, [ZCuOH]) at each of the 21 2Al configurations to identify 9 Al-Al configurations that preferentially formed dimers, shown in **Figure 4.3**. Göltl and coworkers[305,306] have also reported a subset of these 9 2Al pairs forming Cu dimers (configurations 10, 3, and 11 in **Figure 4.3**).

Subsequently, we considered the formation of various dimeric Cu motifs $[Z_2Cu_2O_xH_y]$

as illustrated in **Figure 4.2b**, at the 9 2Al configurations, and evaluated their thermodynamic stability of at a variety of reaction conditions by using SCAN-D3(BJ)vdw functional to compute their formation energies relative to [Z_2Cu_2O] as per:

$$[Z_2Cu_2O] + \left(\frac{1-x}{2}\right) O_2 + \left(\frac{y}{2}\right)\left(H_2O - \frac{1}{2}O_2\right) \rightarrow [Z_2Cu_2O_xH_y] \tag{4.15}$$

where x =1–2, and y =1–2.

Using the SCAN-D3(BJ)vdw computed energies, we calculated their formation free energies (ΔG^{form}) as per the thermodynamic correlations detailed in Section 4.2.2 to generate thermodynamic phase diagrams for each of the 9 2Al configurations by plotting $\Delta G^{\text{form}}(T, P_{H_2O}, P_{O_2})$ at fixed P_{O_2}= 10%, and over varying conditions of H_2O pressures (-5 < $\log(P_{H_2O}/P^{\circ})$ < 5) and temperatures (500 K< T <1000 K) (Figure A.2, Appendix A). At conditions of high temperature O_2 activation (698 K, 7% H_2O, 10% O_2), which are relevant for applications such as NOx SCR in diesel engines, methane-to-methanol conversion, etc…[301,303,306,313,315] we observed a distribution of [Z_2Cu_2O], [$Z_2Cu_2O_2$], [Z_2Cu_2OH], and [$Z_2Cu_2O_2H_2$] species to be thermodynamically stable, with the hydroxylated dimers as the predominant species at 698 K. Similar thermodynamic analyses performed by Göltl et al.[305] for a subset of these Al-Al configurations (configurations 10, 3, and 11 in **Figure 4.3**) found [Z_2Cu_2OH] and [$Z_2Cu_2O_2H_2$] to be the most thermodynamically stable species between 473-773 K. Details of the thermodynamically plausible dimeric Cu species at 698 K, 7% H_2O, 10% O_2 for each of the 9 2Al configurations have been listed in **Table 4.1**, with their formation energy being reported relative to [Z_2Cu_2O] (considered as zero of energy).

Table 4.1: Formation Free Energies in kJ mol^{-1} of Plausible Hydroxylated Cu Dimers [$Z_2Cu_2O_xH_y$] at 698 K, 7% H_2O, 10% O_2 Calculated Using SCAN-D3(BJ)vdw, at the 9 Identified Cu Dimer-forming Al-Al Pairs Reported in Figure 4.3.[a]

Plausible hydroxylated	2Al Configurations (Distance between Al-Al pair in Å)				
Cu dimers [$Z_2Cu_2O_xH_y$]	10 (6.2 Å)	12 (6.2 Å)	14 (6.2 Å)	3 (7.1 Å)	11 (7.2 Å)
[Z_2Cu_2O]	0	0	0	0	0
[$Z_2Cu_2O_2$]	+69	+40	+70	+100	+130
[$Z_2Cu_2O_2H$]	**-19**	-19	**-11**	**-19**	**-7**
[$Z_2Cu_2O_2H$]	+32	+37	+105	+76	+148
[$Z_2Cu_2O_2H_2$]	+3	**-28**	+84	+5	+54

Plausible hydroxylated	2Al Configurations (Distance between Al-Al pair in Å)			
Cu dimers [$Z_2Cu_2O_xH_y$]	19 (7.3 Å)	23 (8.7 Å)	8 (9.7 Å)	5 (10.4 Å)
[Z_2Cu_2O]	0	0	0	0
[$Z_2Cu_2O_2$]	+94	+127	+98	+50
[Z_2Cu_2OH]	-4	**-8**	**-20**	**-28**
[$Z_2Cu_2O_2H$]	+67	+98	+181	+159
[$Z_2Cu_2O_2H_2$]	**-8**	+8	+48	+80

[a] The formation free energies have been expressed relative to [Z_2Cu_2O]. The most thermodynamically stable species for each Al-Al configuration has been highlighted in bold.

4.3.2 Effect of Sulfur Exposure on Dimeric Cu Species

Next, we examined the effect of sulfur exposure (SO_2/SO_3) on the $[Z_2Cu_2O_xH_y]$ species at the 9 2Al configurations by calculating their sulfation reaction energies. While reaction energies of SO_2/SO_3 with Cu dimers in the absence of NH_3, have not been reported earlier, Jangjou et al.[25] and Shih et al.[24] performed DFT calculations for the sulfation of monatomic Cu species such as $[Z_2Cu]$ and [ZCuOH] resulting in the formation of Cu sulfite/sulfate ($[CuSO_{z=2\text{-}4}]^{2+}$) and bisulfite/bisulfate ($[CuHSO_{z\,=\,3,4}]^{+}$), respectively, demonstrating that monatomic Cu sulfation energies are exothermic (ranging from -42 to -143 kJ mol^{-1}).

To compare the sulfation energies of monatomic *vs* dimeric Cu species, first, we used a variety of functionals such as GGA-PBE, PBE+U, and SCAN, in conjunction with D3-(BJ)vdw dispersion correction, to compute the reaction energies of SO_2 and SO_3 with $[Z_2Cu_2O_x]$ (x =1–2) species at an example dimeric Cu-forming Al-Al configuration (configuration 5 in **Figure 4.3**) as per:

$$[Z_2Cu_2O] + SO_2 \rightarrow [Z_2Cu_2SO_3] \tag{4.16}$$

$$[Z_2Cu_2O] + SO_2 + \frac{1}{2}O_2 \rightarrow [Z_2Cu_2SO_4] \tag{4.17}$$

$$[Z_2Cu_2O_2] + SO_2 \rightarrow [Z_2Cu_2SO_4] \tag{4.18}$$

The SO_2/SO_3 reaction energies of dimeric Cu listed in **Table 4.2** are significantly more exothermic (ranging from -115 to -434 kJ mol^{-1}) than those reported for monatomic Cu,[24,25] signifying that SO_x binds much more strongly to Cu dimers. Additionally, the sulfation energies of Cu dimers exhibited a deviation of ∼57-80 kJ mol^{-1} for the reaction of SO_2/SO_3 with $[Z_2Cu_2O]$, and ∼170 kJ mol^{-1} for the reaction of SO_2 with

Table 4.2: Reaction Energies of SO_2/SO_3 with $[Z_2Cu_2O_x]$ (x =1-2) Calculated Using Different Functionals[a]

Reaction	Reaction Energies (in kJ mol^{-1})			
	PBE	PBE+U	HSE06	SCAN
$[Z_2Cu_2O] + SO_2 + \frac{1}{2}O_2 \rightarrow [Z_2Cu_2SO_4]$	-115	-152	-172	-155
$[Z_2Cu_2O] + SO_2 + \frac{1}{2}O_2 \rightarrow [Z_2Cu_2SO_4]$	-290	-331	-385	-354
$[Z_2Cu_2O_2] + SO_2 \rightarrow [Z_2Cu_2SO_4]$	-258	-348	- 434	-306

[a] D3(B)vdw dispersion correction has been applied to all the calculations

$[Z_2Cu_2O_2]$, demonstrating sensitivity to the functional employed. However, regardless of the functional used, we note that sulfur reaction energies with dimeric Cu are consistently highly exothermic and yield the same optimized structure for Cu sulfite $[Cu_2SO_3]^{2+}$ and sulfate $[Cu_2SO_4]^{2+}$. To determine which functional among the ones considered is the most accurate for the reaction of SO_2/SO_3 with Cu dimers, we next performed benchmarking calculations by computing the formation energies of bulk $CuSO_4$ and Cu_2SO_4 using GGA-PBE, PBE+U, and SCAN, with D3-(BJ)vdw dispersion correction; calculation details are in Section 4.2.4, and the formation energies have been reported in **Table 4.3**. Comparing the computed energies with the experimental energies of formation reported in previous studies,[325,326] we found good agreement with the SCAN-D3(BJ)vdw reaction energies.

Subsequently, we used SCAN-D3(BJ)vdw functional to compute the reaction energies of SO_2/SO_3 with hydroxylated Cu dimers $[Z_2Cu_2O_xH_y]$ at the example Al-Al configuration in **Figure 4.2e** as per:

$$[Z_2Cu_2OH] + SO_2 + \frac{1}{2}O_2 \rightarrow [Z_2Cu_2HSO_4] \tag{4.19}$$

Table 4.3: Details of the Benchmarking Calculations Performed for Formation Energies of Bulk Copper Sulfates

	Formation energy (in kJ mol^{-1} atom^{-1})			
	PBE (with D3-BJ vdw)	**PBE+U (with D3-BJ vdw)**	**SCAN (with D3-BJ vdw)**	**Experimental values**
$CuSO_4$	-110	-111	-136	-133[325]
Cu_2SO_4	-90	-101	-112	-113[326]

$$[Z_2Cu_2O_2H_2] + SO_2 \rightarrow [ZCu_2HSO_4]\,/[ZH] \tag{4.20}$$

We observe that sulfation of hydroxylated Cu dimer changes the formal oxidation state of Cu from +2 in $[Cu_2SO_4]^{2+}$ to +1.5 and +1 in $[Cu_2HSO_4]^{2+}$ and $[Cu_2HSO_4]^{+}$ as seen in eqs 4.19 and 4.20, respectively, suggesting that similar to the reaction of sulfur with peroxo Cu dimers in the presence of NH_3 ($[Cu_2{}^{2+}(NH_3)_4O_2]^{2+}$),[26,30] Cu dimers exposed to sulfur in the presence of H_2O may reduce the Cu^{2+} cation. We also computed sulfation of the monatomic Cu moieties ($[Z_2Cu]$ and [ZCuOH], and their H_2O-solvated counterparts), at the example Al-Al configurations in **Figure 4.2c-d**. Using the computed reaction energies and the thermodynamic correlations described in Section 4.2.2, we calculated $\Delta G^{\text{form}}(T, P_{H_2O}, P_{O_2}, P_{SO_2})$ for the formation of sulfated monatomic and dimeric Cu species, and constructed thermodynamic phase diagrams for a range of temperatures (300 K$< T <$1000 K) and H_2O pressures (-5 $<$ $\log(P_{H_2O}/P^{\circ}) < 5$) at 10% O_2 and 30 ppm SO_2, shown in **Figure 4.4a-c**. At low temperatures (473 K, 10% O_2, 30 ppm SO_2, 7% H_2O), analogous to previously reported calculations by Shih et al.,[24] we observed that SOx reacts with H_2O-solvated $[Z_2Cu]$

and [ZCuOH] forming a monatomic Cu complex containing two bisulfite $(HSO_4)^-$ ligands which is detached from the zeolite framework, at all the Al-Al configurations. At configuration 1 (**Figure 4.4a**), which preferentially formed [Z_2Cu] in the absence of sulfur exposure, increase in temperature results in the desorption of one bisulfite $(HSO_4)^-$ ligand, and we observe the formation [$ZH/ZCuSO_4$], suggesting sulfur could facilitate conversion of some Z_2Cu sites to ZCuOH (in specific 3Al ensembles). Subsequently, at T >600 K, sulfur desorbs from the Cu sites generating [Z_2Cu] back; we refer to the temperature at which sulfated Cu becomes the minority species as the desulfation temperature. At configuration 2 (**Figure 4.4b**), we observed the formation of two isolated [ZCuOH] sites at $T < 600$ K in the absence of sulfur exposure; reaction with SO_x lead to the formation of [$Cu(HSO_4)_2$] complexes which are detached from the zeolite framework, and at $T > 580$ K form sulfated Cu dimer [$Z_2Cu_2SO_4$]. Sulfur eventually desorbs from the Cu dimer at 800 K forming [Z_2Cu_2OH]. Similar behavior is observed at configuration 3 (**Figure 4.4c**) which thermodynamically favored formation of Cu dimers at $T > 450$ K when no SO_x was present; upon exposure to SO_x, sulfated monatomic Cu complexes transformed into sulfated Cu dimers at $T > 550$ K, with the sulfur binding strongly to the Cu dimer until 870 K. We observe that as temperatures increase, there is a thermodynamic driving force for desulfation of Cu dimers, with the desulfation temperatures dependent on the arrangement of the Al-Al pairs.

Next, we extended our thermodynamic model to all the Al-Al configurations in **Figure 4.3**, and computed the formation free energies of sulfated Cu dimers as a function of reaction conditions. The thermodynamic phase diagrams constructed for all the Al-Al configurations have been reported in Figure A.3, Appendix B; the formation free energies of the (bi)sulfite and (bi)sulfate Cu dimers relative to the

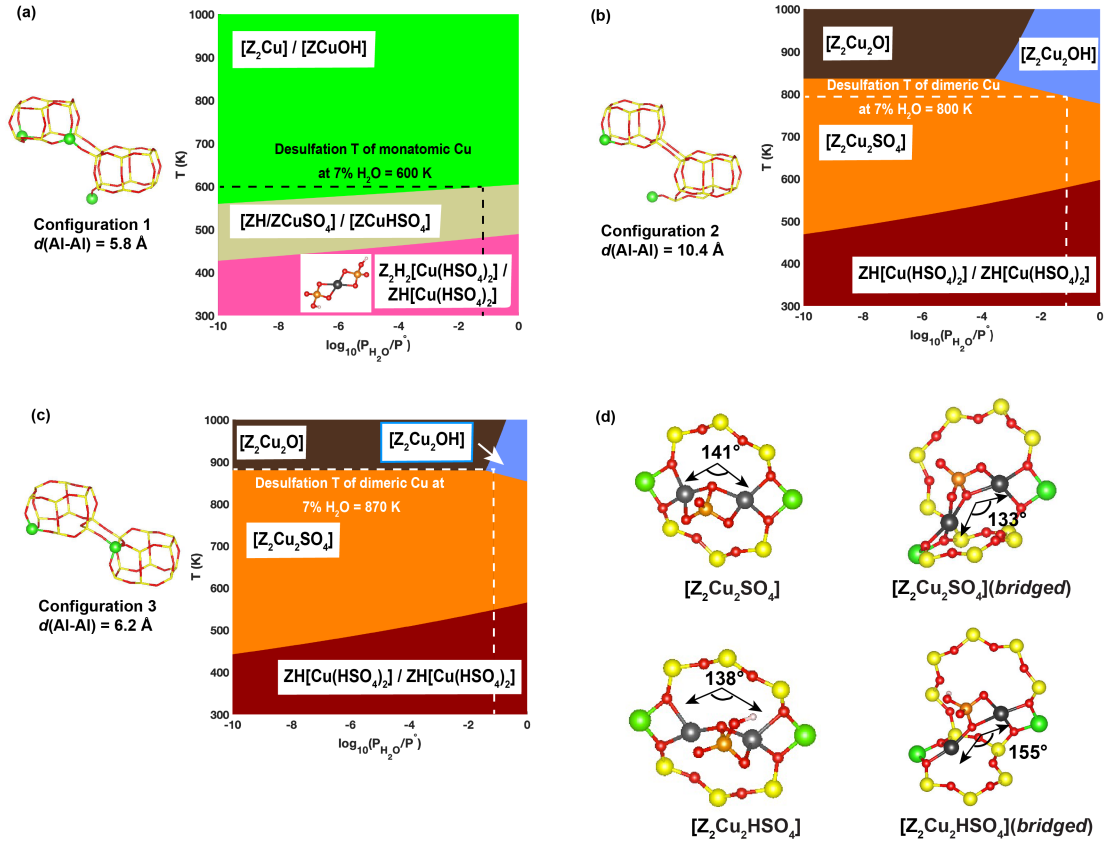

Figure 4.4: Thermodynamic phase diagram for sulfation of (a) Al-Al pair is present in the same 6MR at a distance of 5.8 Å (configuration 1), preferentially forming [Z_2Cu], (b) two isolated Al exchange sites present at a distance of 10.4 Å (configuration 2), forming isolated [ZCuOH] and dimeric Cu species, and (c) Al-Al pair is present in separate rings (6 and 4MR) at a distance of 6.2 Å, thermodynamically favoring formation of dimeric Cu, and (d) optimized geometries of representative structures of bisulfate and sulfate Cu dimers at Al-Al pairs present in the same 8MR, and at a '*bridged*' configuration, respectively. The energies values of all the species considered in the phase diagrams has been provided in Table A.1, Appendix A.

Table 4.4: Formation Free Energies in kJ mol^{-1} of Sulfated Cu Dimers at 698 K, 7% H_2O, 10% O_2, 30 ppm SO_2 Calculated Using SCAN-D3(BJ)vdw, at the 9 Identified Cu Dimer-forming Al-Al Pairs.[a]

Plausible sulfated	2Al Configurations (Distance between Al-Al pair in Å)				
Cu dimers	10 (6.2 Å)	12 (6.2 Å)	14 (6.2 Å)	3 (7.1 Å)	11 (7.2 Å)
$[Z_2Cu_2HSO_3]$	+130	+138	+134	+137	+105
$[Z_2Cu_2HSO_4]$	+25	+17	-27	**-1**	-18
$[Z_2Cu_2SO_3]$	+148	+20	+68	+146	+89
$[Z_2Cu_2SO_4]$	**+26**	**-17**	**-70**	+20	**-64**
	Desulfation Temperature (in K)[b]				
	654	761	874	707	847

Plausible sulfated	2Al Configurations (Distance between Al-Al pair in Å)			
Cu dimers	19 (7.3 Å)	23 (8.7 Å)	8 (9.7 Å)	5 (10.4 Å)
$[Z_2Cu_2HSO_3]$	+137	+146	+133	+141
$[Z_2Cu_2HSO_4]$	-15	+13	+10	+15
$[Z_2Cu_2SO_3]$	+98	+128	+113	+131
$[Z_2Cu_2SO_4]$	**-39**	**-48**	**-51**	**-39**
	Desulfation Temperature (in K)[b]			
	794	810	817	791

[a] The formation free energies have been expressed relative to the most exergonic $[Z_2Cu_2O_xH_y]$ species identified at the stated reaction conditions; they have been highlighted in bold in Table 4.1.

[b] The desulfation temperature for each Al-Al configuration has been reported at 7% H_2O, 10% O_2, 30 ppm SO_2

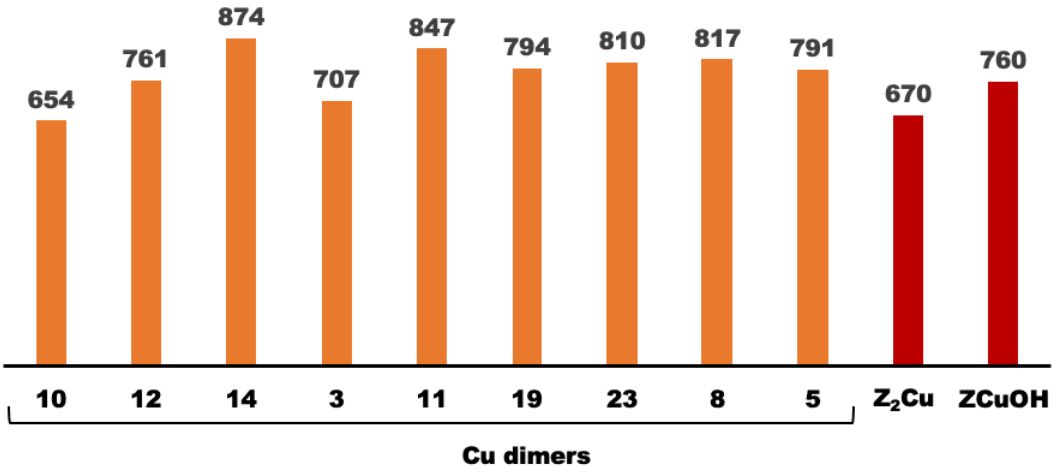

Figure 4.5: Comparison of desulfation temperatures (in K) of monatomic vs dimeric Cu species based on SCAN-D3(BJ)vdw computed energies

most exergonic $[Z_2Cu_2O_xH_y]$ species identified at 698 K, 10% O_2, 30 ppm SO_2, 7% H_2O, along with the desulfation temperature at each Al-Al configuration have been reported in **Table 4.4**.

At such high temperature conditions (698 K, 10% O_2, 30 ppm SO_2, 7% H_2O), during which the NH_3 coverage is low in NH_3-SCR of NOx, we observed a distribution of thermodynamically stable dimeric Cu sulfates and bisulfates. While the sulfated Cu dimers across all the Al-Al configurations exhibit highly exergonic sulfation energies, the strength of sulfur binding to the Cu dimers, as reflected in their desulfation energies, is influenced by the Al-Al pair arrangement. We found that configurations having both the Al-exchange sites in the same 8MR (configurations 10 and 3) displayed lower desulfation temperatures (654–707 K) than the '*bridged*' 2Al configurations (761–874 K), indicating that sulfur binds more strongly to these '*bridged*' 2Al sites (**Figure 4.5**). Representative optimized structures of the (bi)sulfate Cu dimers at both these types of Al–Al configurations have been shown in **Figure 4.4d**. Moreover, the dimeric Cu species formed at the '*bridged*' 2Al sites displayed higher

desulfation temperature compared to the monatomic Cu species (<760 K) (illustrated in **Figure 4.5**), reiterating the observation from our DFT calculations and those reported in literature,[24,25,305,306] that dimeric Cu species interact more strongly with sulfur than monatomic Cu.

4.3.3 Comparison with Experimental Data from Sulfur Exposure Experiments

We compared our high temperature sulfation reaction theoretical results with the SCR kinetic results on Cu/SSZ-13 pre- and post-sulfur exposure at 698 K, 10% O_2, 30 ppm SO_2, 7% H_2O reported by our experimental collaborators Chen et al.[327] We observe that NO_x conversion reduced significantly after SO_2 and SO_2+SO_3 exposure; the decrease was larger upon the introduction of SO_3. The change in the values of activation energy, reported before and after sulfur exposure (+93 and +53 (with SO_2)/ +55 (SO_2+SO_3) kJ mol^{-1}, respectively) could allude to a change in the SCR mechanism post high-temperature sulfur exposure, with either the sulfation of NH_3-solvated Cu dimer ($[Cu_2{}^{2+}(NH_3)O_2]^{2+}$),[26,30] or the inability of sulfated Cu dimers to form $[Cu_2{}^{2+}(NH_3)O_2]^{2+}$, impacting the SCR activity. To determine whether sulfur exposure lead to a decrease in the available Cu active sites, Chen et al.[327] titrated the amount of Cu dimers using CO as a probe reaction at 473 K. The results indicate that, consistent with our theoretical calculations, sulfur binds strongly to Cu dimers, thereby reducing the amount of CO titratable Cu dimers significantly (from 29 to 0.46 mol/g catalyst CO_2 generated pre- and post-sulfur exposure, respectively). To further validate the loss of Cu dimers following sulfur exposure, Chen et al.[327] also compared the UV-vis spectra collected of SSZ-13 catalyst (pretreated in dry air at 673 K) before and after sulfur exposure, and observed the disappearance of the Cu

dimer-associated peaks in the d-d transition regions post sulfation, and spectra that were qualitatively consistent with that of bulk Cu sulfate.

4.3.4 Conclusions

Here, we investigated high-temperature sulfur poisoning of Cu/CHA zeolite during SCR of NOx using DFT calculations, SCR rate experiments, and spectroscopic measurements. Our theoretical calculations showed that high temperature oxidizing conditions lead to the formation of a distribution of thermodynamically stable dimeric Cu moieties ($Cu_2O_{x\,=\,1\text{–}2}H_{y\,=\,1\text{–}2}$) in CHA from solvated $[CuOH]^+$ complexes, but only at certain Al-Al configurations where isolated $[CuOH]^+$ sites are in close proximity, emphasizing the role of zeolite composition (Si/Al ratio, Cu loading) and Al distribution on the Cu cation speciation at high temperatures. We found that high temperature (>673 K) sulfur exposure leads to the exergonic formation of stable $[Cu_2HSO_4]^{2+}$ and $[Cu_2SO_4]^{2+}$, which display significantly stronger sulfation energies in comparison to that of monatomic Cu, indicating that much higher temperature desulfation treatments (>700 K) would be required for regenerating Cu dimers in a CHA catalyst. While the elementary steps for forming these sulfated Cu species are unclear, our combined experimental and theoretical results suggest that following sulfur exposure at high temperatures, the strongly bound sulfur on Cu dimers renders them chemically inert to CO, and likely NH_3, consequently reducing SCR performance of the catalyst. The loss of available Cu active sites due to high temperature interaction of sulfur with Cu dimers, as observed in our CO titration measurements, and UV-vis spectra, posits a relation between the susceptibility of sulfur poisoning of a zeolite with the amount of Cu dimers present; for instance, Cu/MOR, which has a higher density of as-exchanged Cu dimers, would be expected to experience a greater degree

of sulfur poisoning and reduced catalytic performance, compared to CHA. Similarly, a CHA catalyst with low Si/Al ratio and Cu loading, will have a higher propensity for forming Z_2Cu sites compared to ZCuOH, leading to a lower concentration of Cu dimers, requiring less aggressive regeneration protocols.

Overall, our theoretical model and results for sulfur poisoning of Cu/CHA highlight the role of Al siting and reaction conditions in the exchanged metal speciation and their reactivity with sulfur, and lays the groundwork for investigating the effect NH_3 in regenerating these dimer sites.

Acknowledgements

The authors acknowledge Cummins Inc. for financial support.

Chapter 5

Contributions to Other Research Projects

I have been working with Chemical Engineering undergraduate student, Anupama Jayaraman, and my fellow group member, Asanka Wijerathne, since Spring 2019, on understanding the thermodynamics and kinetics of redispersion of Pt nanoparticles to cations in zeolites. In this study, we extended our previous research on Pd redispersion in CHA to redispersion of Pt particles in zeolites by analyzing the influence of initial Pt particle size distribution, and external reaction conditions on the interconversion between Pt particles and cations. Here, we have used DFT calculations, thermodynamic correlations and kinetic Monte Carlo (kMC) simulations to develop free energy models that encompass the thermodynamic and kinetic parameters dictating the reversible interconversion between Pt particles and Pt^{2+} cations ion-exchanged in zeolites under oxidizing and reductive reaction conditions.

For Pt catalysts supported on zeolites, stabilization of Pt metal in anchoring sites[14,240,328–331] is facilitated by the altered electronic structure and coordination of the metal to the zeolite framework.[181,328] The three-dimensional, cage-like structure of zeolites confers additional sintering and resistance due to the high energy barrier associated with particle diffusion through zeolite pores.[181,329] Nonetheless, under certain reaction conditions, particles may overcome the energetic barrier to diffusion, enabling intercon-

version between different Pt metal structures.[14,240,328,329] The thermodynamics and kinetics of particle restructuring depends on the zeolite composition and topology, reaction conditions and particle size. Under high temperature oxidative conditions, particles disintegrate into smaller particles or single atoms. Conversely, low temperature reducing conditions facilitate particle agglomeration and growth.[14,240,328–330] Such a reversible transformation between different metal speciation induced by varying reaction conditions, has been explored in several studies Pt cluster formation from isolated atoms in Y zeolite during ethane dehydrogenation at 973 K,[332] high-temperature oxidations on single-site Pt and Pt clusters in high silica CHA[14,202,240] and ZSM-5.[333,334]

We use density functional theory (DFT) to compute the energies for the most stable Pt^{2+} cation structures and use free energy expressions for supported and unsupported nanoparticles to estimate the size-dependent energies of encapsulated Pt particles in CHA zeolites. We combine these cation and particle energies at different particle sizes and gaseous environmental conditions ($P_{O_2}, P_{H_2O}, P_{H_2}, T$) to develop thermodynamic phase diagrams for Pt speciation within the zeolite. We have also performed kinetic Monte Carlo (kMC) simulations for a gas-phase mediated Ostwald Ripening mechanism followed by trapping of PtO_2(g) monomers at the atom-trapping Al-exchange sites in the zeolite, to model the kinetics of particle redispersion. Currently we have a manuscript based on this study in preparation (Jayaraman, A.; Mandal, K.; Wijerathne, A.; Gounder, R.; and Paolucci, C. Predicting Conditions and Rates of Pt Nanoparticle Redispersion to Cations in Zeolites, *In Preparation*).

My specific contributions to this work have been helping Anupama Jayaraman in performing DFT calculations of Pt/SSZ-13 to compute the Pt cation energies, and developing the thermodynamic model for the free energy of supported particles. I also

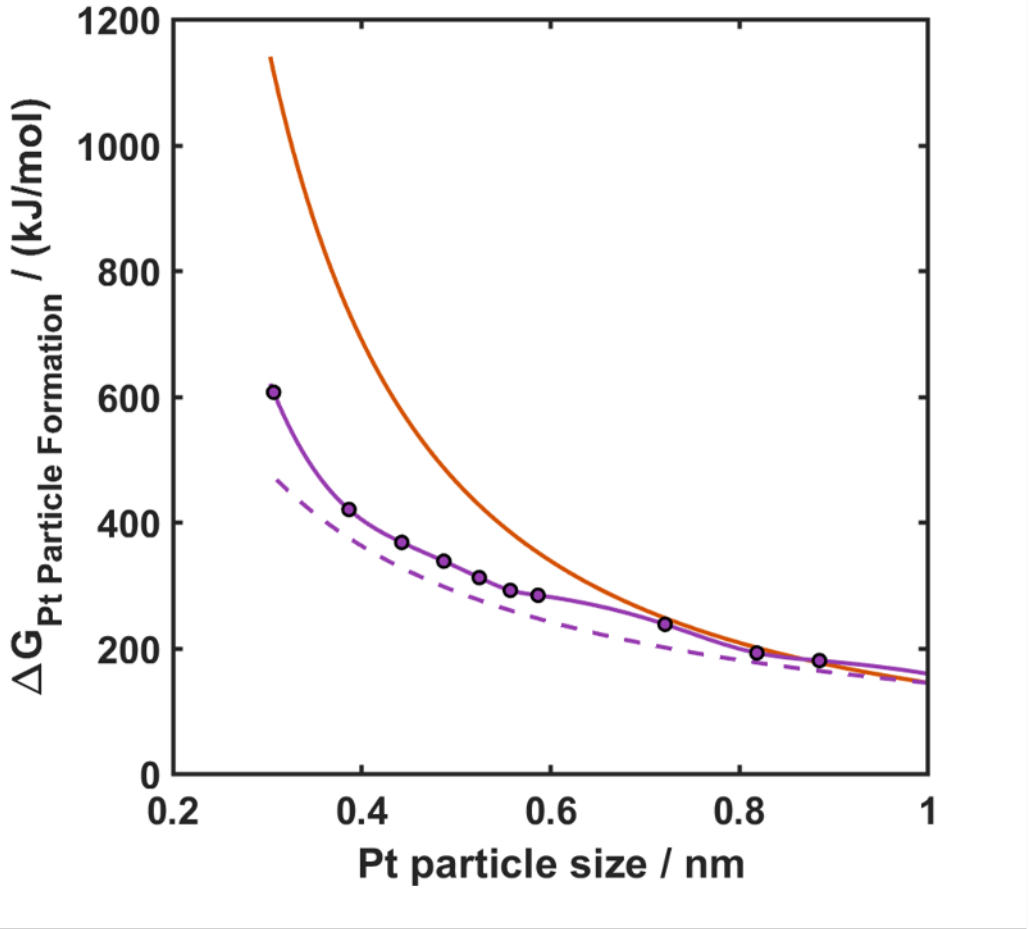

Figure 5.1: Plot of Gibbs Free Energy for Pt particle formation as a function of particle size. The orange, dotted purple, and solid purple with purple circles lines represent energies with for $\gamma_{\text{avg,Pt}} = 75$ meV/Å^2 for the supported free energy model, the unsupported free energy without interpolation of energies for small Pt particles ($<$ 1 nm), and unsupported free energy model with interpolation of Pt particle energies, respectively. The purple circles represent the DFT calculated energies of Pt clusters $<$ 1 nm diameter.

performed DFT calculations for Pt nanoparticle clusters, ranging from 1-75 atoms, to develop correlations for free energies of unsupported Pt particles (**Figure 5.1**). In addition, I'm also involved in drafting, writing, and editing of the manuscript.

Chapter 6

Final Conclusions and Outlook for the Future

In this dissertation, we used computational modeling tools such as density functional theory (DFT), and wave function theory (WFT) calculations, AIMD and kinetic Monte Carlo simulations, first-principles based thermodynamic models, experimental and spectroscopic techniques, to understand the underlying thermodynamics and kinetic factors that govern the thermal and chemical deactivation of zeolite-supported metal catalysts, using ion-exchanged Pd- and Cu/zeolites as model systems.

Pd/zeolites have been explored for numerous applications such as Wacker oxidation, alkene hydrogenation, methane oxidation, and aftertreament of diesel exhaust, with their potential role for low-temperature NOx adsorption being the focus of numerous studies. A mechanistic understanding of the solvation chemistry of Pd cations in the presence of H_2O, and its effect on the coordination environment of Pd-nitrosyl complexes, and CO oxidation can reveal crucial information about the catalytic performance, stability, and deactivation processes of Pd/zeolites. A combined computational and experimental study of Pd/CHA showed that at conditions of practical interest (< 573 K) in oxidation reactions, and passive NOx adsorption (PNA), H_2O is ubiquitously present in the reaction environment (0.3-7% H_2O), and

analogous to the behavior reported for Cu/zeolites and homogeneous Pd inorganic chemistry, leads to the formation of fully solvated, four-fold coordinated mobile Pd complexes. Our studies demonstrated that H_2O-solvation of Pd cations in zeolites affects PNA performance of Pd/CHA by increasing the NO desorption temperature (an increase of ∼200 K at 4.5% H_2O) due to the formation of thermodynamically stable $[Pd^{II}(NO^-)(H_2O)_3]^+$ complexes, which had reduced mobility relative to fully H_2O-solvated Pd complexes. It is also interesting to note that presence of H_2O introduces a homogeneity across zeolites of different topologies, which otherwise possess distinct NO adsorption/ desorption profiles in the absence of H_2O, by the formation of these mobile H_2O-solvated Pd-nitrosyl complexes.

Furthermore, our study on redispersion of Pd particles in CHA highlights the role of H_2O on sintering of these zeolites, with H_2O driving the thermodynamic equilibrium towards agglomeration of Pd cations to PdO particles at low temperatures, and accelerating catalyst deactivation. Our research findings suggest that mitigating the presence of H_2O in the reaction environment could improve the low-temperature performance and longevity of Pd/zeolites for PNAs, and automobile exhaust treatment. Probable solutions can range from changes in the architecture of the aftertreatment system (which is often difficult or cost-prohibitive to implement), and synthesis of better zeolite supports. Zeolites with a more exothermic ion-exchange reaction would possess higher thermodynamic resistance to the structural transformation of cations to particles. Hydrophobic zeolite frameworks, and (or) zeolite synthesis methods that impart greater hydrophobicity to CHA zeolites, could also be potential routes to explore. However, we would also need to evaluate the affects of such treatments or the impact on the NO storage capacity, catalytic activity, and hydrothermal stability of when using other zeolites that have more exergonic exchange energies. Our ther-

modynamic and kinetic models for structural interconversion between particles and cations in zeolites also provide a potential roadmap for the study of particle sintering (or redispersion) of other metal oxide supports where, similar to zeolitic supports, the distribution and site density of trapping sites or defects play a key role in catalyst stability and regeneration capabilities.

Investigations into the sulfur poisoning and regeneration of Cu/zeolites for SCR of NOx in diesel engines showed that formation of dimeric Cu species at high temperatures is deleterious to the SCR performance of the material. Sulfated Cu dimers possess excellent thermodynamic stability, and zeolites with a higher concentration of Cu dimers would require significantly higher deSOx temperatures for catalyst regeneration, which in turn raises concerns regarding the hydrothermal stability of these materials under such conditions. Our results suggest that optimizing zeolite synthesis protocols to avoid Al configurations that favor Cu dimers, and ideally facilitate formation of solely 6MR 2Al exchange sites without other adjacent Al, can attenuate sulfur-induced catalyst poisoning, lower regeneration temperatures, and improve the catalyst life-cycle.

In chapter 3, “Kinetic and Thermodynamic Factors Influencing Palladium Nanoparticle Redispersion into Mononuclear Pd(II) Cations in Zeolite Supports”, our study focused on the redispersion of Pd nanoparticles present on the external surface of a zeolite support during high-temperature air treatments. Subsequent studies can be performed for (a) redispersion of Pd nanoparticles with different particle size distributions, (b) redispersion of Pd nanoclusters encapsulated in the zeolite pores to investigate the effect of zeolite confinement on the stability of nanoclusters, and (c) impact of the presence of other external oxidizing gases such as NO. We can also develop similar thermodynamic and kinetic models for Pd nanoparticle redispersion on

metal-oxide supports with atom trapping sites and(or) defects such as ceria, alumina, etc. to explore the influence of the catalyst support on particle redispersion.

In the next phase of our study discussed in Chapter 4, "Effect of Reaction Conditions and SO_2 Exposure on Cu Speciation in SSZ13 Zeolites", the goal is to investigate the effect of sulfur exposure on Cu dimers in the presence of NH_3. Some recent studies[26,30] have looked at the effect of sulfur exposure on NH_3-solvated Cu dimers ($[Cu_2^{II}(NH_3)_2O_2]^{2+}$), which are intermediates formed during the SCR redox cycle, and found that SO_2 strongly reacts with $[Cu_2^{II}(NH_3)_2O_2]^{2+}$ forming $HSO_4(NH_4)$ that contribute to sulfur accumulation in Cu/CHA, and adversely impact the probability of pairing of two proximal $[Cu^{I}(NH_3)_2]^{+}$ complexes. The physical blocking of active sites in Cu/CHA by sulfur has been shown to be reversible in nature, with desulfation and regeneration of monatomic Cu (Z_2Cu and ZCuOH) sites in Cu/CHA observed at temperatures ~673 K when decomposition of $HSO_4(NH_4)$ occurs.[23,26,28] However, the interaction of NH_3 with framework bound sulfated dimeric Cu sites in Cu/CHA is not well known. Thus, we would need to perform DFT calculations and AIMD simulations for the reaction of $NH_3$with hydroxylated and (bi)sulfated Cu dimers that are bound to the zeolite framework, and generate thermodynamic phase diagrams for a variety of NH_3 coverages and temperatures. An atomistic and thermodynamic study of the local coordination environment of the sulfated Cu dimers (NH_3-solvated vs framework-bound) at different Al configurations and reaction conditions, along with the corresponding experimental studies on sulfur-poisoned Cu/CHA in the presence of NH_3, is thereby required to develop a complete mechanistic understanding of the physical and chemical deactivation of Cu/CHA in the presence of sulfur, and for further development of effective catalyst regeneration protocols.

Bibliography

(1) Crespo-Quesada, M.; Yarulin, A.; Jin, M.; Xia, Y.; Kiwi-Minsker, L. Structure sensitivity of alkynol hydrogenation on shape- and size-controlled palladium nanocrystals: Which sites are most active and selective? *Journal of the American Chemical Society* **2011**, *133*, 12787–12794.

(2) Liu, L.; Corma, A. Evolution of Isolated Atoms and Clusters in Catalysis. *Trends in Chemistry* **2020**, *2*, 383–400.

(3) Martín, A. J.; Mitchell, S.; Mondelli, C.; Jaydev, S.; Pérez-Ramírez, J. Unifying views on catalyst deactivation. *Nature Catalysis* **2022**, *5*, 854–866.

(4) Argyle, M. D.; Bartholomew, C. H. Heterogeneous catalyst deactivation and regeneration: A review. *Catalysts* **2015**, *5*, 145–269.

(5) Bartholomew, C. H. Mechanisms of nickel catalyst poisoning. *Studies in Surface Science and Catalysis* **1987**, 81–104.

(6) Bartholomew, C. H. Mechanisms of catalyst deactivation. *Applied Catalysis A: General* **2001**, *212*, Catalyst Deactivation, 17–60.

(7) Bartholomew, C.; Agrawal, P.; Katzer, J. In Eley, D., Pines, H., Weisz, P. B., Eds.; Advances in Catalysis, Vol. 31; Academic Press: 1982, pp 135–242.

(8) Liu, L.; Zakharov, D. N.; Arenal, R.; Concepcion, P.; Stach, E. A.; Corma, A. Evolution and stabilization of subnanometric metal species in confined space by in situ TEM. *Nature Communications* **2018**, *9*, 1–10.

(9) Wu, S. M.; Yang, X. Y.; Janiak, C. Confinement Effects in Zeolite-Confined Noble Metals. *Angewandte Chemie - International Edition* **2019**, *58*, 12340–12354.

(10) Chai, Y.; Shang, W.; Li, W.; Wu, G.; Dai, W.; Guan, N.; Li, L. Noble Metal Particles Confined in Zeolites: Synthesis, Characterization, and Applications. *Advanced Science* **2019**, *6*, DOI: 10.1002/advs.201900299.

(11) Zheng, Y.; Kovarik, L.; Engelhard, M. H.; Wang, Y.; Wang, Y.; Gao, F.; Szanyi, J. Low-Temperature Pd/Zeolite Passive NOx Adsorbers: Structure, Performance, and Adsorption Chemistry. *Journal of Physical Chemistry C* **2017**, *121*, 15793–15803.

(12) Ryou, Y. S.; Lee, J.; Cho, S. J.; Lee, H.; Kim, C. H.; Kim, D. H. Activation of Pd/SSZ-13 catalyst by hydrothermal aging treatment in passive NO adsorption performance at low temperature for cold start application. *Applied Catalysis B: Environmental* **2017**, *212*, 140–149.

(13) Gu, Y.; Zelinsky, R. P.; Chen, Y. R.; Epling, W. S. Investigation of an irreversible NOx storage degradation Mode on a Pd/BEA passive NOx adsorber. *Applied Catalysis B: Environmental* **2019**, *258*, 118032.

(14) Moliner, M.; Gabay, J. E.; Kliewer, C. E.; Carr, R. T.; Guzman, J.; Casty, G. L.; Serna, P.; Corma, A. Reversible Transformation of Pt Nanoparticles into Single Atoms inside High-Silica Chabazite Zeolite. *Journal of the American Chemical Society* **2016**, *138*, 15743–15750.

(15) Petrov, A. W.; Ferri, D.; Krumeich, F.; Nachtegaal, M.; Van Bokhoven, J. A.; Kröcher, O. Stable complete methane oxidation over palladium based zeolite catalysts. *Nature Communications* **2018**, *9*, 2545.

(16) Bello, E.; Margarit, V. J.; Gallego, E. M.; Schuetze, F.; Hengst, C.; Corma, A.; Moliner, M. Deactivation and regeneration studies on Pd-containing medium pore zeolites as passive NOx adsorbers (PNAs) in cold-start applications. *Microporous and Mesoporous Materials* **2020**, *302*, 110222.

(17) Lardinois, T. M.; Bates, J. S.; Lippie, H. H.; Russell, C. K.; Miller, J. T.; Meyer, H. M.; Unocic, K. A.; Prikhodko, V.; Wei, X.; Lambert, C. K.; Getsoian, A. B.; Gounder, R. Structural Interconversion between Agglomerated Palladium Domains and Mononuclear Pd(II) Cations in Chabazite Zeolites. *Chemistry of Materials* **2021**, *33*, 1698–1713.

(18) Paolucci, C.; Di Iorio, J. R.; Schneider, W. F.; Gounder, R. Solvation and mobilization of copper active sites in zeolites by ammonia: Consequences for the catalytic reduction of nitrogen oxides. *Accounts of Chemical Research* **2020**, *53*, 1881–1892.

(19) Marberger, A.; Petrov, A. W.; Steiger, P.; Elsener, M.; Kröcher, O.; Nachtegaal, M.; Ferri, D. Time-resolved copper speciation during selective catalytic reduction of NO on Cu-SSZ-13. *Nature Catalysis* **2018**, *1*, 221–227.

(20) Lomachenko, K. A.; Borfecchia, E.; Negri, C.; Berlier, G.; Lamberti, C.; Beato, P.; Falsig, H.; Bordiga, S. The Cu-CHA deNOx Catalyst in Action: Temperature-Dependent NH3-Assisted Selective Catalytic Reduction Monitored by Operando XAS and XES. *Journal of the American Chemical Society* **2016**, *138*, 12025–12028.

(21) Millan, R.; Cnudde, P.; Van Speybroeck, V.; Boronat, M. Mobility and Reactivity of Cu+Species in Cu-CHA Catalysts under NH3-SCR-NOx Reaction Conditions: Insights from AIMD Simulations. *Journal of the American Chemical Society* **2021**, *1*, 1778–1787.

(22) Wijayanti, K.; Xie, K.; Kumar, A.; Kamasamudram, K.; Olsson, L. Effect of gas compositions on SO2 poisoning over Cu/SSZ-13 used for NH3-SCR. *Applied Catalysis B: Environmental* **2017**, *219*, 142–154.

(23) Kumar, A.; Smith, M. A.; Kamasamudram, K.; Currier, N. W.; Yezerets, A. Chemical deSOx: An effective way to recover Cu-zeolite SCR catalysts from sulfur poisoning. *Catalysis Today* **2016**, *267*, 10–16.

(24) Shih, A. J. et al. Spectroscopic and kinetic responses of Cu-SSZ-13 to SO2 exposure and implications for NOx selective catalytic reduction. *Applied Catalysis A: General* **2019**, *574*, 122–131.

(25) Jangjou, Y.; Do, Q.; Gu, Y.; Lim, L. G.; Sun, H.; Wang, D.; Kumar, A.; Li, J.; Grabow, L. C.; Epling, W. S. Nature of Cu Active Centers in Cu-SSZ-13 and Their Responses to SO2 Exposure. *ACS Catalysis* **2018**, *8*, 1325–1337.

(26) Bjerregaard, J. D.; Votsmeier, M.; Grönbeck, H. Mechanism for SO2 poisoning of Cu-CHA during low temperature NH3-SCR. *Journal of Catalysis* **2023**, *417*, 497–506.

(27) Luo, J.; Wang, D.; Kumar, A.; Li, J.; Kamasamudram, K.; Currier, N.; Yezerets, A. Identification of two types of Cu sites in Cu/SSZ-13 and their unique responses to hydrothermal aging and sulfur poisoning. *Catalysis Today* **2016**, *267*, 3–9.

(28) Kumar, A.; Smith, M. A.; Kamasamudram, K.; Currier, N. W.; An, H.; Yezerets, A. Impact of different forms of feed sulfur on small-pore Cu-zeolite SCR catalyst. *Catalysis Today* **2014**, *231*, 75–82.

(29) Tang, Y.; Wang, D.; Wang, X.; Zha, Y.; An, H.; Kamasamudram, K.; Yezerets, A. Impact of low temperature sulfur exposure on the aging of small pore Cu-zeolite SCR catalyst. *Catalysis Today* **2021**, *360*, 234–240.

(30) Molokova, A. Y.; Borfecchia, E.; Martini, A.; Pankin, I. A.; Atzori, C.; Mathon, O.; Bordiga, S.; Wen, F.; Vennestrøm, P. N.; Berlier, G.; Janssens, T. V.; Lomachenko, K. A. SO2Poisoning of Cu-CHA deNOxCatalyst: The Most Vulnerable Cu Species Identified by X-ray Absorption Spectroscopy. *Journal of the American Chemical Society* **2022**, *2*, 787–792.

(31) Dahlin, S.; Lantto, C.; Englund, J.; Westerberg, B.; Regali, F.; Skoglundh, M.; Pettersson, L. J. Chemical aging of Cu-SSZ-13 SCR catalysts for heavy-duty vehicles – Influence of sulfur dioxide. *Catalysis Today* **2019**, *320*, 72–83.

(32) Kosinov, N.; Liu, C.; Hensen, E. J.; Pidko, E. A. Engineering of Transition Metal Catalysts Confined in Zeolites. *Chemistry of Materials* **2018**, *30*, 3177–3198.

(33) Li, Y.; Li, L.; Yu, J. Applications of Zeolites in Sustainable Chemistry. *Chem* **2017**, *3*, 928–949.

(34) Harris, J. W.; Bates, J. S.; Bukowski, B. C.; Greeley, J.; Gounder, R. Opportunities in Catalysis over Metal-Zeotypes Enabled by Descriptions of Active Centers beyond Their Binding Site. *ACS Catalysis* **2020**, *10*, 9476–9495.

(35) Dusselier, M.; Davis, M. E. Small-Pore Zeolites: Synthesis and Catalysis. *Chemical Reviews* **2018**, *118*, 5265–5329.

(36) Thomas, J. M.; Raja, R.; Lewis, D. W. Single-site heterogeneous catalysts. *Angewandte Chemie - International Edition* **2005**, *44*, 6456–6482.

(37) Paolucci, C.; Khurana, I.; Parekh, A. A.; Li, S.; Shih, A. J.; Li, H.; Di Iorio, J. R.; Albarracin-Caballero, J. D.; Yezerets, A.; Miller, J. T.; Delgass, W. N.; Ribeiro, F. H.; Schneider, W. F.; Gounder, R. Dynamic multinuclear sites formed by mobilized copper ions in NOx selective catalytic reduction. *Science* **2017**, *357*, 898–903.

(38) Chen, L.; Falsig, H.; Janssens, T. V.; Grönbeck, H. Activation of oxygen on (NH3–Cu–NH3)+ in NH3-SCR over Cu-CHA. *Journal of Catalysis* **2018**, *358*, 179–186.

(39) Brogaard, R. Y.; Kømurcu, M.; Dyballa, M. M.; Botan, A.; Van Speybroeck, V.; Olsbye, U.; De Wispelaere, K. Ethene Dimerization on Zeolite-Hosted Ni Ions: Reversible Mobilization of the Active Site. *ACS Catalysis* **2019**, *9*, 5645–5650.

(40) Gao, F.; Mei, D.; Wang, Y.; Szanyi, J.; Peden, C. H. Selective Catalytic Reduction over Cu/SSZ-13: Linking Homo- and Heterogeneous Catalysis. *Journal of the American Chemical Society* **2017**, *139*, 4935–4942.

(41) Negri, C.; Selleri, T.; Borfecchia, E.; Martini, A.; Lomachenko, K. A.; Janssens, T. V.; Cutini, M.; Bordiga, S.; Berlier, G. Structure and Reactivity of Oxygen-Bridged Diamino Dicopper(II) Complexes in Cu-Ion-Exchanged Chabazite Catalyst for NH3-Mediated Selective Catalytic Reduction. *Journal of the American Chemical Society* **2020**, *142*, 15884–15896.

(42) Crabtree, R. H.; Michael, D.; Mingos, P., *Comprehensive organometallic chemistry III*; 12; Elsevier: Amsterdam; Boston, 2007; Vol. 1, pp 1–8798.

(43) Grice, K. A.; Scheuermann, M. L.; Goldberg, K. I., *Higher Oxidation State Organopalladium and Platinum Chemistry: Five-coordinate Platinum(IV) complexes*; Iii; Springer: 2011; Vol. 35, pp 129–156.

(44) Henry, P. M., *Palladium Catalyzed Oxidation of Hydrocarbons*; Springer Science Business Media: 1980; Vol. 2, p 435.

(45) Balch, A. L. Odd Oxidation States of Palladium and Platinum. *Comments on Inorganic Chemistry* **1984**, *3*, 51–67.

(46) Powers, D. C.; Ritter, T. Bimetallic Pd(III) complexes in palladium-catalysed carbon-heteroatom bond formation. *Nature Chemistry* **2009**, *1*, 302–309.

(47) Mirica, L. M.; Khusnutdinova, J. R. Structure and electronic properties of Pd(III) complexes. *Coordination Chemistry Reviews* **2013**, *257*, 299–314.

(48) Goggin, P. L.; Mink, J. Palladium(I) carbonyl halide complexes. *Journal of the Chemical Society, Dalton Transactions* **1974**, 534.

(49) Jaworski, J. N.; Kozack, C. V.; Tereniak, S. J.; Knapp, S. M. M.; Landis, C. R.; Miller, J. T.; Stahl, S. S. Operando Spectroscopic and Kinetic Characterization of Aerobic Allylic C-H Acetoxylation Catalyzed by Pd(OAc)2/4,5-Diazafluoren-9-one. *Journal of the American Chemical Society* **2019**, *141*, 10462–10474.

(50) Canty, A. J. The +IV Oxidation State in Organopalladium Chemistry. *Platinum Metals Review* **1993**, *37*, 2–7.

(51) Canty, A. J. Development of Organopalladium(IV) Chemistry: Fundamental Aspects and Systems for Studies of Mechanism in Organometallic Chemistry and Catalysis. *Accounts of Chemical Research* **1992**, *25*, 83–90.

(52) Canty, A. J. Organopalladium and platinum chemistry in oxidising milieu as models for organic synthesis involving the higher oxidation states of palladium. *Dalton Transactions* **2009**, 10409–10417.

(53) Muñiz, K. High-oxidation-state palladium catalysis: New reactivity for organic synthesis. *Angewandte Chemie - International Edition* **2009**, *48*, 9412–9423.

(54) Sehnal, P.; Taylor, R. J.; Fairlamb, L. J. Emergence of palladium(IV) chemistry in synthesis and catalysis. *Chemical Reviews* **2010**, *110*, 824–889.

(55) Ryan; Cooper; Tauer No Title No Title No Title. *Paper Knowledge . Toward a Media History of Documents* **2013**, 12–26.

(56) Shimada, S.; Li, Y. H.; Choe, Y. K.; Tanaka, M.; Bao, M.; Uchimaru, T. Multinuclear palladium compounds containing palladium centers ligated by five silicon atoms. *Proceedings of the National Academy of Sciences of the United States of America* **2007**, *104*, 7758–7763.

(57) Chen, W.; Shimada, S.; Tanaka, M. Synthesis and structure of formally hexavalent palladium complexes. *Science* **2002**, *295*, 308–310.

(58) Knott, B. C.; Nimlos, C. T.; Robichaud, D. J.; Nimlos, M. R.; Kim, S.; Gounder, R. Consideration of the Aluminum Distribution in Zeolites in Theoretical and Experimental Catalysis Research. *ACS Catalysis* **2018**, *8*, 770–784.

(59) Dědeček, J.; Sobalík, Z.; Wichterlová, B. Siting and Distribution of Framework Aluminium Atoms in Silicon-Rich Zeolites and Impact on Catalysis. *Catalysis Reviews - Science and Engineering* **2012**, *54*, 135–223.

(60) Sklenak, S.; Dědeček, J.; Li, C.; Wichterlová, B.; Gábová, V.; Sierka, M.; Sauer, J. Aluminum siting in silicon-rich zeolite frameworks: A combined high-resolution 27Al NMR spectroscopy and quantum mechanics/molecular mechanics study of ZSM-5. *Angewandte Chemie - International Edition* **2007**, *46*, 7286–7289.

(61) Yokoi, T.; Mochizuki, H.; Namba, S.; Kondo, J. N.; Tatsumi, T. Control of the Al Distribution in the Framework of ZSM-5 Zeolite and Its Evaluation by Solid-State NMR Technique and Catalytic Properties. *Journal of Physical Chemistry C* **2015**, *119*, 15303–15315.

(62) Pinar, A. B.; Gómez-Hortigüela, L.; McCusker, L. B.; Pérez-Pariente, J. Controlling the aluminum distribution in the zeolite ferrierite via the organic structure directing agent. *Chemistry of Materials* **2013**, *25*, 3654–3661.

(63) Descorme, C.; Gélin, P.; Primet, M.; Lécuyer, C. Infrared study of nitrogen monoxide adsorption on palladium ion-exchanged ZSM-5 catalysts. *Catalysis Letters* **1996**, *41*, 133–138.

(64) Khivantsev, K.; Jaegers, N. R.; Kovarik, L.; Hanson, J. C.; Tao, F. (; Tang, Y.; Zhang, X.; Koleva, I. Z.; Aleksandrov, H. A.; Vayssilov, G. N.; Wang, Y.; Gao, F.; Szanyi, J. Achieving Atomic Dispersion of Highly Loaded Transition Metals in Small-Pore Zeolite SSZ-13: High-Capacity and High-Efficiency Low-Temperature CO and Passive NO x Adsorbers. *Angewandte Chemie* **2018**, *130*, 16914–16919.

(65) Khivantsev, K.; Jaegers, N. R.; Kovarik, L.; Prodinger, S.; Derewinski, M. A.; Wang, Y.; Gao, F.; Szanyi, J. Palladium/Beta zeolite passive NOx adsorbers (PNA): Clarification of PNA chemistry and the effects of CO and zeolite crystallite size on PNA performance. *Applied Catalysis A: General* **2019**, *569*, 141–148.

(66) Khivantsev, K.; Jaegers, N. R.; Koleva, I. Z.; Aleksandrov, H. A.; Kovarik, L.; Engelhard, M.; Gao, F.; Wang, Y.; Vayssilov, G. N.; Szanyi, J. Stabilization of Super Electrophilic Pd+2Cations in Small-Pore SSZ-13 Zeolite. *Journal of Physical Chemistry C* **2020**, *124*, 309–321.

(67) Khivantsev, K.; Gao, F.; Kovarik, L.; Wang, Y.; Szanyi, J. Molecular Level Understanding of How Oxygen and Carbon Monoxide Improve NOx Storage in Palladium/SSZ-13 Passive NOx Adsorbers: The Role of NO+ and Pd(II)(CO)(NO) Species. *Journal of Physical Chemistry C* **2018**, *122*, 10820–10827.

(68) Khivantsev, K.; Jaegers, N. R.; Kovarik, L.; Hu, J. Z.; Gao, F.; Wang, Y.; Szanyi, J. Palladium/Zeolite Low Temperature Passive NOx Adsorbers (PNA): Structure-Adsorption Property Relationships for Hydrothermally Aged PNA Materials. *Emission Control Science and Technology* **2020**, *6*, 126–138.

(69) Kowalak, S.; Weiss, R. C.; Balkus, K. J. Zeolite encapsulated Pd(salen), a selective hydrogenation catalyst. *Journal of the Chemical Society, Chemical Communications* **1991**, 57–58.

(70) Zhang, J.; Wang, L.; Shao, Y.; Wang, Y.; Gates, B. C.; Xiao, F. S. A Pd@Zeolite Catalyst for Nitroarene Hydrogenation with High Product Selectivity by Sterically Controlled Adsorption in the Zeolite Micropores. *Angewandte Chemie - International Edition* **2017**, *56*, 9747–9751.

(71) Armor, J. N. Catalytic reduction of nitrogen oxides with methane in the presence of excess oxygen: A review. *Catalysis Today* **1995**, *26*, 147–158.

(72) Cargnello, M.; Delgado Jaén, J. J.; Hernández Garrido, J. C.; Bakhmutsky, K.; Montini, T.; Calvino Gámez, J. J.; Gorte, R. J.; Fornasiero, P. Exceptional activity for methane combustion over modular Pd@CeO2 subunits on functionalized Al2O3. *Science* **2012**, *337*, 713–717.

(73) Petrov, A. W.; Ferri, D.; Tarik, M.; Kröcher, O.; van Bokhoven, J. A. Deactivation Aspects of Methane Oxidation Catalysts Based on Palladium and ZSM-5. *Topics in Catalysis* **2017**, *60*, 123–130.

(74) Losch, P.; Huang, W.; Vozniuk, O.; Goodman, E. D.; Schmidt, W.; Cargnello, M. Modular Pd/Zeolite Composites Demonstrating the Key Role of Support Hydrophobic/Hydrophilic Character in Methane Catalytic Combustion. *ACS Catalysis* **2019**, *9*, 4742–4753.

(75) Imbao, J.; van Bokhoven, J. A.; Clark, A.; Nachtegaal, M. Elucidating the mechanism of heterogeneous Wacker oxidation over Pd-Cu/zeolite Y by transient XAS. *Nature Communications* **2020**, *11*, 1–9.

(76) Ali, A.; Chin, Y. H.; Resasco, D. E. Redispersion of Pd on acidic supports and loss of methane combustion activity during the selective reduction of NO by CH4. *Catalysis Letters* **1998**, *56*, 111–117.

(77) Chen, H. Y.; Collier, J. E.; Liu, D.; Mantarosie, L.; Durán-Martín, D.; Novák, V.; Rajaram, R. R.; Thompsett, D. Low Temperature NO Storage of Zeolite Supported Pd for Low Temperature Diesel Engine Emission Control. *Catalysis Letters* **2016**, *146*, 1706–1711.

(78) Mihai, O.; Trandafilović, L.; Wentworth, T.; Torres, F. F.; Olsson, L. The Effect of Si/Al Ratio for Pd/BEA and Pd/SSZ-13 Used as Passive NOx Adsorbers. *Topics in Catalysis* **2018**, *61*, 2007–2020.

(79) Gupta, A.; Kang, S. B.; Harold, M. P. NOx uptake and release on Pd/SSZ-13: Impact Of Feed composition and temperature. *Catalysis Today* **2021**, *360*, 411–425.

(80) Ambast, M.; Karinshak, K.; Rahman, B. M. M.; Grabow, L. C.; Harold, M. P. Passive NOx adsorption on Pd/H-ZSM-5: Experiments and modeling. *Applied Catalysis B: Environmental* **2020**, *269*, 118802.

(81) Malamis, S. A.; Harold, M. P.; Epling, W. S. Coupled NO and C3H6 Trapping, Release and Conversion on Pd/BEA: Evaluation of the Lean Hydrocarbon NOx Trap. *Industrial and Engineering Chemistry Research* **2019**, *58*, 22912–22923.

(82) Theis, J. R.; Ura, J. A. Assessment of zeolite-based Low temperature NOx adsorbers: Effect of reductants during multiple sequential cold starts. *Catalysis Today* **2021**, *360*, 340–349.

(83) Primet, M.; Taarit, Y. B. Infrared study of oxidized and reduced palladium loaded zeolites. *Journal of Physical Chemistry* **1977**, *81*, 1317–1324.

(84) Che, M.; Dutel, J. F.; Gallezot, P.; Primet, M. A study of the chemisorption of nitric oxide on PdY zeolite. Evidence for a room temperature oxidative dissolution of Pd crystallites. *Journal of Physical Chemistry* **1976**, *80*, 2371–2381.

(85) Ryou, Y. S.; Lee, J.; Lee, H.; Kim, C. H.; Kim, D. H. Effect of various activation conditions on the low temperature NO adsorption performance of Pd/SSZ-13 passive NOx adsorber. *Catalysis Today* **2019**, *320*, 175–180.

(86) Kim, Y.; Hwang, S.; Lee, J.; Ryou, Y. S.; Lee, H.; Kim, C. H.; Kim, D. H. Comparison of NO x Adsorption/Desorption Behaviors over Pd/CeO 2 and Pd/SSZ-13 as Passive NO x Adsorbers for Cold Start Application. *Emission Control Science and Technology* **2019**, *5*, 172–182.

(87) Mei, D.; Gao, F.; Szanyi, J.; Wang, Y. Mechanistic insight into the passive NOx adsorption in the highly dispersed Pd/HBEA zeolite. *Applied Catalysis A: General* **2019**, *569*, 181–189.

(88) Baerlocher, C.; McCusker, L. Database of Zeolite Structures http://www.iza-structure.org/databases/.

(89) Li, S.; Li, H.; Gounder, R.; Debellis, A.; Müller, I. B.; Prasad, S.; Moini, A.; Schneider, W. F. First-Principles Comparison of Proton and Divalent Copper Cation Exchange Energy Landscapes in SSZ-13 Zeolite. *Journal of Physical Chemistry C* **2018**, *122*, 23564–23573.

(90) Loewenstein, W. The distribution of aluminum in the tetrahedra of silicates and aluminates. *American Mineralogist* **1954**, *39*, 92–96.

(91) Ariana, R. No Title No Title No Title. **2016**, 1–23.

(92) Hayton, T. W.; Legzdins, P.; Sharp, W. B. Coordination and organometallic chemistry of metal-NO complexes. *Chemical Reviews* **2002**, *102*, 935–991.

(93) Crabtree, R. H. In *The Organometallic Chemistry of the Transition Metals*, sixth; John Wiley Sons, Ltd: 2014, pp 40–68.

(94) Paolucci, C.; Parekh, A. A.; Khurana, I.; Di Iorio, J. R.; Li, H.; Albarracin Caballero, J. D.; Shih, A. J.; Anggara, T.; Delgass, W. N.; Miller, J. T.; Ribeiro, F. H.; Gounder, R.; Schneider, W. F. Catalysis in a cage: Condition-dependent speciation and dynamics of exchanged cu cations in ssz-13 zeolites. *Journal of the American Chemical Society* **2016**, *138*, 6028–6048.

(95) Wang, L.; Chen, H.; Wang, W. N-H bond activation in ammonia by TM-SSZ-13 (Fe, Co, Ni and Cu) zeolites: A first-principles calculation. *Physical Chemistry Chemical Physics* **2019**, *21*, 1506–1513.

(96) Fickel, D. W.; Lobo, R. F. Copper coordination in Cu-SSZ-13 and Cu-SSZ-16 investigated by variable-temperature XRD. *Journal of Physical Chemistry C* **2010**, *114*, 1633–1640.

(97) Szanyi, J.; Kwak, J. H.; Zhu, H.; Peden, C. H. Characterization of Cu-SSZ-13 NH3 SCR catalysts: An in situ FTIR study. *Physical Chemistry Chemical Physics* **2013**, *15*, 2368–2380.

(98) Korhonen, S. T.; Fickel, D. W.; Lobo, R. F.; Weckhuysen, B. M.; Beale, A. M. Isolated Cu2+ ions: Active sites for selective catalytic reduction of NO. *Chemical Communications* **2011**, *47*, 800–802.

(99) Fickel, D. W.; D'Addio, E.; Lauterbach, J. A.; Lobo, R. F. The ammonia selective catalytic reduction activity of copper-exchanged small-pore zeolites. *Applied Catalysis B: Environmental* **2011**, *102*, 441–448.

(100) Di Iorio, J. R.; Nimlos, C. T.; Gounder, R. Introducing catalytic diversity into single-site chabazite zeolites of fixed composition via synthetic control of active site proximity. *ACS Catalysis* **2017**, *7*, 6663–6674.

(101) Di Iorio, J. R.; Gounder, R. Controlling the Isolation and Pairing of Aluminum in Chabazite Zeolites Using Mixtures of Organic and Inorganic Structure-Directing Agents. *Chemistry of Materials* **2016**, *28*, 2236–2247.

(102) Bates, S. A.; Verma, A. A.; Paolucci, C.; Parekh, A. A.; Anggara, T.; Yezerets, A.; Schneider, W. F.; Miller, J. T.; Delgass, W. N.; Ribeiro, F. H. Identification of the active Cu site in standard selective catalytic reduction with ammonia on Cu-SSZ-13. *Journal of Catalysis* **2014**, *312*, 87–97.

(103) Bordiga, S.; Vitillo, J. G.; Ricchiardi, G.; Regli, L.; Cocina, D.; Zecchina, A.; Arstad, B.; Bjørgen, M.; Hafizovic, J.; Lillerud, K. F. Interaction of hydrogen with MOF-5. *Journal of Physical Chemistry B* **2005**, *109*, 18237–18242.

(104) Smith, L. J.; Davidson, A.; Cheetham, A. K. A neutron diffraction and infrared spectroscopy study of the acid form of the aluminosilicate zeolite, chabazite (H-SSZ-13). *Catalysis Letters* **1997**, *49*, 143–146.

(105) Lee, J.; Ryou, Y.; Hwang, S.; Kim, Y.; Cho, S. J.; Lee, H.; Kim, C. H.; Kim, D. H. Comparative study of the mobility of Pd species in SSZ-13 and ZSM-5, and its implication for their activity as passive NO : X adsorbers (PNAs) after hydro-thermal aging. *Catalysis Science and Technology* **2019**, *9*, 163–173.

(106) Aylor, A. W.; Lobree, L. J.; Reimer, J. A.; Bell, A. T. Investigations of the dispersion of Pd in H-ZSM-5. *Journal of Catalysis* **1997**, *172*, 453–462.

(107) Vu, A.; Luo, J.; Li, J.; Epling, W. S. Effects of CO on Pd/BEA Passive NOx Adsorbers. *Catalysis Letters* **2017**, *147*, 745–750.

(108) Moliner, M.; Corma, A. From metal-supported oxides to well-defined metal site zeolites: The next generation of passive NO x adsorbers for low-temperature control of emissions from diesel engines. *Reaction Chemistry and Engineering* **2019**, *4*, 223–234.

(109) Gu, Y.; Epling, W. S. Passive NOx adsorber: An overview of catalyst performance and reaction chemistry. *Applied Catalysis A: General* **2019**, *570*, 1–14.

(110) Ruhela, R.; Tomar, B. S.; Singh, A. K.; Hubli, R. C.; Suri, A. K. Investigation of the extraction complexes of palladium(ii) with novel thiodiglycolamide and dithiodiglycolamide ligands by EXAFS and computational methods. *Dalton Transactions* **2013**, *42*, 7085–7091.

(111) Vanelderen, P.; Vancauwenbergh, J.; Sels, B. F.; Schoonheydt, R. A. Coordination chemistry and reactivity of copper in zeolites. *Coordination Chemistry Reviews* **2013**, *257*, 483–494.

(112) Göltl, F.; Hafner, J. Structure and properties of metal-exchanged zeolites studied using gradient-corrected and hybrid functionals. III. Energetics and vibrational spectroscopy of adsorbates. *Journal of Chemical Physics* **2012**, *136*, 64501.

(113) Anggara, T.; Paolucci, C.; Schneider, W. F. Periodic DFT Characterization of NOx Adsorption in Cu-Exchanged SSZ-13 Zeolite Catalysts. *Journal of Physical Chemistry C* **2016**, *120*, 27934–27943.

(114) Paolucci, C.; Di Iorio, J. R.; Ribeiro, F. H.; Gounder, R.; Schneider, W. F. In *Advances in Catalysis*, Song, C., Ed.; Academic Press: 2016; Vol. 59, pp 1–107.

(115) Negri, C.; Borfecchia, E.; Cutini, M.; Lomachenko, K. A.; Janssens, T. V.; Berlier, G.; Bordiga, S. Evidence of Mixed-Ligand Complexes in Cu−CHA by Reaction of Cu Nitrates with NO/NH3 at Low Temperature. *ChemCatChem* **2019**, *11*, 3828–3838.

(116) Bulánek, R.; Drobná, H.; Nachtigall, P.; Rubeš, M.; Bludský, O. On the site-specificity of polycarbonyl complexes in Cu/zeolites: Combined experimental and DFT study. *Physical Chemistry Chemical Physics* **2006**, *8*, 5535–5542.

(117) Tuma, C.; Sauer, J. A hybrid MP2/planewave-DFT scheme for large chemical systems: Proton jumps in zeolites. *Chemical Physics Letters* **2004**, *387*, 388–394.

(118) Tuma, C.; Sauer, J. Treating dispersion effects in extended systems by hybrid MP2:DFT calculations - Protonation of isobutene in zeolite ferrierite. *Physical Chemistry Chemical Physics* **2006**, *8*, 3955–3965.

(119) Hansen, N.; Kerber, T.; Sauer, J.; Bell, A. T.; Keil, F. J. Quantum chemical modeling of benzene ethylation over H-ZSM-5 approaching chemical accuracy: A hybrid MP2:DFT study. *Journal of the American Chemical Society* **2010**, *132*, 11525–11538.

(120) Svelle, S.; Tuma, C.; Rozanska, X.; Kerber, T.; Sauer, J. Quantum chemical modeling of zeolite-catalyzed methylation reactions: Toward chemical accuracy for barriers. *Journal of the American Chemical Society* **2009**, *131*, 816–825.

(121) Bludský, O.; Rubeš, M.; Soldán, P.; Nachtigall, P. Investigation of the benzene-dimer potential energy surface: DFT/CCSD(T) correction scheme. *Journal of Chemical Physics* **2008**, *128*, 114102.

(122) Goncalves, T. J.; Plessow, P. N.; Studt, F. On the Accuracy of Density Functional Theory in Zeolite Catalysis. *ChemCatChem* **2019**, *11*, 4368–4376.

(123) Chen, J.; Chan, B.; Shao, Y.; Ho, J. How accurate are approximate quantum chemical methods at modelling solute-solvent interactions in solvated clusters? *Physical Chemistry Chemical Physics* **2020**, *22*, 3855–3866.

(124) Grein, F. Ground and low-lying excited C2v States of FeO2 - A challenge to computational methods. *International Journal of Quantum Chemistry* **2009**, *109*, 549–558.

(125) Hait, D.; Tubman, N. M.; Levine, D. S.; Whaley, K. B.; Head-Gordon, M. What Levels of Coupled Cluster Theory Are Appropriate for Transition Metal

Systems? A Study Using Near-Exact Quantum Chemical Values for 3d Transition Metal Binary Compounds. *Journal of Chemical Theory and Computation* **2019**, *15*, 5370–5385.

(126) Weaver, M. N.; Merz, K. M. Assessment of the CCSD and CCSD(T) coupled-cluster methods in calculating heats of formation for Cu complexes. *Molecular Physics* **2009**, *107*, 1251–1259.

(127) Nielsen, I. M.; Allendorf, M. D. High-level ab initio thermochemical data for halides of chromium, manganese, and iron. *Journal of Physical Chemistry A* **2005**, *109*, 928–933.

(128) Liu, F.; Kulik, H. J. Impact of Approximate DFT Density Delocalization Error on Potential Energy Surfaces in Transition Metal Chemistry. *Journal of Chemical Theory and Computation* **2020**, *16*, 264–277.

(129) National Institute of Standards and Technology Computational Chemistry Comparison and Benchmark DataBase - Standard Reference Database 101. **2016**.

(130) Irikura, K. K. Experimental vibrational zero-point energies: Diatomic molecules. *Journal of Physical and Chemical Reference Data* **2007**, *36*, 389–397.

(131) Carpenter, J. E.; Weinhold, F. Analysis of the geometry of the hydroxymethyl radical by the "different hybrids for different spins" natural bond orbital procedure. *Journal of Molecular Structure: THEOCHEM* **1988**, *169*, 41–62.

(132) Foster, J. P.; Weinhold, F. Natural Hybrid Orbitals. *Journal of the American Chemical Society* **1980**, *102*, 7211–7218.

(133) Reed, A. E.; Weinhold, F. Natural bond orbital analysis of near-Hartree-Fock water dimer. *The Journal of Chemical Physics* **1983**, *78*, 4066–4073.

(134) Reed, A. E.; Weinstock, R. B.; Weinhold, F. Natural population analysis. *The Journal of Chemical Physics* **1985**, *83*, 735–746.

(135) Reed, A. E.; Weinhold, F. Natural localized molecular orbitals. *The Journal of Chemical Physics* **1985**, *83*, 1736–1740.

(136) Reed, A. E.; Curtiss, L. A.; Weinhold, F. Intermolecular Interactions from a Natural Bond Orbital, Donor—Acceptor Viewpoint. *Chemical Reviews* **1988**, *88*, 899–926.

(137) Weinhold, F.; Carpenter, J. E. In *The Structure of Small Molecules and Ions*, Naaman, R., Vager, Z., Eds.; Springer US: Boston, MA, 1988, pp 227–236.

(138) Pommier, B.; Gelin, P. Infrared and volumetric study of NO adsorption on Pd-H-ZSM-5. *Physical Chemistry Chemical Physics* **2001**, *3*, 1138–1143.

(139) Hadjiivanov, K.; Saussey, J.; Freysz, J. L.; Lavalley, J. C. FT-IR study of NO + O2 co-adsorption on H-ZSM-5: Re-assignment of the 2133 cm-1 band to NO+ species. *Catalysis Letters* **1998**, *52*, 103–108.

(140) Villamaina, R.; Iacobone, U.; Nova, I.; Ruggeri, M. P.; Collier, J.; Thompsett, D.; Tronconi, E. Low-T CO Oxidation over Cu−CHA Catalysts in Presence of NH 3 : Probing the Mobility of Cu II Ions and the Role of Multinuclear Cu II Species. *ChemCatChem* **2020**, *12*, 3795–3795.

(141) Chakarova, K.; Ivanova, E.; Hadjiivanov, K.; Klissurski, D.; Knözinger, H. Co-ordination chemistry of palladium cations in Pd-H-ZSM-5 as revealed by FTIR spectra of adsorbed and co-adsorbed probe molecules (CO and NO). *Physical Chemistry Chemical Physics* **2004**, *6*, 3702–3709.

(142) Jacobs, P. A.; Von Ballmoos, R. Framework hydroxyl groups of H-ZSM-5 zeolites. *Journal of Physical Chemistry* **1982**, *86*, 3050–3052.

(143) Yokoi, T.; Mochizuki, H.; Biligetu, T.; Wang, Y.; Tatsumi, T. Unique Al distribution in the MFI framework and its impact on catalytic properties. *Chemistry Letters* **2017**, *46*, 798–800.

(144) Bortnovsky, O.; Sobalík, Z.; Wichterlová, B. Exchange of Co(II) ions in H-BEA zeolites: Identification of aliminum pairs in the zeolite framework. *Microporous and Mesoporous Materials* **2001**, *46*, 265–275.

(145) Dědeček, J.; Kaucký, D.; Wichterlová, B.; Gonsiorová, O. Co2+ ions as probes of Al distribution in the framework of zeolites. ZSM-5 study. *Physical Chemistry Chemical Physics* **2002**, *4*, 5406–5413.

(146) Kresse, G.; Furthmüller, J. Efficient iterative schemes for ab initio total-energy calculations using a plane-wave basis set. *Physical Review B - Condensed Matter and Materials Physics* **1996**, *54*, 11169–11186.

(147) Perdew, J. P.; Wang, Y. Accurate and simple analytic representation of the electron-gas correlation energy. *Physical Review B* **1992**, *45*, 13244–13249.

(148) Grimme, S.; Antony, J.; Ehrlich, S.; Krieg, H. A consistent and accurate ab initio parametrization of density functional dispersion correction (DFT-D) for the 94 elements H-Pu. *Journal of Chemical Physics* **2010**, *132*, 154104.

(149) Grimme, S.; Ehrlich, S.; Goerigk, L. Effect of the damping function in dispersion corrected density functional theory. *Journal of Computational Chemistry* **2011**, *32*, 1456–1465.

(150) Heyd, J.; Scuseria, G. E.; Ernzerhof, M. Hybrid functionals based on a screened Coulomb potential. *Journal of Chemical Physics* **2003**, *118*, 8207–8215.

(151) Heyd, J.; Scuseria, G. E. Efficient hybrid density functional calculations in solids: Assessment of the Heyd-Scuseria-Ernzerhof screened Coulomb hybrid functional. *Journal of Chemical Physics* **2004**, *121*, 1187–1192.

(152) Heyd, J.; Scuseria, G. E.; Ernzerhof, M. Erratum: Hybrid functionals based on a screened Coulomb potential (Journal of Chemical Physics (2003) 118 (8207)). *Journal of Chemical Physics* **2006**, *124*, 219906.

(153) Krukau, A. V.; Vydrov, O. A.; Izmaylov, A. F.; Scuseria, G. E. Influence of the exchange screening parameter on the performance of screened hybrid functionals. *Journal of Chemical Physics* **2006**, *125*, 224106.

(154) Blöchl, P. E. Projector augmented-wave method. *Physical Review B* **1994**, *50*, 17953–17979.

(155) Joubert, D. From ultrasoft pseudopotentials to the projector augmented-wave method. *Physical Review B - Condensed Matter and Materials Physics* **1999**, *59*, 1758–1775.

(156) Orville-Thomas, W., *Atoms in Molecules — a Quantum Theory*; 1-3; Oxford : Clarendon press: 1996; Vol. 360, p 175.

(157) Tang, W.; Sanville, E.; Henkelman, G. A grid-based Bader analysis algorithm without lattice bias. *Journal of Physics Condensed Matter* **2009**, *21*, 84204.

(158) Sanville, E.; Kenny, S. D.; Smith, R.; Henkelman, G. Improved grid-based algorithm for Bader charge allocation. *Journal of Computational Chemistry* **2007**, *28*, 899–908.

(159) Henkelman, G.; Arnaldsson, A.; Jónsson, H. A fast and robust algorithm for Bader decomposition of charge density. *Computational Materials Science* **2006**, *36*, 354–360.

(160) Yu, M.; Trinkle, D. R. Accurate and efficient algorithm for Bader charge integration. *Journal of Chemical Physics* **2011**, *134*, 64111.

(161) Bray, J. M.; Schneider, W. F. In *Computational Catalysis*, 2014, pp 59–115.

(162) Penninger, M. W.; Kim, C. H.; Thompson, L. T.; Schneider, W. F. DFT Analysis of NO Oxidation Intermediates on Undoped and Doped LaCoO3 Perovskite. *Journal of Physical Chemistry C* **2015**, *119*, 20488–20494.

(163) Davies, R. O., *Molecular Thermodynamics*; 8; University Science Books: Sausalito, California, 1966; Vol. 17, pp 306–306.

(164) Göltl, F.; Sautet, P.; Hermans, I. Can Dynamics Be Responsible for the Complex Multipeak Infrared Spectra of NO Adsorbed to Copper(II) Sites in Zeolites? *Angewandte Chemie - International Edition* **2015**, *54*, 7799–7804.

(165) Göltl, F.; Sautet, P.; Hermans, I. The impact of finite temperature on the coordination of Cu cations in the zeolite SSZ-13. *Catalysis Today* **2016**, *267*, 41–46.

(166) Paolucci, C.; Verma, A. A.; Bates, S. A.; Kispersky, V. F.; Miller, J. T.; Gounder, R.; Delgass, W. N.; Ribeiro, F. H.; Schneider, W. F. Isolation of the copper redox steps in the standard selective catalytic reduction on Cu-SSZ-13. *Angewandte Chemie - International Edition* **2014**, *53*, 11828–11833.

(167) Piccini, G.; Sauer, J. Quantum chemical free energies: Structure optimization and vibrational frequencies in normal modes. *Journal of Chemical Theory and Computation* **2013**, *9*, 5038–5045.

(168) Dauenhauer, P. J.; Abdelrahman, O. A. A Universal Descriptor for the Entropy of Adsorbed Molecules in Confined Spaces. *ACS Central Science* **2018**, *4*, 1235–1243.

(169) Jørgensen, M.; Chen, L.; Grönbeck, H. Monte Carlo Potential Energy Sampling for Molecular Entropy in Zeolites. *Journal of Physical Chemistry C* **2018**, *122*, 20351–20357.

(170) Campbell, C. T.; Sellers, J. R. The entropies of adsorbed molecules. *Journal of the American Chemical Society* **2012**, *134*, 18109–18115.

(171) Li, H.; Paolucci, C.; Schneider, W. F. Zeolite Adsorption Free Energies from ab Initio Potentials of Mean Force. *Journal of Chemical Theory and Computation* **2018**, *14*, 929–938.

(172) Frisch, M. J. et al., *Gaussian 16*, Wallingford, CT, 2016, Gaussian 16, Revision C.01, Gaussian, Inc., Wallin.

(173) Lee, C.; Yang, W.; Parr, R. G. Development of the Colle-Salvetti correlation-energy formula into a functional of the electron density. *Physical Review B* **1988**, *37*, 785–789.

(174) Becke, A. D. Density-functional thermochemistry. III. The role of exact exchange. *The Journal of Chemical Physics* **1993**, *98*, 5648–5652.

(175) Kendall, R. A.; Dunning, T. H.; Harrison, R. J. Electron affinities of the first-row atoms revisited. Systematic basis sets and wave functions. *The Journal of Chemical Physics* **1992**, *96*, 6796–6806.

(176) Woon, D. E.; Dunning, T. H. Gaussian basis sets for use in correlated molecular calculations. III. The atoms aluminum through argon. *The Journal of Chemical Physics* **1993**, *98*, 1358–1371.

(177) Glendenning, E.; Reed, A.; Carpenter, J.; Weinhold, F. NBO; Version 3.1; 2001. *Google Scholar There is no corresponding record for this reference.*

(178) Dennington, R.; Keith, T.; Millam, J., *GaussView, Version 5.* 2009, Semichem Inc.

(179) Kammert, J. D.; Brezicki, G.; Acevedo-Esteves, R.; Stavitski, E.; Davis, R. J. High-throughput operando -ready X-ray absorption spectroscopy flow reactor cell for powder samples. *Review of Scientific Instruments* **2020**, *91*, 13107.

(180) Datye, A. K.; Guo, H. Single atom catalysis poised to transition from an academic curiosity to an industrially relevant technology. *Nature Communications* **2021**, *12*, 1–3.

(181) Liu, L.; Corma, A. Confining isolated atoms and clusters in crystalline porous materials for catalysis. *Nature Reviews Materials* **2021**, *6*, 244–263.

(182) Li, Z.; Ji, S.; Liu, Y.; Cao, X.; Tian, S.; Chen, Y.; Niu, Z.; Li, Y. Well-Defined Materials for Heterogeneous Catalysis: From Nanoparticles to Isolated Single-Atom Sites. *Chemical Reviews* **2020**, *120*, 623–682.

(183) Liu, L.; Corma, A. Metal Catalysts for Heterogeneous Catalysis: From Single Atoms to Nanoclusters and Nanoparticles, 2018.

(184) Wang, A.; Li, J.; Zhang, T. Heterogeneous single-atom catalysis. *Nature Reviews Chemistry* **2018**, *2*, 65–81.

(185) Goodman, E. D.; Johnston-Peck, A. C.; Dietze, E. M.; Wrasman, C. J.; Hoffman, A. S.; Abild-Pedersen, F.; Bare, S. R.; Plessow, P. N.; Cargnello, M. Catalyst deactivation via decomposition into single atoms and the role of metal loading. *Nature Catalysis* **2019**, *2*, 748–755.

(186) Nie, L.; Mei, D.; Xiong, H.; Peng, B.; Ren, Z.; Hernandez, X. I. P.; DeLaRiva, A.; Wang, M.; Engelhard, M. H.; Kovarik, L.; Datye, A. K.; Wang, Y. Acti-

vation of surface lattice oxygen in single-atom Pt/CeO2 for low-temperature CO oxidation. *Science* **2017**, *358*, 1419–1423.

(187) Fernández, E.; Liu, L.; Boronat, M.; Arenal, R.; Concepcion, P.; Corma, A. Low-Temperature Catalytic NO Reduction with CO by Subnanometric Pt Clusters. *ACS Catalysis* **2019**, *9*, 11530–11541.

(188) Yuan, K.; Guo, Y.; Huang, L.; Zhou, L.; Yin, H. J.; Liu, H.; Yan, C. H.; Zhang, Y. W. Tunable Electronic Metal-Support Interactions on Ceria-Supported Noble-Metal Nanocatalysts in Controlling the Low-Temperature CO Oxidation Activity. *Inorganic Chemistry* **2021**, *60*, 4207–4217.

(189) Jones, J.; Xiong, H.; DeLaRiva, A. T.; Peterson, E. J.; Pham, H.; Challa, S. R.; Qi, G.; Oh, S.; Wiebenga, M. H.; Hernández, X. I. P.; Wang, Y.; Datye, A. K. Thermally stable single-atom platinum-on-ceria catalysts via atom trapping. *Science* **2016**, *353*, 150–154.

(190) Jeong, H.; Bae, J.; Han, J. W.; Lee, H. Promoting effects of hydrothermal treatment on the activity and durability of Pd/CeO2 catalysts for CO oxidation. *ACS Catalysis* **2017**, *7*, 7097–7105.

(191) Xiong, H.; Lin, S.; Goetze, J.; Pletcher, P.; Guo, H.; Kovarik, L.; Artyushkova, K.; Weckhuysen, B. M.; Datye, A. K. Thermally Stable and Regenerable Platinum–Tin Clusters for Propane Dehydrogenation Prepared by Atom Trapping on Ceria. *Angewandte Chemie - International Edition* **2017**, *56*, 8986–8991.

(192) Alcala, R.; DeLaRiva, A.; Peterson, E. J.; Benavidez, A.; Garcia-Vargas, C. E.; Jiang, D.; Pereira-Hernández, X. I.; Brongersma, H. H.; ter Veen, R.; Staněk, J.; Miller, J. T.; Wang, Y.; Datye, A. Atomically Dispersed Dopants for Sta-

bilizing Ceria Surface Area. *Applied Catalysis B: Environmental* **2021**, *284*, 119722.

(193) Yu, W. Z.; Wang, W. W.; Li, S. Q.; Fu, X. P.; Wang, X.; Wu, K.; Si, R.; Ma, C.; Jia, C. J.; Yan, C. H. Construction of Active Site in a Sintered Copper-Ceria Nanorod Catalyst. *Journal of the American Chemical Society* **2019**, *141*, 17548–17557.

(194) Carter, J. H.; Liu, X.; He, Q.; Althahban, S.; Nowicka, E.; Freakley, S. J.; Niu, L.; Morgan, D. J.; Li, Y.; Niemantsverdriet, J. W.; Golunski, S.; Kiely, C. J.; Hutchings, G. J. Activation and Deactivation of Gold/Ceria–Zirconia in the Low-Temperature Water–Gas Shift Reaction. *Angewandte Chemie - International Edition* **2017**, *56*, 16037–16041.

(195) Deng, W.; Frenkel, A. I.; Si, R.; Flytzani-Stephanop, M. Reaction-relevant gold structures in the low temperature water-gas shift reaction on Au-CeO2. *Journal of Physical Chemistry C* **2008**, *112*, 12834–12840.

(196) Malta, G.; Kondrat, S. A.; Freakley, S. J.; Davies, C. J.; Lu, L.; Dawson, S.; Thetford, A.; Gibson, E. K.; Morgan, D. J.; Jones, W.; Wells, P. P.; Johnston, P.; Catlow, C. R. A.; Kiely, C. J.; Hutchings, G. J. Identification of single-site gold catalysis in acetylene hydrochlorination. *Science* **2017**, *355*, DOI: 10.1126/science.aal3439.

(197) Malta, G.; Kondrat, S. A.; Freakley, S. J.; Davies, C. J.; Dawson, S.; Liu, X.; Lu, L.; Dymkowski, K.; Fernandez-Alonso, F.; Mukhopadhyay, S.; Gibson, E. K.; Wells, P. P.; Parker, S. F.; Kiely, C. J.; Hutchings, G. J. Deactivation of a Single-Site Gold-on-Carbon Acetylene Hydrochlorination Catalyst: An X-ray Absorption and Inelastic Neutron Scattering Study. *ACS Catalysis* **2018**, *8*, 8493–8505.

(198) Shan, J.; Li, M.; Allard, L. F.; Lee, S.; Flytzani-Stephanopoulos, M. Mild oxidation of methane to methanol or acetic acid on supported isolated rhodium catalysts. *Nature* **2017**, *551*, 605–608.

(199) Hansen, T. W.; Delariva, A. T.; Challa, S. R.; Datye, A. K. Sintering of catalytic nanoparticles: Particle migration or ostwald ripening? *Accounts of Chemical Research* **2013**, *46*, 1720–1730.

(200) Xiong, H.; Datye, A. K.; Wang, Y. Thermally Stable Single-Atom Heterogeneous Catalysts. *Advanced Materials* **2021**, *33*, 2004319.

(201) Datye, A. K. Dispersing nanoparticles into single atoms. *Nature Nanotechnology* **2019**, *14*, 817–818.

(202) Serna, P.; Rodríguez-Fernández, A.; Yacob, S.; Kliewer, C.; Moliner, M.; Corma, A. Single-Site vs. Cluster Catalysis in High Temperature Oxidations. *Angewandte Chemie* **2021**, *133*, 16090–16098.

(203) Fang, C. Y.; Zhang, S.; Hu, Y.; Vasiliu, M.; Perez-Aguilar, J. E.; Conley, E. T.; Dixon, D. A.; Chen, C. Y.; Gates, B. C. Reversible Metal Aggregation and Redispersion Driven by the Catalytic Water Gas Shift Half-Reactions: Interconversion of Single-Site Rhodium Complexes and Tetrarhodium Clusters in Zeolite HY. *ACS Catalysis* **2019**, *9*, 3311–3321.

(204) Ouyang, R.; Liu, J. X.; Li, W. X. Atomistic theory of ostwald ripening and disintegration of supported metal particles under reaction conditions. *Journal of the American Chemical Society* **2013**, *135*, 1760–1771.

(205) Bergmann, A.; Roldan Cuenya, B. Operando Insights into Nanoparticle Transformations during Catalysis. *ACS Catalysis* **2019**, *9*, 10020–10043.

(206) Wei, S. et al. Direct observation of noble metal nanoparticles transforming to thermally stable single atoms. *Nature Nanotechnology* **2018**, *13*, 856–861.

(207) Parkinson, G. S.; Novotny, Z.; Argentero, G.; Schmid, M.; Pavelec, J.; Kosak, R.; Blaha, P.; Diebold, U. Carbon monoxide-induced adatom sintering in a Pd-Fe3 O 4 model catalyst. *Nature Materials* **2013**, *12*, 724–728.

(208) Dessal, C.; Len, T.; Morfin, F.; Rousset, J. L.; Aouine, M.; Afanasiev, P.; Piccolo, L. Dynamics of Single Pt Atoms on Alumina during CO Oxidation Monitored by Operando X-ray and Infrared Spectroscopies. *ACS Catalysis* **2019**, *9*, 5752–5759.

(209) Muravev, V.; Spezzati, G.; Su, Y. Q.; Parastaev, A.; Chiang, F. K.; Longo, A.; Escudero, C.; Kosinov, N.; Hensen, E. J. Interface dynamics of Pd–CeO2 single-atom catalysts during CO oxidation. *Nature Catalysis* **2021**, *4*, 469–478.

(210) Jin, M.; Park, J. N.; Shon, J. K.; Kim, J. H.; Li, Z.; Park, Y. K.; Kim, J. M. Low temperature CO oxidation over Pd catalysts supported on highly ordered mesoporous metal oxides. *Catalysis Today* **2012**, *185*, 183–190.

(211) Navlani-García, M.; Miguel-García, I.; Berenguer-Murcia, Á.; Lozano-Castelló, D.; Cazorla-Amorós, D.; Yamashita, H. Pd/zeolite-based catalysts for the preferential CO oxidation reaction: Ion-exchange, Si/Al and structure effect. *Catalysis Science and Technology* **2016**, *6*, 2623–2632.

(212) Imbao, J.; Van Bokhoven, J. A.; Nachtegaal, M. Optimization of a heterogeneous Pd-Cu/zeolite y Wacker catalyst for ethylene oxidation. *Chemical Communications* **2020**, *56*, 1377–1380.

(213) Imbao, J.; Van Bokhoven, J. A.; Nachtegaal, M. On the Promotional and Inhibitory Effects of Water on Wacker-Type Ethylene Oxidation over Pd-Cu/Zeolite y. *ACS Catalysis* **2021**, *11*, 8684–8691.

(214) Chen, S.; Li, S.; You, R.; Guo, Z.; Wang, F.; Li, G.; Yuan, W.; Zhu, B.; Gao, Y.; Zhang, Z.; Yang, H.; Wang, Y. Elucidation of active sites for CH4 catalytic oxidation over Pd/CeO2 via tailoring metal−support interactions. *ACS Catalysis* **2021**, *11*, 5666–5677.

(215) Khivantsev, K.; Jaegers, N. R.; Kovarik, L.; Wang, M.; Hu, J. Z.; Wang, Y.; Derewinski, M. A.; Szanyi, J. The superior hydrothermal stability of Pd/SSZ-39 in low temperature passive NOx adsorption (PNA) and methane combustion. *Applied Catalysis B: Environmental* **2021**, *280*, 119449.

(216) Tang, X.; Lou, Y.; Zhao, R.; Tang, B.; Guo, W.; Guo, Y.; Zhan, W.; Jia, Y.; Wang, L.; Dai, S.; Guo, Y. Confinement of subnanometric PdCo bimetallic oxide clusters in zeolites for methane complete oxidation. *Chemical Engineering Journal* **2021**, *418*, 129398.

(217) Li, T.; Beck, A.; Krumeich, F.; Artiglia, L.; Ghosalya, M. K.; Roger, M.; Ferri, D.; Kröcher, O.; Sushkevich, V.; Safonova, O. V.; van Bokhoven, J. A. Stable Palladium Oxide Clusters Encapsulated in Silicalite-1 for Complete Methane Oxidation. *ACS Catalysis* **2021**, *11*, 7371–7382.

(218) Guo, Y.; Qi, H.; Su, Y.; Jiang, Q.; Cui, Y. T.; Li, L.; Qiao, B. High Performance of Single-atom Catalyst Pd1/MgO for Semi-hydrogenation of Acetylene to Ethylene in Excess Ethylene. *ChemNanoMat* **2021**, *7*, 526–529.

(219) Zhang, L.; Zhou, M.; Wang, A.; Zhang, T. Selective Hydrogenation over Supported Metal Catalysts: From Nanoparticles to Single Atoms. *Chemical Reviews* **2020**, *120*, 683–733.

(220) Huang, W.; McCormick, J. R.; Lobo, R. F.; Chen, J. G. Selective hydrogenation of acetylene in the presence of ethylene on zeolite-supported bimetallic catalysts. *Journal of Catalysis* **2007**, *246*, 40–51.

(221) Villamaina, R.; Iacobone, U.; Nova, I.; Tronconi, E.; Ruggeri, M. P.; Mantarosie, L.; Collier, J.; Thompsett, D. Mechanistic insight in NO trapping on Pd/Chabazite systems for the low-temperature NOx removal from Diesel exhausts. *Applied Catalysis B: Environmental* **2021**, *284*, 119724.

(222) Ryou, Y. S.; Lee, J.; Lee, H.; Kim, C. H.; Kim, D. H. Low temperature NO adsorption over hydrothermally aged Pd/CeO2 for cold start application. *Catalysis Today* **2018**, *307*, 93–101.

(223) Cui, Y.; Zhu Chen, J.; Peng, B.; Kovarik, L.; Devaraj, A.; Li, Z.; Ma, T.; Wang, Y.; Szanyi, J.; Miller, J. T.; Wang, Y.; Gao, F. Onset of High Methane Combustion Rates over Supported Palladium Catalysts: From Isolated Pd Cations to PdO Nanoparticles. *Journal of the American Chemical Society* **2021**, *1*, 396–408.

(224) Peterson, E. J.; DeLaRiva, A. T.; Lin, S.; Johnson, R. S.; Guo, H.; Miller, J. T.; Kwak, J. H.; Peden, C. H.; Kiefer, B.; Allard, L. F.; Ribeiro, F. H.; Datye, A. K. Low-temperature carbon monoxide oxidation catalysed by regenerable atomically dispersed palladium on alumina. *Nature Communications* **2014**, *5*, 1–11.

(225) Li, J.; Li, M.; Li, J.; Wang, S.; Li, G.; Liu., X. Hydrodechlorination and deep hydrogenation on single-palladium-atom-based heterogeneous catalysts. *Applied Catalysis B: Environmental* **2021**, *282*, 119518.

(226) Ryou, Y. S.; Lee, J.; Kim, Y.; Hwang, S.; Lee, H.; Kim, C. H.; Kim, D. H. Effect of reduction treatments (H2 vs. CO) on the NO adsorption ability and

the physicochemical properties of Pd/SSZ-13 passive NOx adsorber for cold start application. *Applied Catalysis A: General* **2019**, *569*, 28–34.

(227) Lee, J.; Kim, Y.; Hwang, S.; Lee, E.; Lee, H.; Kim, C. H.; Kim, D. H. Deactivation of Pd/Zeolites passive NOx adsorber induced by NO and H2O: Comparative study of Pd/ZSM-5 and Pd/SSZ-13. *Catalysis Today* **2021**, *360*, 350–355.

(228) Goldsmith, B. R.; Sanderson, E. D.; Ouyang, R.; Li, W. X. CO- and NO-induced disintegration and redispersion of three-way catalysts rhodium, palladium, and platinum: An ab initio thermodynamics study. *Journal of Physical Chemistry C* **2014**, *118*, 9588–9597.

(229) Paredis, K.; Ono, L. K.; Behafarid, F.; Zhang, Z.; Yang, J. C.; Frenkel, A. I.; Cuenya, B. R. Evolution of the structure and chemical state of Pd nanoparticles during the in situ catalytic reduction of NO with H2. *Journal of the American Chemical Society* **2011**, *133*, 13455–13464.

(230) Newton, M. A.; Belver-Coldeira, C.; Martínez-Arias, A.; Fernández-García, M. Dynamic in situ observation of rapid size and shape change of supported Pd nanoparticles during CO/NO cycling. *Nature Materials* **2007**, *6*, 528–532.

(231) Yasumura, S.; Ide, H.; Ueda, T.; Jing, Y.; Liu, C.; Kon, K.; Toyao, T.; Maeno, Z.; Shimizu, K. I. Transformation of Bulk Pd to Pd Cations in Small-Pore CHA Zeolites Facilitated by NO. *Journal of the American Chemical Society* **2021**, *1*, 201–211.

(232) Pereira-Hernández, X. I.; DeLaRiva, A.; Muravev, V.; Kunwar, D.; Xiong, H.; Sudduth, B.; Engelhard, M.; Kovarik, L.; Hensen, E. J.; Wang, Y.; Datye, A. K. Tuning Pt-CeO 2 interactions by high-temperature vapor-phase synthe-

sis for improved reducibility of lattice oxygen. *Nature Communications* **2019**, *10*, 1–10.

(233) Kunwar, D. et al. Stabilizing High Metal Loadings of Thermally Stable Platinum Single Atoms on an Industrial Catalyst Support. *ACS Catalysis* **2019**, *9*, 3978–3990.

(234) Liu, K. et al. Strong metal-support interaction promoted scalable production of thermally stable single-atom catalysts. *Nature Communications* **2020**, *11*, 1–9.

(235) Li, Z.; Zhang, M.; Zhang, L.; Dong, X.; Leng, L.; Horton, J. H.; Wang, J. Engineering the atomic interface of porous ceria nanorod with single palladium atoms for hydrodehalogenation reaction. *Nano Research* **2022**, *15*, 1338–1346.

(236) Zhu, S.; Wang, H.; Wan, K.; Guo, L. J.; He, T.; Shi, X. Water-Gas Shift Reaction on Titania-Supported Single-Metal-Atom Catalysts: The Role of Cation (Ti) and Oxygen Vacancy. *Journal of Physical Chemistry C* **2021**, *125*, 8620–8629.

(237) Petrov, A. W.; Ferri, D.; Kröcher, O.; Van Bokhoven, J. A. Design of Stable Palladium-Based Zeolite Catalysts for Complete Methane Oxidation by Postsynthesis Zeolite Modification. *ACS Catalysis* **2019**, *9*, 2303–2312.

(238) Wen, B.; Sun, Q.; Sachtler, W. M. Function of Pdn0 cluster, Pd2+(oxo-) ions, and PdO clusters in the catalytic reduction of NO with methane over Pd/MFI catalysts. *Journal of Catalysis* **2001**, *204*, 314–323.

(239) Okumura, K.; Amano, J.; Yasunobu, N.; Niwa, M. X-ray Absorption Fine Structure Study of the Formation of the Highly Dispersed PdO over ZSM-5

and the Structural Change of Pd Induced by Adsorption of NO. *Journal of Physical Chemistry B* **2000**, *104*, 1050–1057.

(240) Moliner, M.; Gabay, J.; Kliewer, C.; Serna, P.; Corma, A. Trapping of Metal Atoms and Metal Clusters by Chabazite under Severe Redox Stress. *ACS Catalysis* **2018**, *8*, 9520–9528.

(241) Bergeret, G.; Gallezot, P.; Imelik, B. X-ray study of the activation, reduction, and reoxidation of palladium in Y-type zeolites. *Journal of Physical Chemistry* **1981**, *85*, 411–416.

(242) Van der Mynsbrugge, J.; Head-Gordon, M.; Bell, A. T. Computational modeling predicts the stability of both Pd+and Pd2+ion-exchanged into H-CHA. *Journal of Materials Chemistry A* **2021**, *9*, 2161–2174.

(243) Michalik, J.; Heming, M.; Kevan, L. Trivalent and monovalent palladium cations in PdNa-X zeolite: Electron spin resonance and electron spin echo modulation spectroscopic studies. *The Journal of Physical Chemistry* **1986**, *90*, 2132–2136.

(244) Gandhi, S. N.; Lei, G. D.; Sachtler, W. M. Identification of Pd3+ ions in zeolite L by temperature programmed reduction and electron paramagnetic resonance spectroscopy. *Catalysis Letters* **1993**, *17*, 117–126.

(245) Homeyer, S. T.; Sachtler, W. M. Oxidative redispersion of palladium and formation of PdO particles in NaY. An Application of High Precision TPR. *Applied Catalysis* **1989**, *54*, 189–202.

(246) Jain, A.; Ong, S. P.; Hautier, G.; Chen, W.; Richards, W. D.; Dacek, S.; Cholia, S.; Gunter, D.; Skinner, D.; Ceder, G.; Persson, K. A. Commentary:

The materials project: A materials genome approach to accelerating materials innovation. *APL Materials* **2013**, *1*, 011002.

(247) Mandal, K.; Gu, Y.; Westendorff, K. S.; Li, S.; Pihl, J. A.; Grabow, L. C.; Epling, W. S.; Paolucci, C. Condition-Dependent Pd Speciation and NO Adsorption in Pd/Zeolites. *ACS Catalysis* **2020**, *10*, 12801–12818.

(248) Ong, S. P.; Richards, W. D.; Jain, A.; Hautier, G.; Kocher, M.; Cholia, S.; Gunter, D.; Chevrier, V. L.; Persson, K. A.; Ceder, G. Python Materials Genomics (pymatgen): A robust, open-source python library for materials analysis. *Computational Materials Science* **2013**, *68*, 314–319.

(249) Tran, R.; Xu, Z.; Radhakrishnan, B.; Winston, D.; Sun, W.; Persson, K. A.; Ong, S. P. Data Descriptor: Surface energies of elemental crystals. *Scientific Data* **2016**, *3*, 1–13.

(250) Sun, W.; Ceder, G. Efficient creation and convergence of surface slabs. *Surface Science* **2013**, *617*, 53–59.

(251) Sholl, D. S.; Steckel, J. A., *Density Functional Theory: A Practical Introduction*; Wiley: 2009, pp 1–238.

(252) Wulff, G. XXV. Zur Frage der Geschwindigkeit des Wachsthums und der Auflösung der Krystallflächen. *Zeitschrift für Kristallographie - Crystalline Materials* **1901**, *34*, 449–530.

(253) Campbell, C. T.; Mao, Z. Chemical Potential of Metal Atoms in Supported Nanoparticles: Dependence upon Particle Size and Support. *ACS Catalysis* **2017**, *7*, 8460–8466.

(254) Mao, Z.; Campbell, C. T. Predicting a Key Catalyst-Performance Descriptor for Supported Metal Nanoparticles: Metal Chemical Potential. *ACS Catalysis* **2021**, *11*, 8284–8291.

(255) Hemmingson, S. L.; Campbell, C. T. Trends in Adhesion Energies of Metal Nanoparticles on Oxide Surfaces: Understanding Support Effects in Catalysis and Nanotechnology. *ACS Nano* **2017**, *11*, 1196–1203.

(256) Campbell, C. T.; Sellers, J. R. Enthalpies and entropies of adsorption on well-defined oxide surfaces: Experimental measurements. *Chemical Reviews* **2013**, *113*, 4106–4135.

(257) Chen, M.; Schmidt, L. D. Morphology and composition of PtPd alloy crystallites on SiO2 in reactive atmospheres. *Journal of Catalysis* **1979**, *56*, 198–218.

(258) Carvill, B. T.; Lerner, B. A.; Zhang, Z. C.; Sachtler, W. M. Preparation of metal/zeolite catalysts: Formation of palladium aquocomplexes in the precursor of palladium-mordenite catalysts. *Journal of Catalysis* **1993**, *143*, 314–317.

(259) Lee, J.; Kim, J.; Kim, Y.; Hwang, S.; Lee, H.; Kim, C. H.; Kim, D. H. Improving NOx storage and CO oxidation abilities of Pd/SSZ-13 by increasing its hydrophobicity. *Applied Catalysis B: Environmental* **2020**, *277*, 119190.

(260) Chin, Y. H. C.; García-Diéguez, M.; Iglesia, E. Dynamics and thermodynamics of Pd-PdO phase transitions: Effects of pd cluster size and kinetic implications for catalytic methane combustion. *Journal of Physical Chemistry C* **2016**, *120*, 1446–1460.

(261) Yasumura, S.; Ueda, T.; Ide, H.; Otsubo, K.; Liu, C.; Tsunoji, N.; Toyao, T.; Maeno, Z.; Shimizu, K. I. Local structure and NO adsorption/desorption property of Pd2+cations at different paired Al sites in CHA zeolite. *Physical Chemistry Chemical Physics* **2021**, *23*, 22273–22282.

(262) Aljama, H. A.; Head-Gordon, M.; Bell, A. T. Assessing the stability of Pd-exchanged sites in zeolites with the aid of a high throughput quantum chemistry workflow. *Nature Communications* **2022**, *13*, DOI: 10.1038/s41467-022-29505-z.

(263) Li, X.; Wang, X.; Sadykov, I. I.; Palagin, D.; Safonova, O. V.; Li, J.; Beck, A.; Krumeich, F.; van Bokhoven, J. A.; Artiglia, L. Temperature and Reaction Environment Influence the Nature of Platinum Species Supported on Ceria. *ACS Catalysis* **2021**, *11*, 13041–13049.

(264) Li, X.; Wang, X.; Roy, K.; Van Bokhoven, J. A.; Artiglia, L. Role of Water on the Structure of Palladium for Complete Oxidation of Methane. *ACS Catalysis* **2020**, *10*, 5783–5792.

(265) Delariva, A. T.; Hansen, T. W.; Challa, S. R.; Datye, A. K. In situ transmission electron microscopy of catalyst sintering. *Journal of Catalysis* **2013**, *308*, 291–305.

(266) Castoldi, L.; Matarrese, R.; Morandi, S.; Ticali, P.; Lietti, L. Low-temperature Pd/FER NOx adsorbers: Operando FT-IR spectroscopy and performance analysis. *Catalysis Today* **2021**, *360*, 317–325.

(267) Wynblatt, P.; Gjostein, N. A. Particle growth in model supported metal catalysts-I. Theory. *Acta Metallurgica* **1976**, *24*, 1165–1174.

(268) Campbell, C. T.; Parker, S. C.; Starr, D. E. The effect of size-dependent nanoparticle energetics on catalyst sintering. *Science* **2002**, *298*, 811–814.

(269) Dietze, E. M.; Abild-Pedersen, F.; Plessow, P. N. Comparison of Sintering by Particle Migration and Ripening through First-Principles-Based Simulations. *Journal of Physical Chemistry C* **2018**, *122*, 26563–26569.

(270) Yang, F.; Chen, M. S.; Goodman, D. W. Sintering of Au particles supported on TiO 2(110) during CO oxidation. *Journal of Physical Chemistry C* **2009**, *113*, 254–260.

(271) Grillo, F.; Van Bui, H.; Moulijn, J. A.; Kreutzer, M. T.; Van Ommen, J. R. Understanding and Controlling the Aggregative Growth of Platinum Nanoparticles in Atomic Layer Deposition: An Avenue to Size Selection. *Journal of Physical Chemistry Letters* **2017**, *8*, 975–983.

(272) Challa, S. R.; Delariva, A. T.; Hansen, T. W.; Helveg, S.; Sehested, J.; Hansen, P. L.; Garzon, F.; Datye, A. K. Relating rates of catalyst sintering to the disappearance of individual nanoparticles during Ostwald ripening. *Journal of the American Chemical Society* **2011**, *133*, 20672–20675.

(273) Parker, S. C.; Campbell, C. T. Reactivity and sintering kinetics of Au/-TiO2(110) model catalysts: Particle size effects. *Topics in Catalysis* **2007**, *44*, 3–13.

(274) Wan, Q.; Hu, S.; Dai, J.; Chen, C.; Li, W. X. First-Principles Kinetic Study for Ostwald Ripening of Late Transition Metals on TiO 2 (110). *Journal of Physical Chemistry C* **2019**, *123*, 1160–1169.

(275) Horwath, J. P.; Voorhees, P. W.; Stach, E. A. Quantifying Competitive Degradation Processes in Supported Nanocatalyst Systems. *Nano Letters* **2021**, *21*, 5324–5329.

(276) Plessow, P. N.; Abild-Pedersen, F. Sintering of Pt Nanoparticles via Volatile PtO2: Simulation and Comparison with Experiments. *ACS Catalysis* **2016**, *6*, 7098–7108.

(277) Goodman, E. D.; Carlson, E. Z.; Dietze, E. M.; Tahsini, N.; Johnson, A.; Aitbekova, A.; Nguyen Taylor, T.; Plessow, P. N.; Cargnello, M. Size-controlled nanocrystals reveal spatial dependence and severity of nanoparticle coalescence and Ostwald ripening in sintering phenomena. *Nanoscale* **2021**, *13*, 930–938.

(278) Van Den Berg, R.; Parmentier, T. E.; Elkjær, C. F.; Gommes, C. J.; Sehested, J.; Helveg, S.; De Jongh, P. E.; De Jong, K. P. Support Functionalization To Retard Ostwald Ripening in Copper Methanol Synthesis Catalysts. *ACS Catalysis* **2015**, *5*, 4439–4448.

(279) Teixeira, A. R.; Chang, C. C.; Coogan, T.; Kendall, R.; Fan, W.; Dauenhauer, P. J. Dominance of surface barriers in molecular transport through silicalite-1. *Journal of Physical Chemistry C* **2013**, *117*, 25615–25621.

(280) Cheung, O.; Bacsik, Z.; Fil, N.; Krokidas, P.; Wardecki, D.; Hedin, N. Selective Adsorption of CO2on Zeolites NaK-ZK-4 with Si/Al of 1.8-2.8. *ACS Omega* **2020**, *5*, 25371–25380.

(281) Jacobson, M. Z. Review of solutions to global warming, air pollution, and energy security. *Energy and Environmental Science* **2009**, *2*, 148–173.

(282) Johnson, T.; Joshi, A. Review of Vehicle Engine Efficiency and Emissions. *SAE Technical Papers* **2017**, *2017-March*, DOI: 10.4271/2017-01-0907.

(283) Walker, A. Future Challenges and Incoming Solutions in Emission Control for Heavy Duty Diesel Vehicles. *Topics in Catalysis* **2016**, *59*, 695–707.

(284) Piumetti, M.; Bensaid, S.; Fino, D.; Russo, N. Catalysis in Diesel engine NOx aftertreatment: a review. *Catalysis, Structure and Reactivity* **2015**, *1*, 155–173.

(285) Lambert, C. K. Perspective on SCR NO: X control for diesel vehicles. *Reaction Chemistry and Engineering* **2019**, *4*, 969–974.

(286) Gounder, R.; Moini, A. Automotive NO: X abatement using zeolite-based technologies. *Reaction Chemistry and Engineering* **2019**, *4*, 966–968.

(287) Beale, A. M.; Gao, F.; Lezcano-Gonzalez, I.; Peden, C. H.; Szanyi, J. Recent advances in automotive catalysis for NOx emission control by small-pore microporous materials. *Chemical Society Reviews* **2015**, *44*, 7371–7405.

(288) Kwak, J. H.; Tonkyn, R. G.; Kim, D. H.; Szanyi, J.; Peden, C. H. Excellent activity and selectivity of Cu-SSZ-13 in the selective catalytic reduction of NOx with NH3. *Journal of Catalysis* **2010**, *275*, 187–190.

(289) Wang, D.; Gao, F.; Peden, C. H.; Li, J.; Kamasamudram, K.; Epling, W. S. Selective catalytic reduction of NOx with NH3 over a Cu-SSZ-13 catalyst prepared by a solid-state ion-exchange method. *ChemCatChem* **2014**, *6*, 1579–1583.

(290) Chen, H.-Y. Cu/Zeolite SCR Catalysts for Automotive Diesel NOx Emission Control. **2014**, 123–147.

(291) Hammershøi, P. S.; Jensen, A. D.; Janssens, T. V. Impact of SO2-poisoning over the lifetime of a Cu-CHA catalyst for NH3-SCR. *Applied Catalysis B: Environmental* **2018**, *238*, 104–110.

(292) Hammershøi, P. S.; Jangjou, Y.; Epling, W. S.; Jensen, A. D.; Janssens, T. V. Reversible and irreversible deactivation of Cu-CHA NH3-SCRcatalysts by SO2 and SO3. *Applied Catalysis B: Environmental* **2018**, *226*, 38–45.

(293) Xi, Y.; Ottinger, N.; Su, C.; Liu, Z. G. Sulfur Poisoning of a Cu-SSZ-13 SCR Catalyst under Simulated Diesel Engine Operating Conditions. *SAE Technical Papers* **2021**, DOI: 10.4271/2021-01-0576.

(294) Kumar, A.; Li, J.; Luo, J.; Joshi, S.; Yezerets, A.; Kamasamudram, K.; Schmidt, N.; Pandya, K.; Kale, P.; Mathuraiveeran, T. Catalyst Sulfur Poisoning and Recovery Behaviors: Key for Designing Advanced Emission Control Systems. *SAE Technical Papers* **2017**, *2017-Janua*, DOI: 10.4271/2017-26-0133.

(295) Wijayanti, K.; Leistner, K.; Chand, S.; Kumar, A.; Kamasamudram, K.; Currier, N. W.; Yezerets, A.; Olsson, L. Deactivation of Cu-SSZ-13 by SO2 exposure under SCR conditions. *Catalysis Science and Technology* **2016**, *6*, 2565–2579.

(296) Cheng, Y.; Lambert, C.; Kim, D. H.; Kwak, J. H.; Cho, S. J.; Peden, C. H. The different impacts of SO2 and SO3 on Cu/zeolite SCR catalysts. *Catalysis Today* **2010**, *151*, 266–270.

(297) Mesilov, V.; Xiao, Y.; Dahlin, S.; Bergman, S. L.; Pettersson, L. J.; Bernasek, S. L. First-Principles Calculations of Condition-Dependent Cu/Fe Speciation in Sulfur-Poisoned Cu- And Fe-SSZ-13 Catalysts. *Journal of Physical Chemistry C* **2021**, *125*, 4632–4645.

(298) Sushkevich, V. L.; Van Bokhoven, J. A. Methane-to-Methanol: Activity Descriptors in Copper-Exchanged Zeolites for the Rational Design of Materials. *ACS Catalysis* **2019**, *9*, 6293–6304.

(299) Narsimhan, K.; Iyoki, K.; Dinh, K.; Román-Leshkov, Y. Catalytic oxidation of methane into methanol over copper-exchanged zeolites with oxygen at low temperature. *ACS Central Science* **2016**, *2*, 424–429.

(300) Ipek, B.; Lobo, R. F. Catalytic conversion of methane to methanol on Cu-SSZ-13 using N2O as oxidant. *Chemical Communications* **2016**, *52*, 13401–13404.

(301) Ipek, B.; Wulfers, M. J.; Kim, H.; Göltl, F.; Hermans, I.; Smith, J. P.; Booksh, K. S.; Brown, C. M.; Lobo, R. F. Formation of [Cu2O2]2+ and [Cu2O]2+ toward C-H Bond Activation in Cu-SSZ-13 and Cu-SSZ-39. *ACS Catalysis* **2017**, *7*, 4291–4303.

(302) Lan, Z.; Sharada, S. M. Computational strategies to probe CH activation in dioxo-dicopper complexes. *Physical Chemistry Chemical Physics* **2018**, *20*, 25602–25614.

(303) Pappas, D. K. et al. Methane to Methanol: Structure-Activity Relationships for Cu-CHA. *Journal of the American Chemical Society* **2017**, *139*, 14961–14975.

(304) Vanelderen, P.; Snyder, B. E.; Tsai, M. L.; Hadt, R. G.; Vancauwenbergh, J.; Coussens, O.; Schoonheydt, R. A.; Sels, B. F.; Solomon, E. I. Spectroscopic definition of the copper active sites in mordenite: Selective methane oxidation. *Journal of the American Chemical Society* **2015**, *137*, 6383–6392.

(305) Göltl, F.; Bhandari, S.; Mavrikakis, M. Thermodynamics Perspective on the Stepwise Conversion of Methane to Methanol over Cu-Exchanged SSZ-13. *ACS Catalysis* **2021**, *11*, 7719–7734.

(306) Göltl, F.; Bhandari, S.; Lebrón-Rodríguez, E. A.; Gold, J. I.; Zones, S. I.; Hermans, I.; Dumesic, J. A.; Mavrikakis, M. Identifying hydroxylated copper dimers in SSZ-13 via UV-vis-NIR spectroscopy. *Catalysis Science and Technology* **2022**, 2744–2748.

(307) Brezicki, G.; Kammert, J. D.; Gunnoe, T. B.; Paolucci, C.; Davis, R. J. Insights into the Speciation of Cu in the Cu-H-Mordenite Catalyst for the Oxidation of Methane to Methanol. *ACS Catalysis* **2019**, *9*, 5308–5319.

(308) Wulfers, M. J.; Teketel, S.; Ipek, B.; Lobo, R. F. Conversion of methane to methanol on copper-containing small-pore zeolites and zeotypes. *Chemical Communications* **2015**, *51*, 4447–4450.

(309) Dinh, K. T.; Sullivan, M. M.; Serna, P.; Meyer, R. J.; Dincă, M.; Román-Leshkov, Y. Viewpoint on the Partial Oxidation of Methane to Methanol Using Cu- and Fe-Exchanged Zeolites. *ACS Catalysis* **2018**, *8*, 8306–8313.

(310) Kulkarni, A. R.; Zhao, Z. J.; Siahrostami, S.; Nørskov, J. K.; Studt, F. Monocopper Active Site for Partial Methane Oxidation in Cu-Exchanged 8MR Zeolites. *ACS Catalysis* **2016**, *6*, 6531–6536.

(311) Verma, A. A.; Bates, S. A.; Anggara, T.; Paolucci, C.; Parekh, A. A.; Kamasamudram, K.; Yezerets, A.; Miller, J. T.; Delgass, W. N.; Schneider, W. F.; Ribeiro, F. H. NO oxidation: A probe reaction on Cu-SSZ-13. *Journal of Catalysis* **2014**, *312*, 179–190.

(312) Ruggeri, M. P.; Nova, I.; Tronconi, E.; Pihl, J. A.; Toops, T. J.; Partridge, W. P. In-situ DRIFTS measurements for the mechanistic study of NO oxidation over a commercial Cu-CHA catalyst. *Applied Catalysis B: Environmental* **2015**, *166-167*, 181–192.

(313) Dinh, K. T.; Sullivan, M. M.; Narsimhan, K.; Serna, P.; Meyer, R. J.; Dincă, M.; Román-Leshkov, Y. Continuous Partial Oxidation of Methane to Methanol Catalyzed by Diffusion-Paired Copper Dimers in Copper-Exchanged Zeolites. *Journal of the American Chemical Society* **2019**, *141*, 11641–11650.

(314) Li, H.; Paolucci, C.; Khurana, I.; Wilcox, L. N.; Göltl, F.; Albarracin-Caballero, J. D.; Shih, A. J.; Ribeiro, F. H.; Gounder, R.; Schneider, W. F. Consequences of exchange-site heterogeneity and dynamics on the UV-visible spectrum of Cu-exchanged SSZ-13. *Chemical Science* **2019**, *10*, 2373–2384.

(315) Engedahl, U.; Grönbeck, H.; Hellman, A. First-Principles Study of Oxidation State and Coordination of Cu-Dimers in Cu-SSZ-13 during Methane-to-Methanol Reaction Conditions. *Journal of Physical Chemistry C* **2019**, *123*, 26145–26150.

(316) Sun, J.; Ruzsinszky, A.; Perdew, J. Strongly Constrained and Appropriately Normed Semilocal Density Functional. *Physical Review Letters* **2015**, *115*, 036402.

(317) Thomas C. Allison NIST-JANAF Thermochemical Tables - SRD 13, en, 2013.

(318) Hagberg, A. A.; Schult, D. A.; Swart, P. J. Exploring network structure, dynamics, and function using NetworkX. *7th Python in Science Conference (SciPy 2008)* **2008**, 11–15.

(319) First-Principles Comparison of Proton and Divalent Copper Cation Exchange Energy Landscapes in SSZ-13 Zeolite. *Journal of Physical Chemistry C* **2018**, *122*, 23564–23573.

(320) Muraoka, K.; Chaikittisilp, W.; Okubo, T. Energy Analysis of Aluminosilicate Zeolites with Comprehensive Ranges of Framework Topologies, Chemical Compositions, and Aluminum Distributions. *Journal of the American Chemical Society* **2016**, *138*, 6184–6193.

(321) Brezicki, G.; Zheng, J.; Paolucci, C.; Schlögl, R.; Davis, R. J. Effect of the Co-cation on Cu Speciation in Cu-Exchanged Mordenite and ZSM-5 Catalysts for the Oxidation of Methane to Methanol. *ACS Catalysis* **2021**, *11*, 4973–4987.

(322) Saal, J. E.; Kirklin, S.; Aykol, M.; Meredig, B.; Wolverton, C. Materials design and discovery with high-throughput density functional theory: The open quantum materials database (OQMD). *Jom* **2013**, *65*, 1501–1509.

(323) Kirklin, S.; Saal, J. E.; Meredig, B.; Thompson, A.; Doak, J. W.; Aykol, M.; Rühl, S.; Wolverton, C. The Open Quantum Materials Database (OQMD): Assessing the accuracy of DFT formation energies. *npj Computational Materials* **2015**, *1*, 1–15.

(324) Chen, L.; Janssens, T. V.; Grönbeck, H. A comparative test of different density functionals for calculations of NH3-SCR over Cu-Chabazite. *Physical Chemistry Chemical Physics* **2019**, *21*, 10923–10930.

(325) Bailey, D. M. A note on the crystal structure of ThCu3.6. *Journal of The Less-Common Metals* **1973**, *30*, 164–166.

(326) Berthold, H. J.; Born, J.; Wartchow, R. The crystal structure of copper(I)sulfate Cu 2 SO 4. *Zeitschrift für Kristallographie - Crystalline Materials* **1988**, *183*, 309–318.

(327) Chen, Y.-R.; Epling, W. Degradation Study of Cu-SSZ-13 Selective Catalytic Reduction Catalysts, Ph.D. Thesis, Charlottesville: University of Virginia, 2023.

(328) Wang, T.; Ding, C.; Ma, L.; Ma, Z.; Yang, M.; Wang, J.; Zhang, K. Redispersion of Pt nanoparticles encapsulated within ZSM-5 in oxygen and catalytic properties in partial oxidation of methane. *Journal of Porous Materials* **2022**, *29*, 1337–1347.

(329) Hou, D.; Grajciar, L.; Nachtigall, P.; Heard, C. J. Origin of the Unusual Stability of Zeolite-Encapsulated Sub-Nanometer Platinum. *ACS Catalysis* **2020**, *10*, 11057–11068.

(330) Liu, L.; Lopez-Haro, M.; Lopes, C. W.; Li, C.; Concepcion, P.; Simonelli, L.; Calvino, J. J.; Corma, A. Regioselective generation and reactivity control of subnanometric platinum clusters in zeolites for high-temperature catalysis. *Nature Materials* **2019**, *18*, 866–873.

(331) Choi, M.; Wu, Z.; Iglesia, E. Mercaptosilane-assisted synthesis of metal clusters within zeolites and catalytic consequences of encapsulation. *Journal of the American Chemical Society* **2010**, *132*, 9129–9137.

(332) Liu, Y. et al. A General Strategy for Fabricating Isolated Single Metal Atomic Site Catalysts in y Zeolite. *Journal of the American Chemical Society* **2019**, *141*, 9305–9311.

(333) Felvey, N.; Guo, J.; Rana, R.; Xu, L.; Bare, S. R.; Gates, B. C.; Katz, A.; Kulkarni, A. R.; Runnebaum, R. C.; Kronawitter, C. X. Interconversion of Atomically Dispersed Platinum Cations and Platinum Clusters in Zeolite ZSM-5 and Formation of Platinum gem-Dicarbonyls. *Journal of the American Chemical Society* **2022**, *144*, 13874–13887.

(334) Zhang, S.; Li, Y.; Ding, C.; Niu, Y.; Zhang, Y.; Yang, B.; Li, G.; Wang, J.; Ma, Z.; Yu, L.-J. Atomic Dispersion of Pt Clusters Encapsulated Within ZSM-5 Depending on Aluminum Sites and Calcination Temperature. *Small Structures* **2022**, *4*, 2200115.

Appendices

Appendix A

Supporting Information of Chapter 4: Effect of Reaction Conditions and SO_2 Exposure on Cu Speciation in SSZ-13 Zeolites

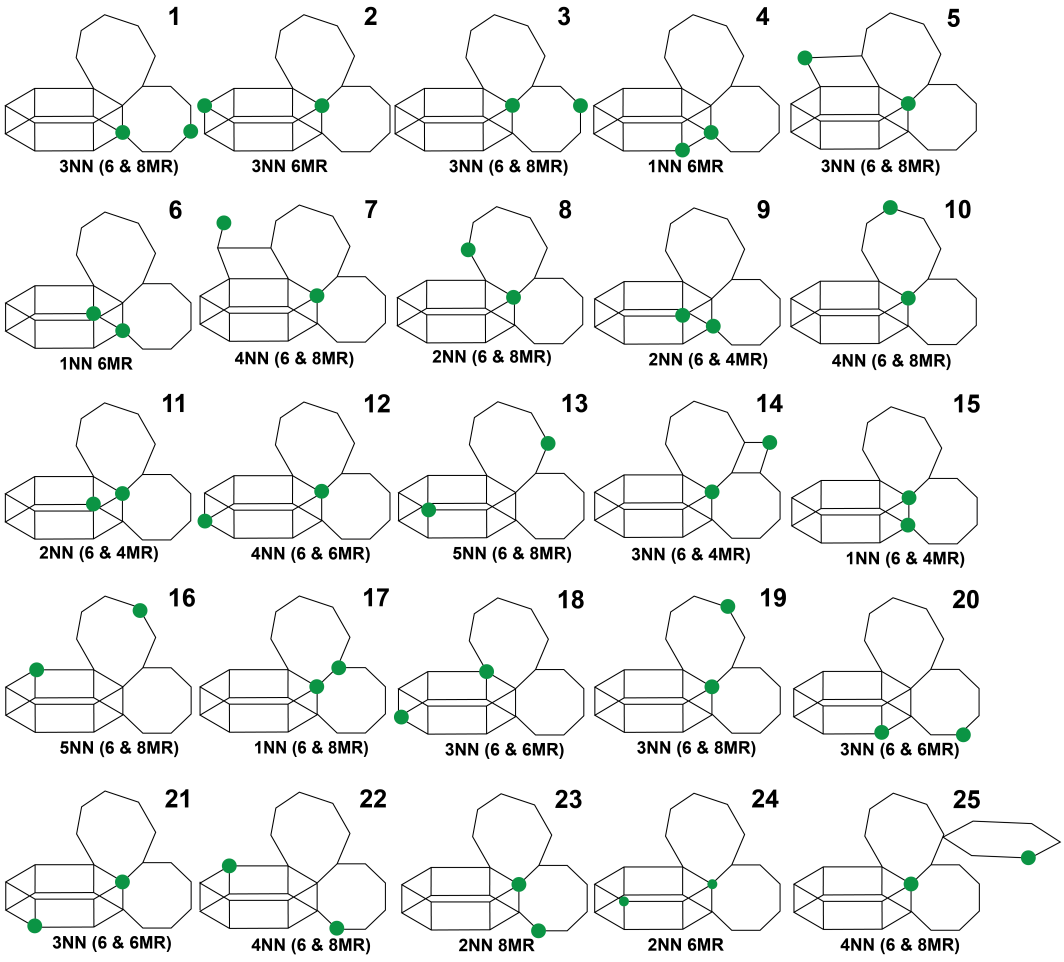

Figure A.1: 25 symmetry-distinct Al-Al configurations plausible in 36 T-site SSZ-13

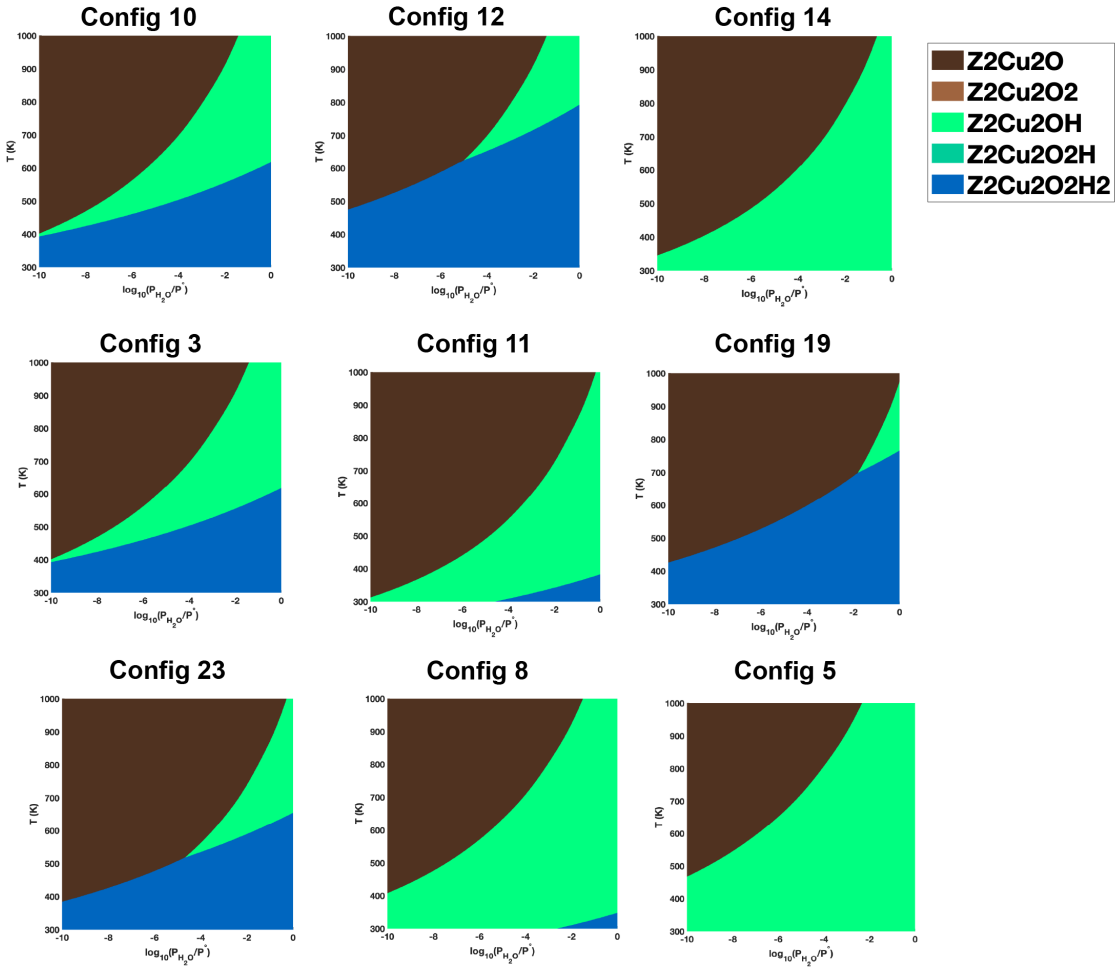

Figure A.2: SCAN-D3(BJ)vdw based thermodynamic phase diagram at 10% O_2 for the 9 Al-Al configurations forming Cu dimers as shown in Figure 5.2

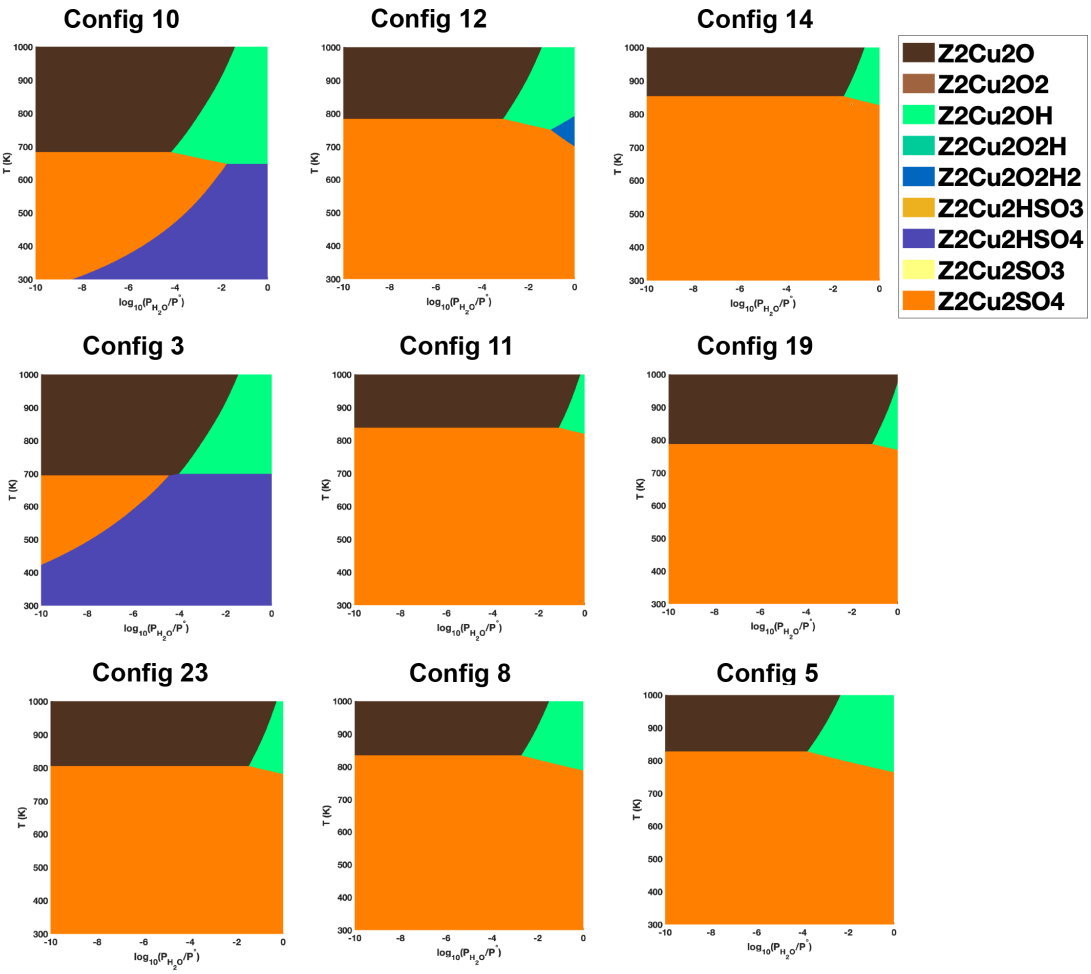

Figure A.3: SCAN-D3(BJ)vdw based thermodynamic phase diagram at 10% O_2, 30 ppm SO_2 for the 9 Al-Al configurations forming Cu dimers as shown in Figure 5.2

Table A.1: SCAN-D3(BJ)vdw Energies of Hydroxylated and Sulfated Monatomic and Dimeric Cu Species Computed at 698 K, 10% O_2, 30 ppm SO_2, 7% H_2O for the 3 Example Al-Al Configurations shown in Figure 4.2 and 4.4

	Configuration 1	Configuration 2	Configuration 3
Hydroxylated Cu Species			
Z2[Cu(H2O)4]/Z[CuOH(H2O)3] or Z[CuOH(H2O)3]/Z[CuOH(H2O)3]	0	0	0
[Z2Cu]/ZCuOH] or [ZCuOH]/[ZCuOH]	-329	-205	-194
Z2Cu2O	-249	-201	-372
Z2Cu2O2	-141	-203	-307
Z2Cu2OH	-296	-227	-384
Z2Cu2O2H	-178	-103	-271
Z2Cu2O2H2	-259	NA	-293
Sulfated Cu Species			
Z2H2[Cu(HSO4)2]/ZH[[Cu(HSO4)2] or ZH [Cu(HSO4)2] / ZH [Cu(HSO4)2]	+87	-6	-132
Z2 [CuHSO4(H2O)2]/Z [CuHSO4(H2O)2] or Z [CuHSO4(H2O)2] / Z [CuHSO4(H2O)2]	+77	-32	-122
[ZCuHSO4/ZH]/[ZCuHSO4] or [ZCuHSO4]/ [ZCuHSO4]	-187	-85	+100
[ZCuSO4/ZH]/[ZCuHSO4]	-208	NA	NA
[Z2Cu2HSO3]	-112	-70	-258
[Z2Cu2HSO4]	-236	-327	-421
[Z2Cu2SO3]	-107	-173	-325
[Z2Cu2SO4]	-214	-274	-463

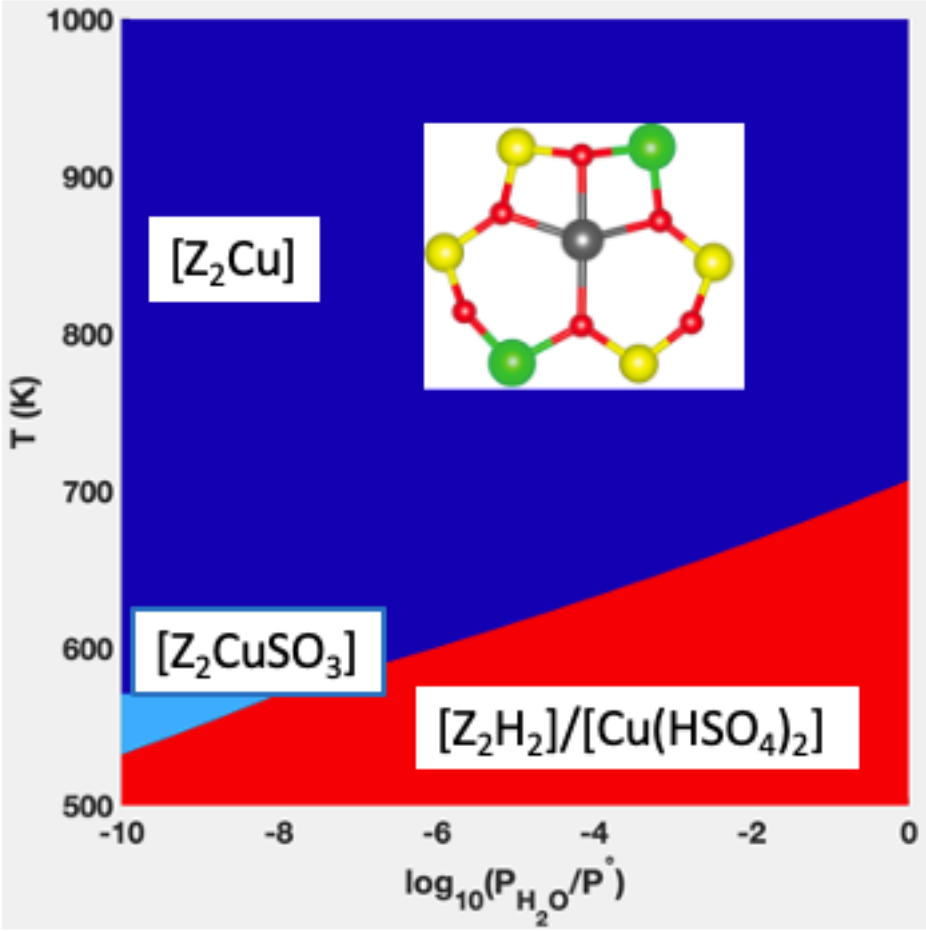

Figure A.4: SCAN-D3(BJ)vdw based thermodynamic phase diagram at 10% O_2, 30 ppm SO_2 for Z_2Cu

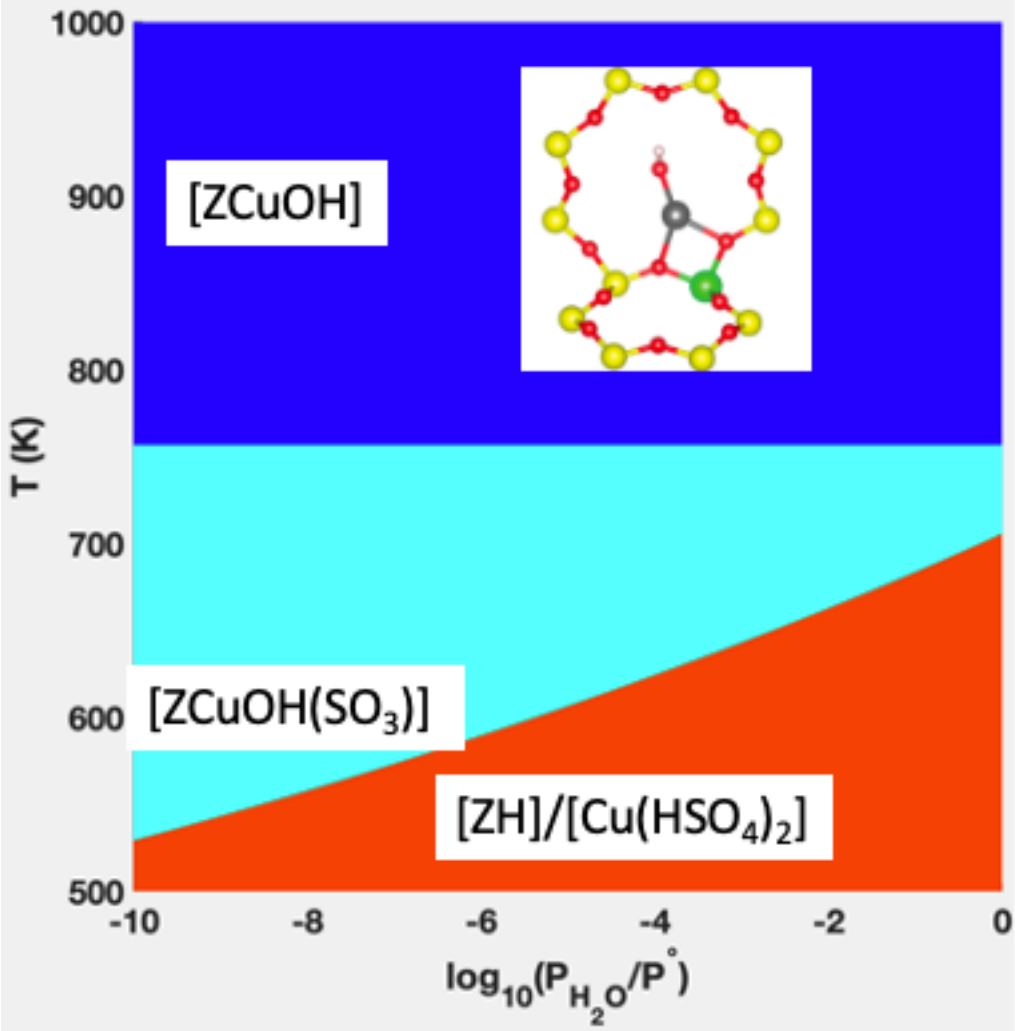

Figure A.5: SCAN-D3(BJ)vdw based thermodynamic phase diagram at 10% O_2, 30 ppm SO_2 for ZCuOH